Numerical Modelling of Heat Transfer and Thermal Stresses in gas turbine guide vanes

by

Faisal Rahman

Submitted in partial fulfillment of the requirements for the degree,

MASTER OF ENGINEERING

in the Faculty of Engineering, Built Environment and Information Technology,
University of Pretoria, Pretoria

November 2003

Numerical Modelling of Heat Transfer and Thermal Stresses in gas turbine guide vanes

by

Faisal Rahman

Study leader: Prof. J.A. Visser

Department: Mechanical and Aeronautical Engineering

Degree: Master of Engineering

SUMMARY

Due to a relative high thermal efficiency, the gas turbine engine has wide ranging applications in various industries today. The aerospace and power generation sectors are probably the best known. One method of increasing the thermal efficiency of a gas turbine engine is to increase the turbine inlet temperature. This increase in temperature will result in an additional thermal load being placed on the turbine blades and in particular the nozzle guide vanes. The higher temperature gradients will increase the thermal stresses. In order to prevent failure of blades due to thermal stresses, it is important to accurately determine the magnitude of the stresses during the design phase of an engine.

The accuracy of the thermal stresses mainly depends on two issues. The first is the determination of the heat transfer from the fluid to the blade and then secondly the prediction of the thermal stresses in the blade as a result of the thermal loading. In this study the flow and heat transfer problem is approached through the use of computational fluid dynamics (CFD). The principal focus is to predict the heat transfer and thermal stresses for steady state cases for both cooled and uncooled nozzle guide vanes through numerical modelling techniques. From the literature, two studies have been identified for which experimental data was available. These case studies can therefore be used to evaluate the accuracy of using CFD to simulate the thermal loading on the blades. One study focused only on solving heat

transfer whilst the other included thermal stress modelling. The same methodology is then applied to a three-dimensional application in which flow and heat transfer was solved for a nozzle guide vane of a commercial gas turbine engine. The accuracy of results varied with the choice of turbulence model but was, generally within ten percent of experimental data. It was shown that the accurate determination of the heat transfer to the blade is the key element to accurately determine the thermal stresses.

Keywords:

Thermal efficiency
Turbine inlet temperature
Heat transfer
Steady state
Numerical modelling
Gas turbine engine
Thermal stresses
Computational fluid dynamics
Cooled/uncooled nozzle guide vane
Turbulence model

ACKNOWLEDGEMENTS

In the name of God, Most Gracious, Most Merciful

I would like to thank the following people for their contributions during the course of this study:

Prof J.A. Visser for his interest, support, guidance and encouragement during the study. I have indeed learnt a lot and thoroughly enjoyed the work I did.

Danie de Kok, Montresor Morris and Jurie Bezuidenhout for the great support, encouragement and humour they provided me in various aspects of this study. Their help and patience was invaluable in helping me complete this work. I really appreciate what you have done for me.

To everyone else who has contributed directly or indirectly to this study, I appreciate all the help that you have given me.

Finally to my parents and family, thank you for the support and patience you have shown me during the study. I feel I have achieved something that would otherwise have not been possible without your support. To my sister, a special thanks for having the patience to proof read this dissertation.

TABLE OF CONTENTS

Chapter One

Introduction

This chapter presents an introduction and describes the specific problem. The various relevant literature studied has been summarised. A motivation for the study is given and the chapter concludes with an outline of the subsequent chapters.

1.1 The problem considered

The gas turbine engine has wide ranging applications in various industries today. The aerospace and power generation sectors are probably the best known. The efficiency of the gas turbine engine is one of its biggest advantages, but the high capital and maintenance costs when exposed to cyclic operating conditions, have been a limiting factor. Therefore, the gas turbine designer needs to carefully balance efficiency, capital and maintenance costs when designing a new engine. An increase in combustor exit temperatures is one method of improving the overall efficiency of the gas turbine engine whilst keeping operational costs low. However, raising the operating temperature increases the thermal load on several hot end components that may result in increased maintenance costs.

The maintenance costs can often be reduced through minor operating adjustments. These adjustments require the ability to predict the influence of any change on the expected usable life of the different components. A typical example is the nozzle guide vanes. The nozzle guide vanes are directly exposed to the combustor exit temperatures. To protect the material, the guide vanes are usually cooled by cold air bled from the compressor and passed through intricate passages inside the blade. This result in complex flow phenomena and heat transfer occurring that subjects the blade to large thermal loads due to the temperature gradients present. This is of particular importance during start-up and shut-down procedures. The thermal loading will induce *thermal stresses* in the blade. The rotor blades are also subjected to centrifugal loads. The magnitude of the loads and the number of cycles to failure are critical information required to prevent failure during operation but still maximising the usable component life.

The determination of thermal stresses is one of the most important aspects in the operation of gas turbine engines. The harsh operating conditions of gas turbines make it almost impossible to accurately measure thermal stresses in the blades. Therefore, calculations and experiments are needed to estimate

blade life. Most experimental work is done in test rigs and cascade facilities. These experimental results thus represent only an isolated part of the total problem faced by the operators. When done properly, the results are valuable and can solve several existing problems. An attractive alternative is to use numerical modelling techniques. In the case of turbine blades, the first step is to model the flow of the hot combustion gas over the blade accurately. The determination of the correct heat transfer from the hot gas to the blade will give the correct temperature distribution over the blade surface. This can then be used to obtain the thermal stress magnitude and distribution on the blade.

The combination of the consistent increase in computational power, more accurate simulation techniques and mathematical sub-models has made numerical solutions the dominant way of predicting thermal stresses in gas turbine blades. Large-scale validation of numerical models also played a key role in the acceptance of numerical simulation techniques by the industry. The accuracy of using some of these models will be evaluated in this study.

1.2 Review of related literature

The drive to improve gas turbine efficiency and reliability has, over a number of years, launched several investigations to obtain the thermal loading on gas turbine blades. The ultimate aim with predicting thermal stresses is to predict fatigue and expected usable life of the turbine blades. The thermal stresses can be basically obtained in one of two ways. The first is using experimental methods while the second is using Finite Element Modelling techniques.

Experiments to obtain accurate thermal stresses in a component with complex geometry and exposed to highly fluctuating thermal conditions is an almost impossible task. This is mainly because the physical process of testing real blades under service conditions is both difficult and uneconomic [1]. Tests, however, provide a realistic simulation of the thermal cycle experienced by real components. A common method to capture the high level of detailed

temperature and stress distribution is through the use high-temperature thin film thermocouples [2].

The majority of projects make use of commercial Finite Element Modelling software packages to solve the stress problem [3]-[6]. Numerical modelling requires proper understanding of the physical process that leads to the formation of thermal stresses. Thermal stresses in gas turbine blades occur in two distinct phases. These are during steady state and transient conditions. It is important to analyse both these thermal stress conditions in order to design the blade correctly [1], [3]-[11]. This is due to the fact that the gas turbine is largely designed for steady state long-term operation.

Steady state thermal stresses are particularly linked to the cooling configuration in gas turbine blades. Cooling hole arrangement, amongst other factors, are responsible for inducing thermal stresses in blades due to the direct role they play in uneven temperature distribution [3], [5], [12]. High thermal stresses can often occur in the vicinity of the cooling holes. One study concluded that optimising the cooling configuration could have a major impact in reducing the levels of thermal stress in the blade [3]. Minimising the temperature gradients was possible through re-configuring the cooling channel layout. In a similar way, it was found that high stresses could occur in the vicinity of impingement holes due to the high thermal gradients present [12]. The shape and location of the cooling configuration had a major influence on the thermal stress distribution.

Transient thermal stresses are calculated to capture the entire operating range of gas turbine engines. Typical transient operations occur during the start-up and shut-down operation of the engine. Since the investigations of these transient operations are difficult to conduct in a real engine, the problem is often broken down into a study where there are a limited number of variables. The development of a computationally efficient procedure for calculating transient thermal stresses from flight-recorded is the eventual goal [13]. The numerical analysis of temperature and stress for a typical gas turbine engine can be divided into the following steps:

- Compute gas stream temperatures, pressures and velocities from the known performance characteristics of the engine
- Compute the secondary air flows, such as cooling bleeds
- Compute the gas/metal heat transfer coefficients from the above
- Apply the temperatures and heat transfer coefficients to a transient heat conduction model of the structure to predict the metal temperatures through the flight
- Transfer the temperature distribution to a structural analysis model and predict the stresses through the flight

Several studies conducted have shown that stresses are often the most severe during transient operating conditions [4], [5], [7], [8]. This is due to the contributing factors such as mechanical loading that includes vibratory effects [14]. Rapid acceleration and deceleration during start-up and shut-down operations place additional stresses that need to be accounted for in the correct design of rotor blades. Uncooled blades can be the most severely affected by transients. The first stage rotor blades are usually the most critical in transient operation as they are exposed to high thermal stresses together with high centrifugal load [4].

It is thus far seen that both steady state and transient thermal stresses need to be accounted for in the design of turbine blades. However, there are several factors that contribute to determining these stresses accurately. By and large they are problem specific, meaning that one needs to closely scrutinize the specific application, then decide what factors contribute to the accurate prediction of thermal stresses by mathematical modelling techniques.

The thermal design of contemporary high-pressure turbine nozzle guide vanes represents one of the most difficult engineering tasks in the design of any modern gas turbine. The most important issue affecting the magnitude and distribution of thermal stresses is thermal loading or temperature distribution. Thus, several studies focus on the investigation of stresses due to temperature and/or load variation [3]-[5], [7], [8], [13], [14]. This has led to

combine aero-thermal performance determination of gas turbine blades, in which there is a fluid-solid coupling at the wall in the numerical procedure to calculate temperature distribution within the blade [3]. This problem can be extended further to a fluid-structure interaction, where thermal stress is also calculated. This could lead to quicker and possibly more accurate solution for a combined temperature/stress problem than the more traditional method of exporting temperature distribution to commercial FEM software to determine the thermal stresses. Thus a program known as *BLADE-CT* was developed and is a coupling of NASA's PCPANEL, STAN5 and CPT programs [7]. The program analyses gas turbine thermal-mechanical stress and natural frequencies under the boundary conditions, which result from the gas flow and the cooling/barrier, flow within a given turbine. The more traditional method of transferring temperature distribution can lead to interpolation errors when temperatures are exported to a FEM package, particularly when the numerical models used in the flow/thermal problem differ from the structural model. Hence a code, TRANCITIS, was developed to transfer three-dimensional transient thermal information accurately, efficiently and automatically from a heat transfer code to a structural analysis code [8]. The code has the ability to handle different mesh densities for the heat transfer analysis and the structural analysis. Finite difference and finite element heat transfer analysis codes can be coupled to both linear and non-linear finite element structural analysis codes.

The problem of determining temperature distributions on gas turbine blades is directly linked in calculating the heat transfer coefficients. This brings to light one of the most challenging tasks facing gas turbine designers. Therefore, much research and effort has been applied to determine the heat transfer coefficients. This includes both experimental and numerical procedures to determine the heat transfer. Several commercial CFD packages are available to aid the numerical modelling of heat transfer. Since the three modes of heat transfer: conduction, convection and radiation are present in gas turbine engines, the task is made even more complex. Finite Volume methods are used in the CFD packages. Numerous studies have been conducted on heat transfer and temperature distributions in gas turbine blades [10], [11], [15],

[16]. In one study [15] a method for calculating the transient temperature fields in cooled turbine blades was demonstrated. The procedure can be used for calculating dangerous (with respect to thermal stresses) temperatures in blades of any configuration. Extensive experiments to determine the heat transfer coefficients on the surface of a cooled nozzle guide vane (NGV) were also conducted [10]. The rate of heat transfer to a gas turbine rotor; along with the effect of Mach number, Reynolds number, inlet flow angle and free stream turbulence on heat transfer rate; was investigated [11]. The study concluded that these factors play a major role in determining heat transfer rates. A similar study [16] investigated the transient heat transfer of a first stage rotor blade during start-up and shut down conditions. The numerical simulation agreed within ten percent with experimental data. Many other similar studies have been conducted on turbine nozzle guide vanes as well as rotor blades. The eventual aim of these studies has been to ascertain the effect of increased turbine inlet temperature.

A major influencing factor on the accuracy of predicting thermal stresses in gas turbine blades is the formulation of the material properties. The modelling of physical properties has to be in tandem with the specific problem as well as the resources available to tackle the problem. The material used may also exhibit low variation of physical properties with temperature and hence a constant value may suffice. In such cases, it may be acceptable to model the properties as temperature independent [5]. The elastic modulus and thermal conductivity of the blade metal can be assumed constant regardless of temperature to reduce computational effort. This is acceptable if the material properties exhibit no large temperature dependence.

Since the blades are subjected to large variations in the temperatures, it is important to account for the temperature dependence of the physical properties of the material [17]. This is often the case in transient operation. The Modulus of Elasticity (Young's Modulus), thermal coefficient of expansion and thermal conductivity are the most temperature sensitive. Previous studies have shown that by modelling the properties of Young's Modulus and coefficient of thermal expansion as temperature dependent can result in

thermal stresses that are up to forty percent higher in magnitude than when modelling these properties as temperature independent [17]. This was despite the material properties exhibiting only a three percent variation over the operating temperature range. During transient solutions, it was assumed that at each time instant the material properties stay constant. Most commercial FEM packages allow for the temperature dependence of the material to be defined. Various constitutive equations are available for describing the mechanical behaviour of alloys, the material often used in fabrication of gas turbine blades [1]. They can involve elastic, elasto-plastic or elasto-visco plastic deformation models. The important conclusion is that failure to account the temperature dependence of material properties, can lead to substantial errors in the predicted thermal stresses.

If temperatures are too high, thermal barrier coatings (TBCs) are often used in the hottest parts of gas turbines to protect the materials. Thermal barrier coating systems are multi-layer material systems that provide thermal protection to metallic components. Whilst TBCs have seen to have a positive effect on gas turbine blades, the temperature profiles have become harder to predict [18], [19]. Alternate materials for gas turbine blades are also increasingly being investigated. Some studies have analysed the possibility of using other materials for turbine blades and in particular the use of ceramics as alternative material has gained popularity [20], [21]. A low cooled ceramic nozzle vane was tested under transient conditions to determine the thermal shock behaviour of an optimised ceramic nozzle vane [20]. It was found that the mechanical loads were negligible compared to the thermally induced stresses due to different thermal expansions. The experimental measurements agreed within ten percent of the finite element model. Manufacturing processes can also play a role in keeping thermal stresses to a minimum. Directional solidification of turbine blades allows an increase of up to 25 K in operating temperatures [22], with single crystal blades being able to withstand even higher temperatures.

All the factors that contribute to thermal stress ultimately lead to thermal fatigue. This is the most important aspect when it comes to lifing prediction of

gas turbine components. The way in which a turbine is operated directly influences the component life. The temperatures, pressure, velocity and turbulence intensity level all influence the blade life. For instance, a study on impingement cooled turbine blades showed that a rise in turbulence level from four to twelve percent decreased the blade life by ten percent [23]. The structural analysis also showed that fatigue and creep modes of failure must be considered to achieve realistic estimates of safe blade operational life. The predicted failure mode and critical region compared favourably to actual blades in service. A study on advanced anisotropic turbine alloys focused on the out-of-phase strain and temperature waveforms [24]. It showed that the worst-case scenario was the completely out-of-phase cycle due to the high mean stresses developed as a result of stress relaxation at the maximum cyclic temperature. This led to thermal fatigue. It has also been shown that thermo mechanical fatigue may be successfully simulated on turbine blades [25].

It is clear thus far that the importance of heat transfer and thermal stresses is of great importance for life prediction of the hot section of gas turbine blades. Hence, it is of paramount importance that the correct heat transfer from the blades is obtained and hence the temperature distribution. This can then be used for obtaining thermal stresses and eventually the component life.

1.3 Motivation

From the literature study it can be concluded that the prediction of thermal stresses in gas turbine blades remains a difficult task to the design engineer. The difficulty encountered in measuring thermal stresses on gas turbine blades poses a challenging problem to the designer. Hence, resources such as CFD and FEM have become attractive alternatives. Similarly turbine blade cascade experiments for flow and temperature distributions on blade surfaces are difficult to set-up and require expensive experimental equipment. A good example is the design of radial temperature profile entering the turbine inlet, with maximum temperature typically occurring at the fifty to seventy percent

radial position. The maximum spatial temperature is difficult to control. Reducing it can result in significant improvement of turbine nozzle guide vane life and/or engine efficiency [26]. Hence, understanding the temperature distributions to see its effects on blade life is important for correct design.

The use of numerical modelling as an aid to the design of the turbine is common practice today. The important question to the design engineer is the accuracy that can be expected from numerical modelling if the results are to be used to determine the expected usable life of turbine blades. This is by no means a trivial question, even if the numerical model accounts for all the known critical issues as discussed in the literature. No wonder, that no studies with thermal stress results for real commercial gas turbine blades could be found in the literature.

The accuracy of the thermal stresses mainly depends on two issues. The first is the modelling of the heat transfer from the fluid to the blade and then secondly the prediction of the thermal stresses in the blade as a result of the thermal loading. The development of software that has fluid-solid interaction has grown over the past few years, but it is still common practice to solve the flow and structural problems separately. The first part is therefore to calculate the heat transfer coefficients and thermal profile around the blade using a commercial CFD code. The next step is to apply these boundary conditions to a FEM model to obtain the thermal stresses.

Although both parts are critically important, the general opinion is that the key to accurate thermal stress results lies in the accuracy in which the heat transfer to the blade can be predicted and the boundary conditions imposed to the FEM model. The objective of this study is therefore firstly, to evaluate the accuracy of the heat transfer coefficients to the blade when using a commercial CFD package. For this purpose the numerical results will be compared to experimental data obtained from the literature for simplified blade configurations.

The real challenge will be to use CFD to calculate the heat transfer coefficients for a cooled nozzle guide vane of a commercial engine. This model has to account for the thermal profile at the exit of the combustor and for real operating conditions. Evaluating the accuracy of the thermal stresses remains a difficult issue. In this case, the only data available are temperature results obtained for the same blade, using a different numerical approach. The results will therefore only be compared to other numerical results for the same nozzle guide vane.

1.4 Outline of this study

Chapter two focuses on the principles of flow, heat transfer and thermal stress modelling. The equations for the conservation of momentum, mass and energy are given, as well as a description of the turbulence models used in this study. The basic theory of thermal stresses is explained.

Chapter three is a heat transfer analysis of a two-dimensional turbine blade cascade using a simple one-equation turbulence model. The computational grid, assumptions and boundary conditions for the model are given. The heat transfer results from the simulation were compared to experimental data.

Chapter four focuses on the determination of heat transfer and thermal stress of a cooled two-dimensional turbine nozzle guide vane. The computational grid and boundary conditions for implementation of the solution are given. Two different turbulence models are evaluated and the results compared to literature.

Chapter five extends the heat transfer analysis to three-dimensions. A commercial cooled NGV is used as a test case. Various boundary conditions are calculated based on certain assumptions. One turbulence model is used and the results are compared to data from different studies.

Chapter six concludes the work done in this study. The most important conclusions are given as well as recommendations for further work. The drawbacks and limitations of numerical modelling experienced during this study are also stated.

Chapter Two

Principles of Heat Transfer and Thermal Stress Modelling

This chapter presents basic fluid flow, heat transfer and thermal stress theory. The basic equations of fluid flow, heat transfer and thermal stresses are given. Turbulence models and near wall treatments are also discussed.

2.1 Preamble

The use of numerical simulations to solve a flow and heat transfer problem depends upon the simultaneous solution of momentum, continuity and energy equations. The focus of achieving the goals of this study is through the use of CFD. Therefore, it is important to examine the basic mathematics involved. The basic theory of thermal stresses and how heat transfer influences it, is also important to get an understanding of the problem.

2.2 Flow and Heat Transfer Modelling

2.2.1 Conservation of Mass and Momentum

The use of CFD to analyse the flow is achieved by solving the partial differential equations for the conservation of momentum, mass and energy. The flow equations are as follows [39]:

Continuity:

$$\frac{\partial \rho}{\partial t} + \Delta \bullet (\rho \bar{v}) = 0 \tag{2.1}$$

Momentum:

$$\rho \frac{DV}{Dt} = \rho g + \nabla \cdot \tau_{ij} - \nabla p \tag{2.2}$$

The equations are solved numerically through the use of the commercial code FLUENT. Fluent uses the finite volume technique to solve these equations.

2.2.2 Turbulence Models

The stress tensor term, τ_{ij}, shown in equation (2.2) can be written as:

$$\tau_{ij} = \underbrace{\mu\left(\frac{\partial u_i}{\partial x_j} + \frac{\partial u_j}{\partial x_i}\right)}_{laminar} - \underbrace{\overline{\rho u_i' u_j'}}_{turbulent} \tag{2.3}$$

It explicitly shows the laminar and turbulent components. Depending on the turbulence model used, the Reynolds stresses $\overline{\rho u_i' u_j'}$ are modelled appropriately. A common method employs the *Boussinesq* hypothesis to relate the Reynolds stresses to the mean velocity gradients [36]:

$$\overline{\rho u_i' u_j'} = \mu_t\left(\frac{\partial u_i}{\partial x_j} + \frac{\partial u_j}{\partial x_i}\right) - \frac{2}{3}\left(\rho k + \mu_t \frac{\partial u_i}{\partial x_i}\right)\delta_{ij} \tag{2.4}$$

All turbulence models used in this study use the *Boussinesq* approach. The disadvantage of the Boussinesq hypothesis is that it assumes the turbulent viscosity to be an isotropic scalar quantity, which is not necessarily the case [36]. Therefore, such a model is unsuitable for high swirl dominated flows and stress-driven secondary flows. Closure of the momentum equations is achieved by the relevant turbulence model used to solve the Reynolds stresses, provided the flow considered is turbulent as is in this study.

The **Spalart-Allmaras** turbulence model is a relatively simple one-equation model that solves a modelled transport equation for the kinematic eddy (turbulent) viscosity [36]. The Spalart-Allmaras model was designed specifically for aerospace applications involving wall-bounded flows. It has been proven to predict accurate results for boundary layers subjected to adverse-pressure gradients and is popular for turbo machinery applications.

The model solves a quantity that is a modified form of the turbulent kinematic viscosity. The transported variable, $\tilde{\upsilon}$, is identical to the turbulent kinematic

viscosity except in the near-wall (viscous affected) region. The transport equation is given by equation (2.5) [36]:

$$\rho\frac{D\tilde{\upsilon}}{Dt}=\rho C_{b1}\tilde{S}\tilde{\upsilon}+\frac{1}{\sigma_{\tilde{\upsilon}}}\left[\frac{\partial}{\partial x_j}\{(\mu+\rho\tilde{\upsilon})\frac{\partial\tilde{\upsilon}}{\partial x_j}\}+C_{b2}\rho\left(\frac{\partial\tilde{\upsilon}}{\partial x_j}\right)^2\right]-\rho C_{\omega 1}f_{\omega}\frac{\tilde{\upsilon}}{d^2} \quad (2.5)$$

The first and last terms of the right hand side of equation (2.5) are the production of turbulent viscosity and the destruction of turbulent viscosity that occurs in the near-wall region due to wall blocking and viscous damping respectively. The turbulent viscosity, μ_t, is computed from

$$\mu_t=\rho\tilde{\upsilon}f_{\upsilon 1} \quad (2.6)$$

The term $f_{\upsilon 1}$ is the viscous damping function. The model constants used in the Spalart-Allmaras turbulence model are as follows:

C_{b1}=0.1335	C_{b2}=0.622	C_{v1}=7.1	$C_{\omega 2}$=0.3
$C_{\omega 3}$=2	C_{prod}=2	κ=0.4187	$\sigma_{\tilde{\upsilon}}$=0.667

The main advantage of the Spalart-Allmaras turbulence model is that it is considered to be economical. It also has a good track record for mildly complex boundary layer flows. The disadvantages of this turbulence model include lack of sub models (for example, combustion and buoyancy) and as yet it has not been widely tested.

This study also made use of the ***k-ε*** turbulence model. There are two forms: the *standard k-ε turbulence model* and the *realizable k-ε turbulence model*. The model involves solving two additional transport equations: one is for the turbulent kinetic energy and the other for turbulence dissipation rate. The turbulent viscosity is then computed as a function of these. The *standard* k-ε turbulence model is a semi-empirical model based on model transport equations for the turbulent kinetic energy (*k*) and its dissipation (*ε*). The model

transport equation for *k* is derived from the exact equation, while the model transport equation for ε was obtained using physical reasoning.

The *realizable* k-ε turbulence model differs from the standard k-ε turbulence model in two ways:

- The realizable k-ε model contains a new formulation for the turbulent viscosity.
- A new transport equation for the dissipation rate, ε, has been derived from an exact equation for the transport of the mean-square vorticity fluctuation.

The term *realizable* means that the model satisfies certain mathematical constraints on the Reynolds stresses, consistent with the physics of turbulent flows. The modelled transport equation for k is the same for both the standard and realizable models as shown in equation (2.7):

$$\rho\frac{Dk}{Dt}=\frac{\partial}{\partial x_i}\left[\left(\mu+\frac{\mu_t}{\sigma_k}\right)\frac{\partial k}{\partial x_j}\right]+G_k+G_b-\rho\varepsilon-Y_M \qquad (2.7)$$

In this equation G_k represents the generation of turbulent kinetic energy due to the mean velocity gradients, G_b represents the generation of turbulent kinetic energy due to buoyancy and Y_M represents the contribution of the fluctuating dilatation in compressible turbulence to overall dissipation rate.

Equation (2.8) shows the equation for the rate of dissipation for the ***realizable*** k-ε model as used in this study.

$$\rho\frac{D\varepsilon}{Dt}=\frac{\partial}{\partial x_j}\left[\left(\mu+\frac{\mu_t}{\sigma_\varepsilon}\right)\frac{\partial \varepsilon}{\partial x_j}\right]+\rho C_1 S\varepsilon-\rho C_2\frac{\varepsilon^2}{k+\sqrt{\upsilon\varepsilon}}+C_{1\varepsilon}\frac{\varepsilon}{k}C_{3\varepsilon}G_b \qquad (2.8)$$

The model constants for the *realizable* model are:

$C_{1\varepsilon}$=1.44	C_2=1.9	σ_k=1	σ_ε=1.2

Thus the main difference between the *standard* and *realizable* models is that the term C_μ is not a constant in the *realizable* model but rather computed from equation (2.9):

$$C_\mu = \frac{1}{A_0 + A_s \frac{U^* k}{\varepsilon}} \tag{2.9}$$

where A_0 and A_s are model constants.

This in turn has a bearing on the eddy viscosity, which is computed from equation (2.10):

$$\mu_t = \rho C_\mu \frac{k^2}{\varepsilon} \tag{2.10}$$

Coupled with the use of a turbulence model, is the near wall treatment. The choice of the particular turbulence model and the near wall treatment culminated from the consideration of the specific problem.

There are three options available for near wall treatments in FLUENT. These are the *standard wall functions*, *non-equilibrium wall functions* and the *enhanced wall treatment* [36]. The standard wall functions are based on the log-law of the wall. This method is considered to be robust, economical and reasonably accurate. It is, however, poor in predicting separation and shock waves accurately. The non-equilibrium wall function approach can be employed when separation and/or shock waves are expected in the flow. This method sensitises the log-law for mean velocities to pressure gradients. Therefore it has better accuracy in predicting complex flows.

The enhanced wall treatment is a near-wall modelling method that combines a two-layer model with enhanced wall functions [36]. The requirement for this method is that a fine mesh near the wall that is sufficient enough to resolve the laminar sub layer be present. Hence the concept of y^+ is employed. Y^+ is a local Reynolds number near the wall region. It is based on a friction velocity

(u_t) and a distance from the centroid of the first cell adjacent to the wall (y). It is defined mathematically by equation (2.11):

$$y^+ = \frac{\rho u_t y}{\mu} \tag{2.11}$$

In studies that involve accurate heat transfer modelling, it is important to ensure the correct y^+ range. For the enhanced wall treatment, a fine near wall mesh requires $y^+ \approx 1$, whereas for other wall treatments the following range should be adhered to: $50 < y^+ < 150$ [36].

A fine near wall mesh may be impractical due to vast computational requirements. Figure 2.1 shows the near wall treatments in FLUENT. It points out the differences between the wall function approach and the near-wall model approach.

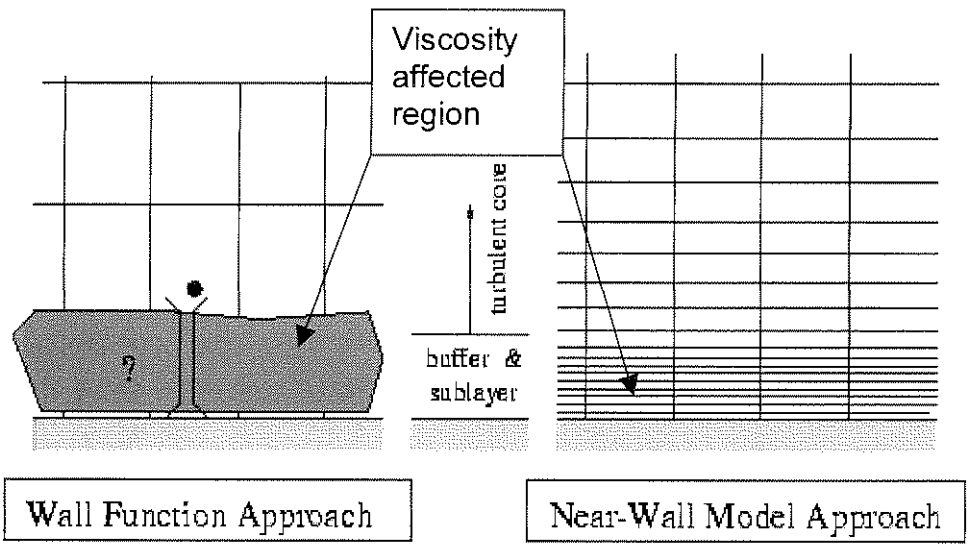

Figure 2.1 – Near Wall Treatments in FLUENT [36]

The main difference between the Wall Function approach and the Near Wall Model is that the viscosity affected region is not resolved but bridged by the wall function in the Wall Function method whereas it is resolved entirely to the wall in the Near Wall model.

2.2.3 Heat Transfer

The energy equation must be solved when heat transfer is to be determined. The energy equation is as follows:

Energy:

$$\Delta\bullet(\rho\bar{v}T)=\Delta\bullet\left[\left(\frac{\mu}{Pr}+\frac{\mu_t}{Pr_t}\right)\Delta T\right]-[\tau:\Delta\bar{v}]+\frac{Dp}{Dt} \tag{2.12}$$

When a fixed temperature condition is applied at a wall, the heat flux to the wall from the fluid is computed from equation (2.13):

$$q=h_f(T_w-T_f)+q_{rad} \tag{2.13}$$

The **local** heat transfer coefficient is solved based on the flow conditions, that is, laminar or turbulent. For turbulent flow, it then takes the form shown in equation (2.14):

$$h=(T_w-T_p)\rho c_p C_\mu^{\frac{1}{4}} k_p^{\frac{1}{2}} \tag{2.14}$$

The terms C_μ and k are modelled according to the turbulence model used. This implies that the heat transfer coefficient and turbulence model are related. It then becomes important to pay special consideration to the turbulence model when accurate heat transfer results are of paramount importance.

2.3 Thermal Stress Theory

There are two main types of stress that may occur in a body. These are mechanical and thermal stresses. Mechanical stresses occur due to a

physical loading such as an applied force, body weight and vibrations. Thermal stresses occur as a result of changes in temperatures. Temperature changes are known to cause expansion or contraction on various bodies. The change, for instance, in length of the body can be related by the coefficient of linear thermal expansion (α) and temperature difference between the initial and final temperatures. This coefficient, α, is the change in length of the bar per unit length due to a change in temperature of 1^0 [29].

If all the fibres of a body are free to expand or contract, no stress is produced by the temperature change. In real engineering applications objects seldom have uniform geometry. Hence, expansion or contraction generally cannot proceed freely so that stresses are produced. External restraints on the body that prevent expansion or contraction also produce stresses in the body. These stresses are referred to as *thermal stresses* [29]. Thermal stresses can also arise as a result of uniform temperatures in bodies consisting of different materials, for instance two bars fastened together such that they restrain each other.

There are several variables that determine the thermal stress levels in a component [30]:

- The shape of the structure
- The mechanical and physical properties of the material
- The initial fluid to metal temperature difference
- The subsequent changes of fluid temperature with time
- The spatial variation of surface heat transfer coefficients, and the way in which the coefficients change during a transient.

Theoretical methods are used to investigate the effect of component shape and of material properties on thermal stress levels whilst the experimental data provides information for the thermal boundary conditions and on the fluid temperature changes which occur during transients.

The role of material properties in calculating thermal stresses can be explained through the following equations. Consider the change in length of a bar:

$$\Delta L = \alpha L(T - T_0) \tag{2.15}$$

T and T_0 are the final and initial temperatures respectively. The elongation of a bar of length L due to a uniform stress, σ is:

$$\Delta L = \frac{\sigma L}{E} \tag{2.16}$$

In the above equation, E is the modulus of elasticity. If the bar is completely restrained so that it does not change length, bow or buckle the elongation given by (2.15) must cancel the elongation given by (2.16) to give the thermal stress as:

$$\sigma = \alpha E(T - T_0) \tag{2.17}$$

The negative sign to indicate a compressive stress has been ignored. It must be pointed out that the material properties E and α are temperature dependent. Young's Modulus decreases slowly with temperature rise and α usually increases slowly with temperature rise [29]. Young's Modulus also depends upon the stress-strain curve for the material, decreasing rapidly if the stress is in the plastic portion of the stress-strain curve.

Equations (2.15)-(2.17) present the one dimensional thermal stress formulation. The problem can be extended to two-dimensions, with particular focus on a two-dimensional turbine blade. The stress distribution in the mid-span cross section of the blade is calculated assuming the *plain strain* conditions. Plain strain is defined to be a state of strain in which the strain

normal to the x-y plane ε_z and the shear strains ε_{xz} and ε_{yz} are assumed to be zero [31]. This implies that: $\varepsilon_z = \varepsilon_{xz} = \varepsilon_{yz} = 0$. This assumption is valid for long bodies with constant cross sectional area. Isotropic linear elastic material behaviour is also assumed. In order to comply with the equilibrium condition of the external force in the z-direction, which is supposed to be zero, the following condition must hold:

$$\sum \sigma_{zi} \cdot A_i = 0 \tag{2.18}$$

According to Hooke's Law which states that the stress is directly proportional to the strain for a given direction, and with $\varepsilon_z=0$, the stress normal to the cross section is given by:

$$\sigma_z = \upsilon \cdot \left(\sigma_x + \sigma_y\right) - \alpha\left(T - T_{ref}\right) \cdot E \tag{2.19}$$

The stress components other than σ_z are found to be negligible as shown by Maya et al [5]. An approximate solution of the equilibrium condition, as shown in equation (2.18), can be achieved with an area-weighted temperature as the initial stress free temperature. Stresses in the z-direction will occur due to temperatures either higher or lower than the reference temperature, which implies when there must be a temperature gradient. For the particular nozzle guide vane considered, there is a temperature gradient due to the different cooling rates applied in the different cooling holes.

The von Mises stress is often the failure criterion used for design purposes. This was the case applicable in this particular blade analysis. The von Mises stress σ_{VM} is related to the principle stresses as shown in equation (2.20):

$$\sigma_{VM} = \frac{1}{\sqrt{2}} \sqrt{(\sigma_1 - \sigma_2)^2 + (\sigma_2 - \sigma_3)^2 + (\sigma_3 - \sigma_1)^2} \tag{2.20}$$

In the above equation, σ_1, σ_2, and σ_3 are the principle stresses. It can thus be deduced that the von Mises stresses are always positive.

It has been established how thermal stresses arise in one and two-dimensional bodies. Similarly the theory can be extended to three dimensions [29]. In this study a commercial software package was used to calculate the thermal stresses and hence the three dimensional theory is beyond the scope of this study.

2.4 Summary

The general theory of flow, heat transfer modelling and thermal stresses has been discussed. The Reynolds Averaged Navier-Stokes equations for the conservation of momentum, mass and energy were presented. Turbulence models and near wall treatments as used in this study were also briefly explained. The mathematics behind one and two-dimensional thermal stresses was also presented. The focus now shifts to the numerical modelling of the problem, where the various theory shall be applied.

Chapter Three

Heat Transfer Modelling of a 2D turbine blade cascade

This chapter analyses heat transfer modelling on a two-dimensional turbine blade cascade. It presents the computational grid, boundary conditions as implemented in the numerical model and results of the analysis. The results have been compared to experimental data obtained from literature.

3.1 Preamble

The first step in the ultimate goal for obtaining thermal stresses is to obtain accurate heat transfer data over a blade surface. This part of the study aims to achieve results through the use of commercial computational fluid dynamics (CFD) software that can be validated by experimental results. The experiments used for the validation purpose were conducted at the *von Karman Institute for Fluid Dynamics* (VKI) on a turbine nozzle guide vane mounted in a linear cascade arrangement [33]. CFD is being used because boundary layer methods have been used extensively in the past and, this method may fail near stagnation or separation points [34]. The commercial CFD code **FLUENT** was used to conduct the simulation.

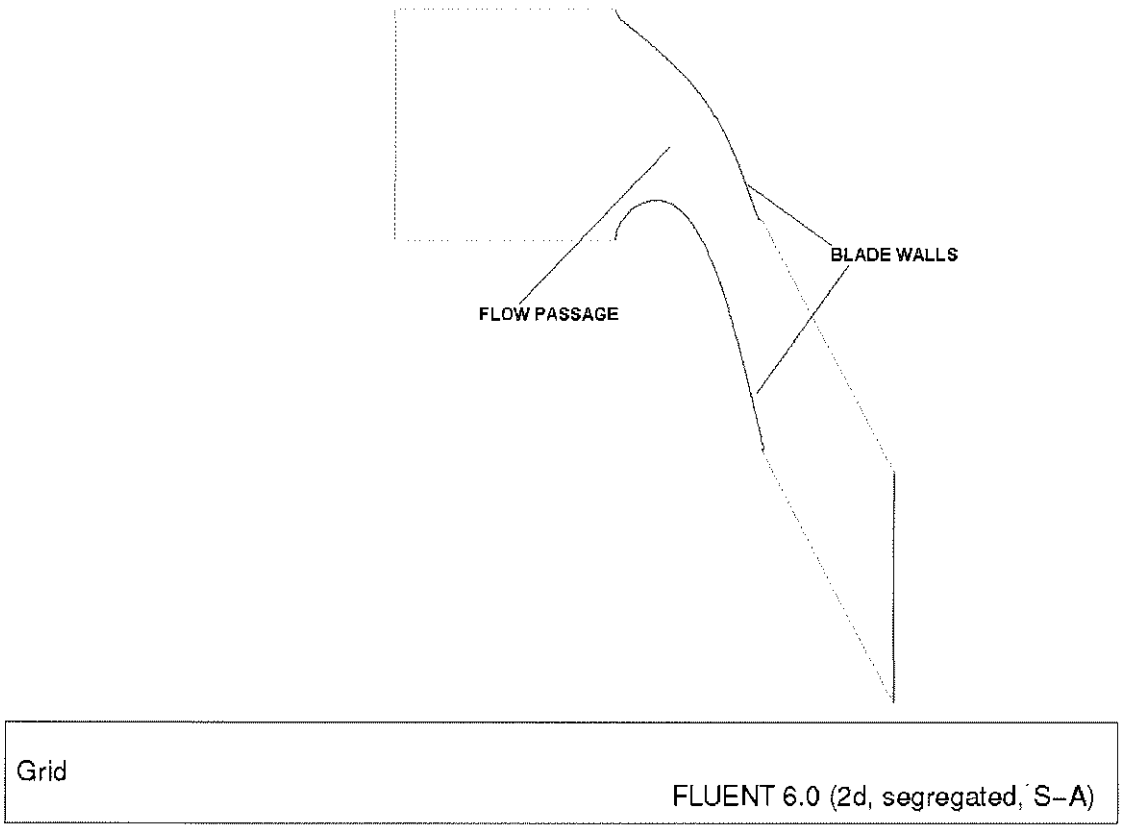

Figure 3.1 – Geometric configuration of model

The physical cascade geometry has been obtained from VKI [36]. The geometric configuration of the model is shown in Figure 3.1. The test conditions have been used as the simulation boundary conditions for the

numerical model. A steady-state simulation has been conducted as experimental results given are for this condition. Only flow has been modelled in this simulation. The physical blade was not modelled and no temperature distribution within the blade solid was solved for. Only a one-equation turbulence model has been used to investigate its accuracy. The simulation results compares heat transfer coefficients on the blade pressure and suction sides.

3.2 Computational Grid

Figure 3.2 shows the computational grid for the problem considered.

Figure 3.2 – computational grid

It is of vital importance that the blade is correctly defined. It has been found that poor blade shape definition leads to severe oscillations in heat transfer [34]. The blade shape was generated through use of the manufacturing coordinates [33] using FLUENT's pre-processor GAMBIT. The grid shown was the one used to obtain the final solution. The convergence plot of the

solution is shown in Figure 3.3. The graph shows the percentage deviation decreasing as the residual decrease.

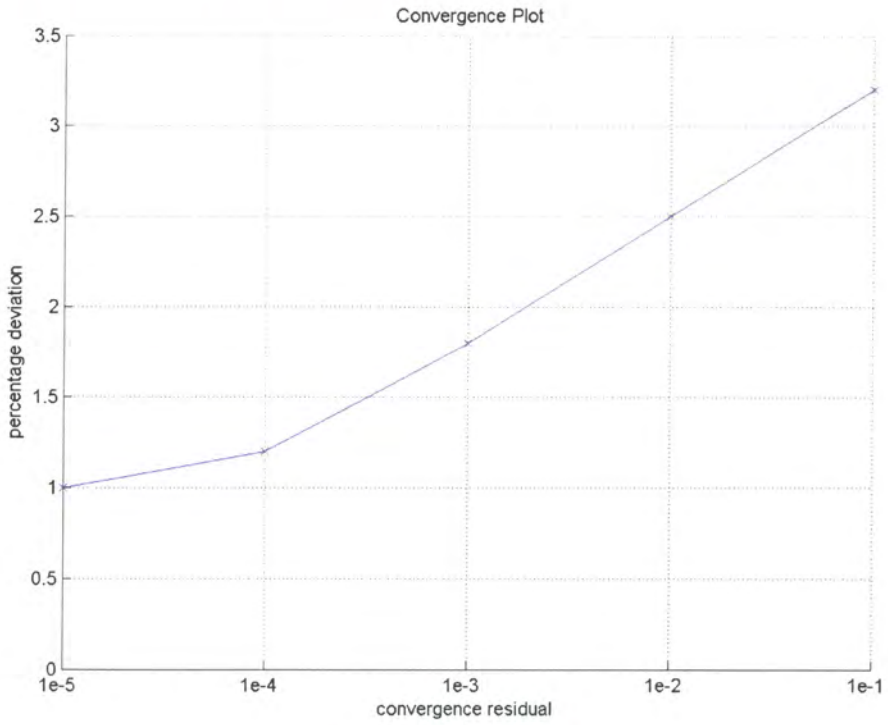

Figure 3.3 – Convergence criteria

A close up view of the grid near the wall region is shown in Figure 3.4.

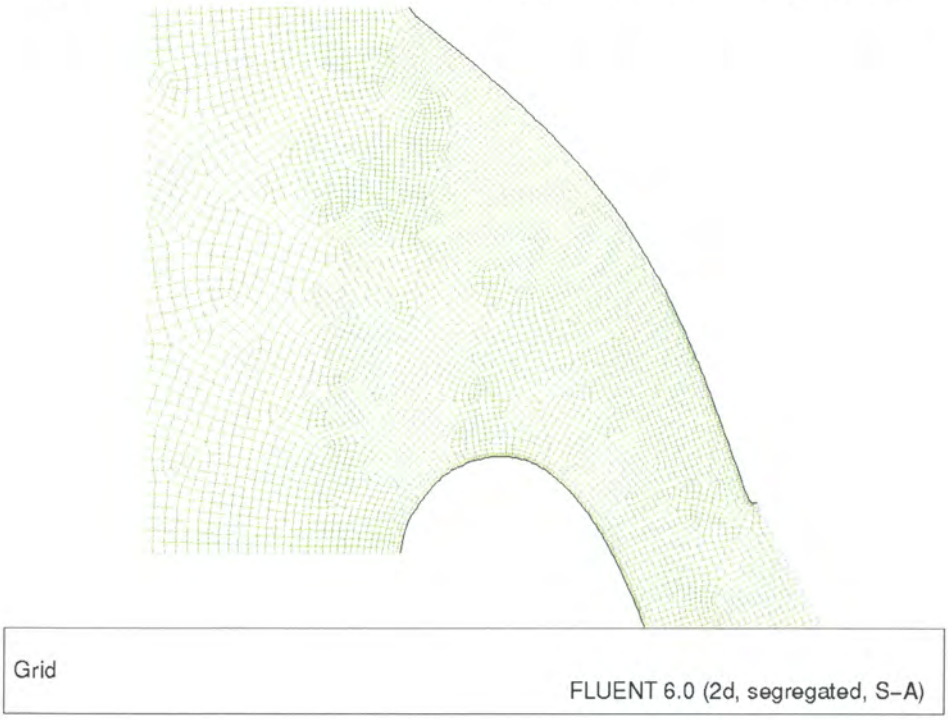

Figure 3.4 – close-up view of grid

3.3 Boundary Conditions

The boundary conditions implemented were according to the experimental set-up. No blades have been modelled in the cascade. Therefore, to obtain more accurate results, as that for a real life turbine cascade, periodic boundary conditions have been used. Flow periodicity has been ensured during the experiments conducted at VKI by means of wall static pressure measurements and Schlieren flow visualisations [33]. It was important to model the flow of the fluid in the simulation as compressible. This implied that the fluid medium (air) was modelled according to the ideal gas law. This is because transonic flow can occur, thus it is necessary to account for that possibility. A pressure inlet and pressure outlet was used as required by the CFD code for modelling of compressible flows.

Figure 3.5 depicts the boundary types.

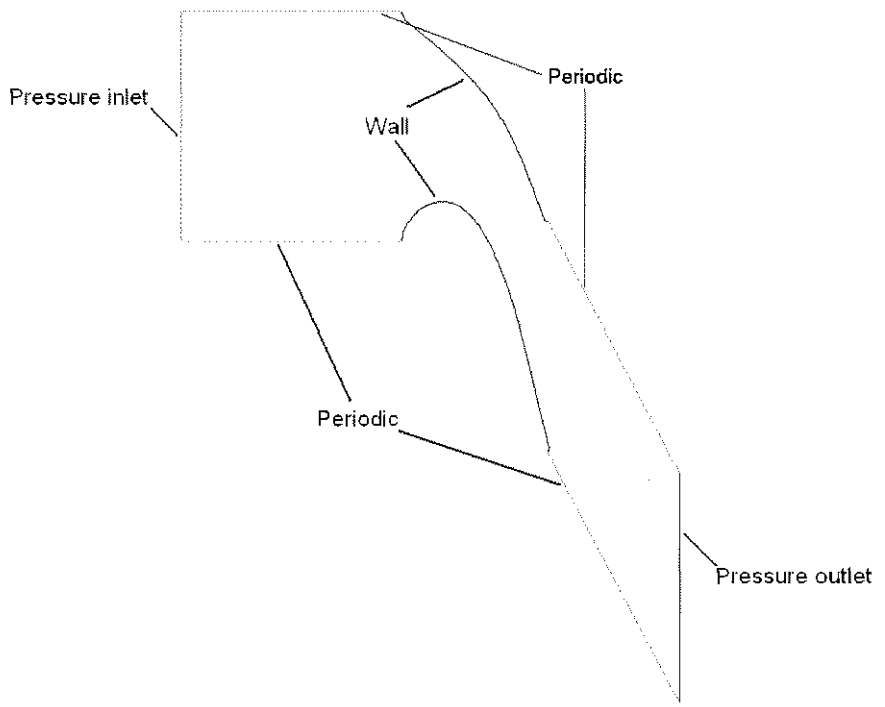

Figure 3.5 – Boundary types

A wall temperature of 302.15 K was specified for the blade whilst the total inlet pressure was 3.395 bar. The static inlet pressure was 3.342 bar and outlet

static pressure was 1.96 bar. A free-stream turbulence intensity of 1% as measured in the experiment was also taken into account.

The experimental data gave the properties of the working medium (air). These properties were:

- Density
- Dynamic viscosity
- Kinematic viscosity

Density was modelled using the ideal gas law whereas the dynamic and kinematic viscosities were modelled as constant values.

3.4 Results

The goal of this study as stated earlier was to obtain accurate prediction of the heat transfer coefficients of the blade surface. The heat transfer measurements in the experiments were conducted by means of 45 platinum thin films. These were located on both the suction and pressure surfaces of the blade. Their positions were given by means of coordinates with the stagnation point on the blade as a reference. It was necessary to create these points on the blade surface in order to obtain the heat flux at that point. The heat flux was thus, obtained from the simulation. It was in turn used to calculate the heat transfer coefficient through use of equation (3.1):

$$h = \frac{q_w}{T_{01} - T_w} \tag{3.1}$$

T_{01} and T_w are the total inlet temperature and wall temperature respectively. The heat transfer coefficients were hence calculated and plotted against the experimental values.

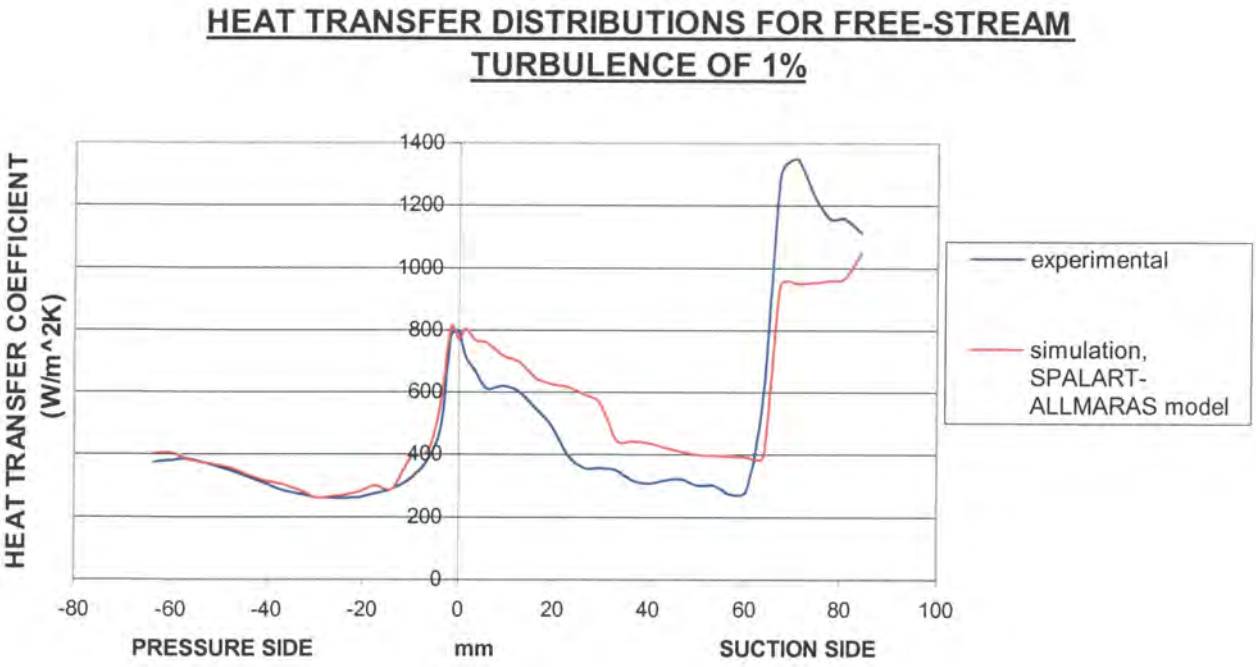

Figure 3.6 – heat transfer results

From the heat transfer results it is immediately seen that there is good agreement with the experiment on the pressure side of the blade. However, the heat transfer coefficient is over-predicted over the first section on the suction side of the blade. At this location a sudden *jump* occurs in the heat transfer coefficient and thereafter the heat transfer coefficient is under-predicted.

At this point, it is important to explain the sudden increase in the heat transfer rate on the suction side of the blade. This is best explained by examining the Mach number contours shown in Figure 3.7.

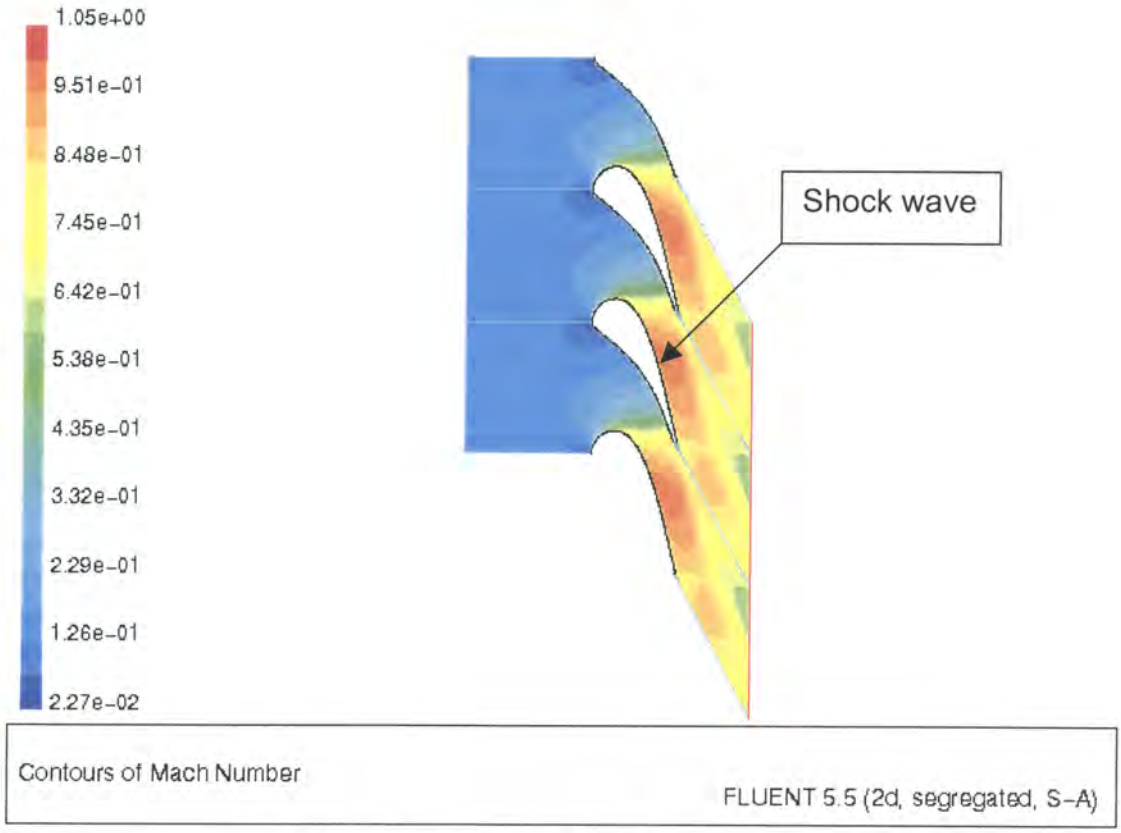

Figure 3.7 – Mach number contours

It is clear from the Mach number contours that the flow was in fact transonic. As the flow passes through the throat section, it accelerates to supersonic conditions. When returning back to sub-sonic conditions, a shock develops that causes the sudden increase in heat transfer coefficient. The velocity vectors in the corresponding section are shown in Figure 3.8 with a close-up view in Figure 3.9. These views show clearly that no flow separation occurred in area around the shock. This is consistent with the Schlieren visualisations conducted in the experiment [33]. A shock wave was seen to form on the suction surface, but no definite separated flow regions could be clearly identified. Thus, the shock wave has *tripped* the flow from laminar to turbulent resulting in the increase in heat transfer coefficient at this location.

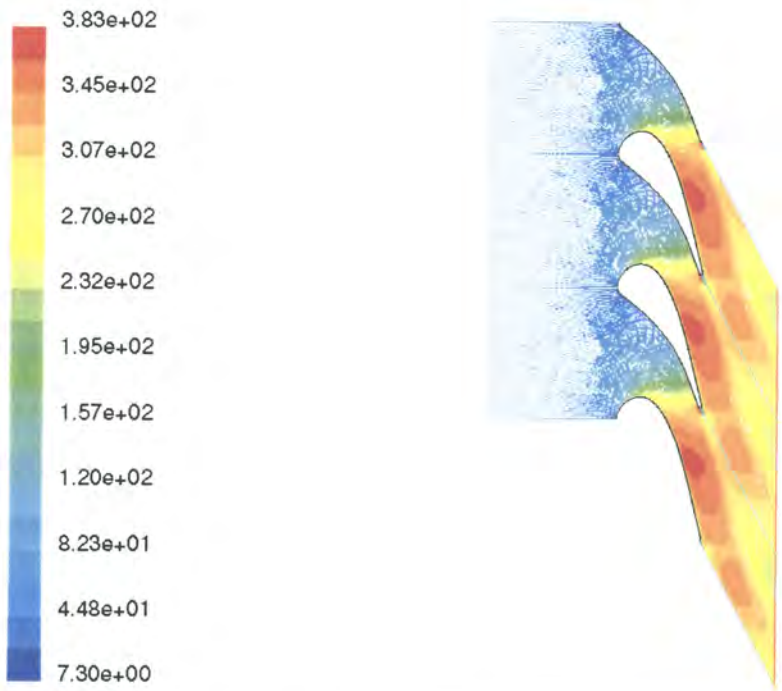

Figure 3.8 – Velocity vectors

The numerical model fails to predict the heat transfer accurately on the suction surface. The phenomenon of transition reduces the level of accuracy of predicting heat transfer. This is possibly due to the simple one-equation approach used to solve for the turbulence, which does not resolve the boundary layer accurately. Thus at the point where transition to turbulent flow occurs, the turbulence model does not sufficiently capture the heat transfer distribution.

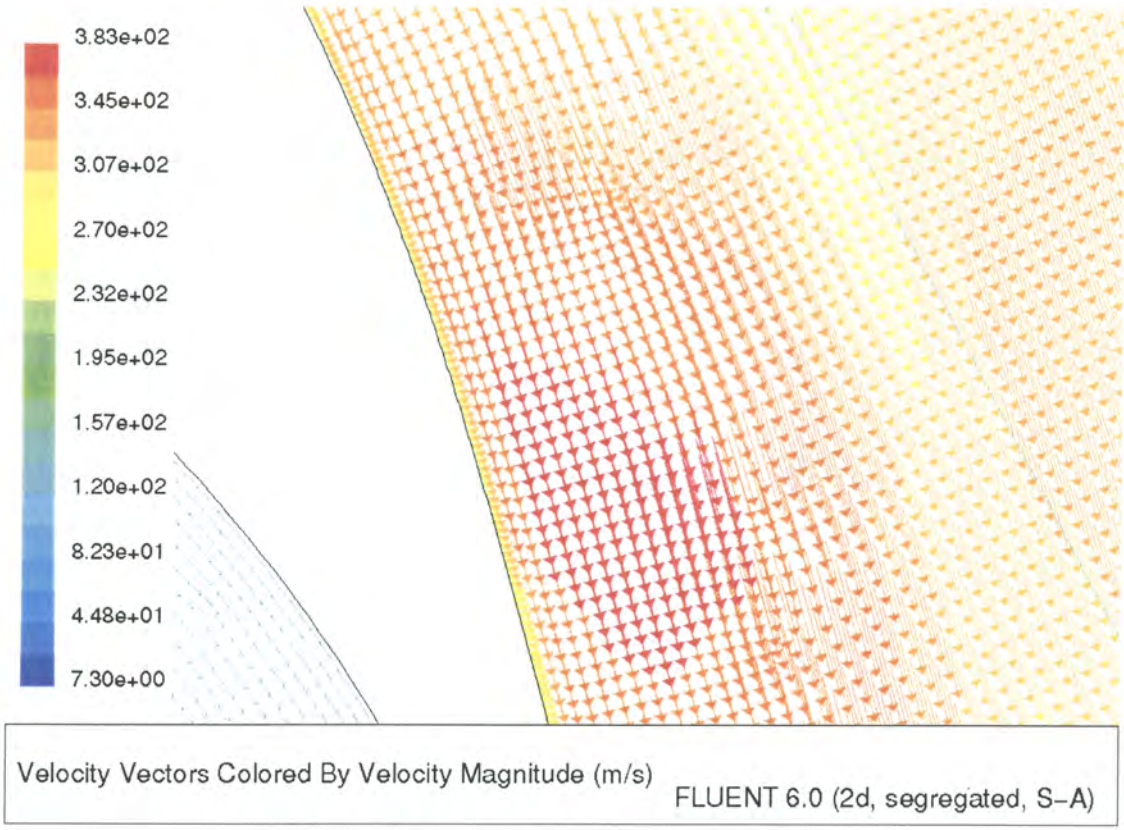

Figure 3.9 – close-up view of velocity vectors

3.5 Summary

A heat transfer analysis was conducted on a turbine nozzle guide vane cascade. The purpose was to investigate the one-equation turbulence model to accurately predict the heat transfer. The numerical modelling results were validated against the experimental results conducted at VKI. The heat transfer was predicted with fair accuracy on the pressure side of the blade but the accuracy was reduced on the suction side. The presence of a normal shock was predicted in the numerical model, but the heat transfer results were not in agreement with the experimental data. The use of the one-equation turbulence model has shown the correct trend of the experimental results. The analysis now needs to be further extended to include different turbulence models as well as solving for the thermal stresses.

Chapter Four

Heat transfer and thermal stress in a 2D turbine nozzle guide vane

This chapter analyses heat transfer and thermal stress modelling on a cooled two-dimensional nozzle guide vane. It presents the computational grid, boundary conditions as implemented in the numerical model and results of the analysis. Thermal stresses as a result of the temperature distribution have been computed. The heat transfer results were compared against experimental data.

4.1 Preamble

In this chapter a well-documented case study of a cooled turbine blade is simulated and compared to existing numerical data as well as experimental data. The case study was found from the literature and is known as *MARKII* [3]. Both thermal and stress data is available and can be used for validation of current simulations. The application is shown in Figure 4.1. Boundary conditions and set-up of the numerical model is similar to that conducted by Bohn et al. [3]. The study consists of two phases. Firstly the temperatures and pressures on the blade were computed. This study included the blade solid, so that a temperature distribution within the blade was solved. The commercial CFD code **FLUENT** was used for this part of the study. Secondly the temperature distribution was exported to a structural solver in order to compute the thermal stresses. This part of the study was conducted through the use of **FIDAP**.

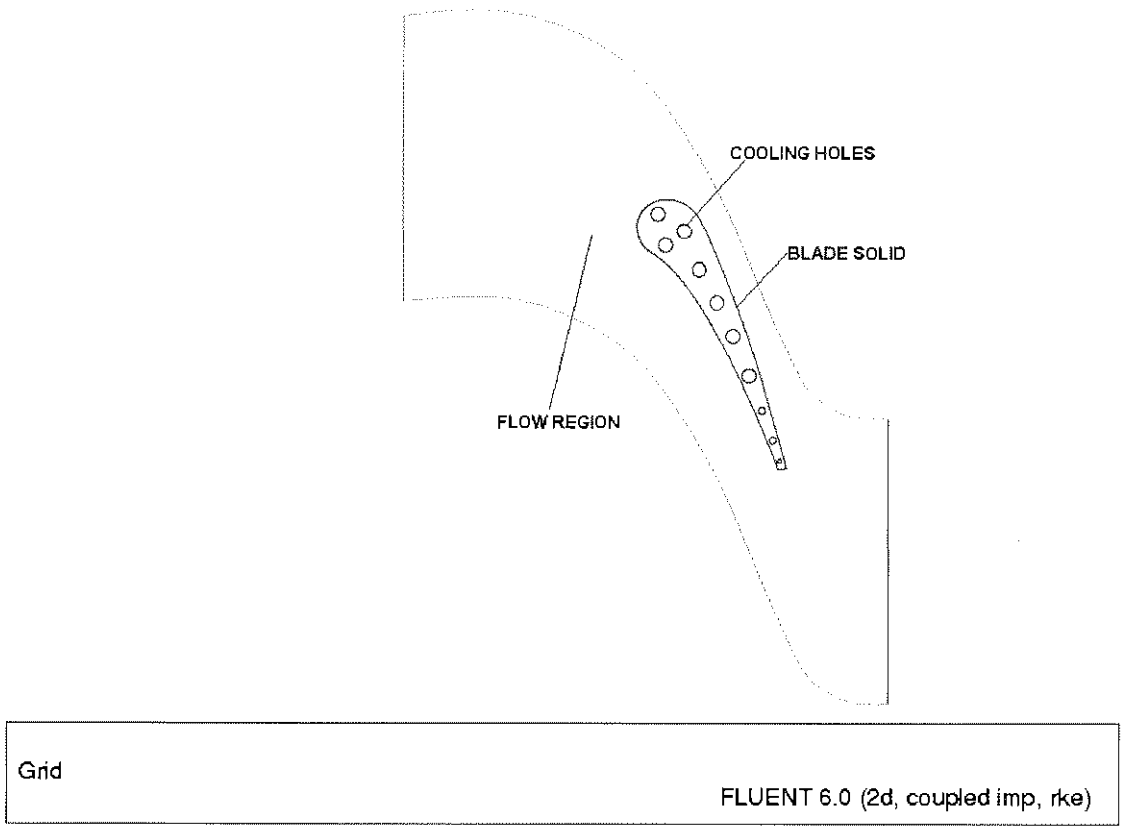

Figure 4.1 – Geometric Configuration of model

4.2 Computational Grid

The computational domain was divided into several smaller sections to enable a better quality grid to be applied on the blade. A 2-D grid consisting of 135 534 cells was generated with the worst equi-angle skewness measured as 0.73 and the worst aspect ratio as 9.43 as shown in Figure 4.2.

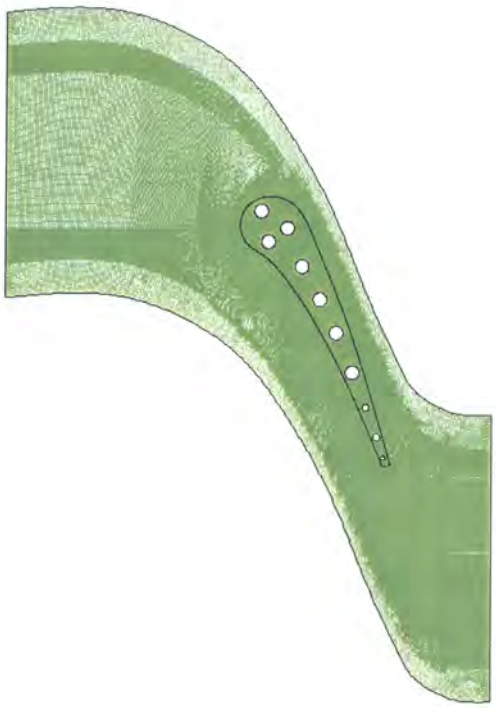

Figure 4.2 – computational grid

In generating the mesh, it was important to balance the cell densities in the fluid and solid regions. This is important to obtain the correct conjugate heat transfer from the blade surfaces. Therefore the transition in cell size from the fluid zone into the solid zone must match and all changes in cell size must be gradual. Equally important is the number of grid cells in the boundary layer to ensure that the grid resolution is adequate to capture both the flow and thermal boundary layers. The fact that an adapted grid could not be exported to FIDAP also eliminated that option due to the creation of hanging nodes in

an adaption process. Therefore a fine grid was necessary for the correct y^+ criteria to be met for the accurate determination of the surface heat transfer.

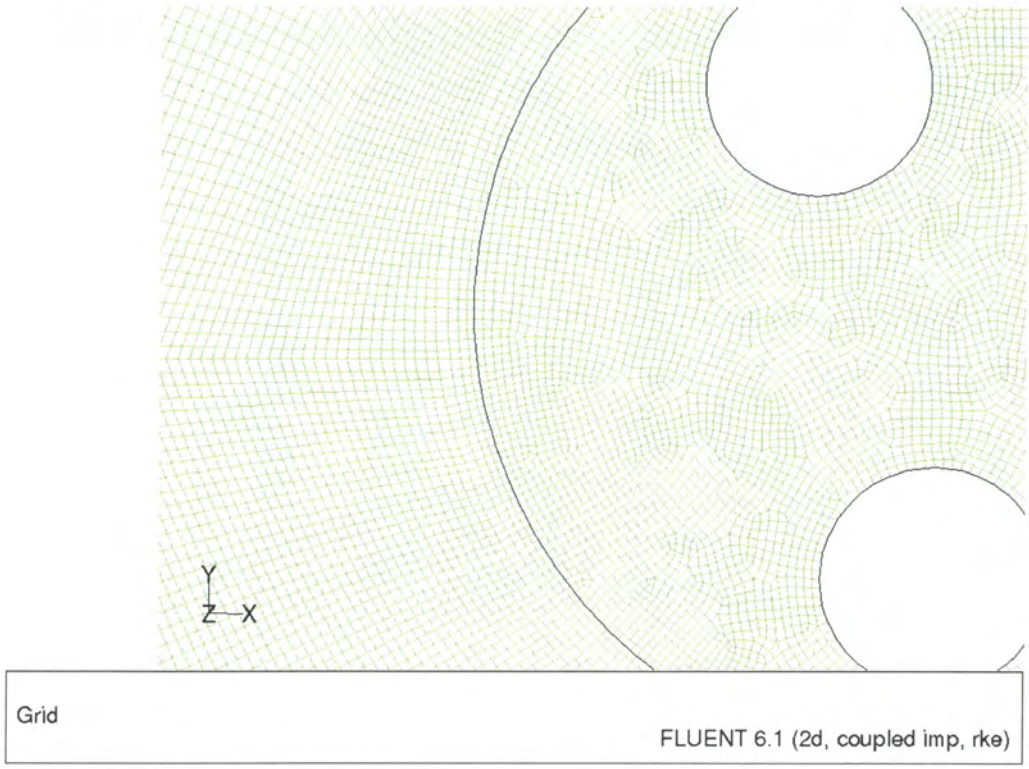

Figure 4.3 – computational grid in the vicinity of cooling holes 1 and 2

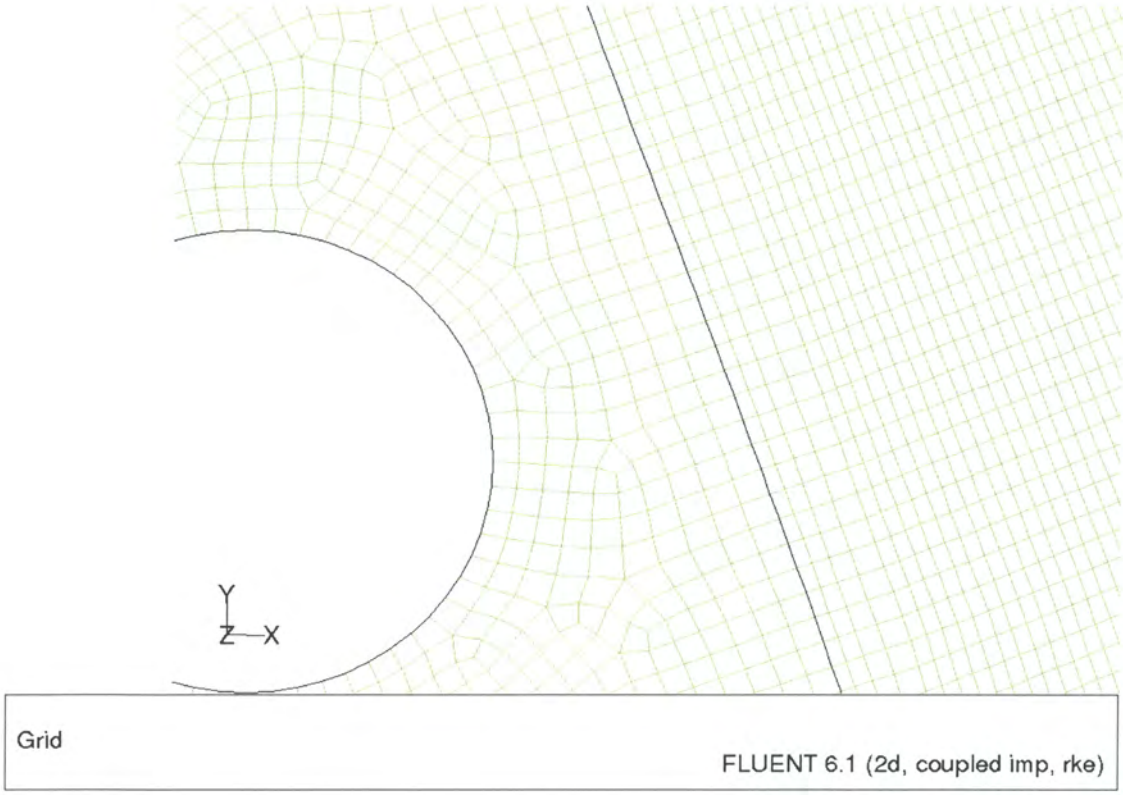

Figure 4.4 – computational grid in the vicinity of cooling hole 7

Figures 4.3 and 4.4 show that the mesh densities in the fluid and solid regions have been balanced in terms of change of grid cells. Also, only quadrilateral cells have been used in the entire computational domain. The blade interior has an unstructured grid due to the layout of the cooling holes that make building a structured grid a difficult task that leads to poor quality cells. The fluid region or blade exterior has a structured grid almost entirely. The division of the fluid region into smaller regions allowed this.

4.3 Boundary Conditions

The operating conditions were specified as supplied by the experimental study. The blade was internally cooled by means of ten round cooling holes through which cold air was passed. The boundary types are shown in Figure 4.5. The convective heat transfer coefficients were supplied for each cooling hole and are shown in table 4.1.

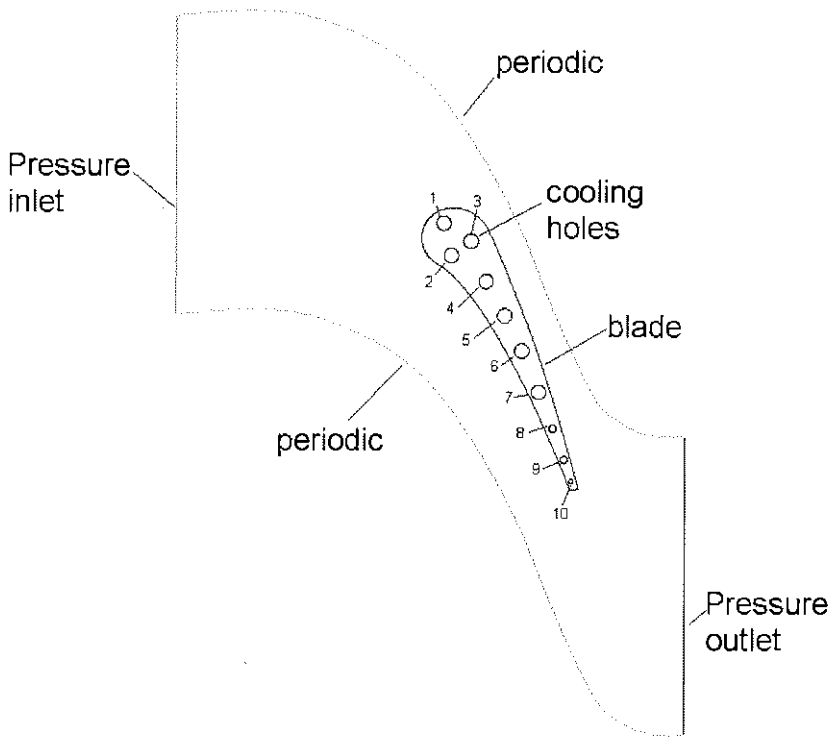

Figure 4.5 – general outline of MarkII blade

The *MarkII* blade was a transonic analysis. This implied that inlet and outlet pressures must be specified. Periodic boundaries are used to include the effect of other blades on the flow and heat transfer without having to actually model the other blades. The fluid was modelled as compressible.

Hole	Heat transfer coefficient	Coolant temperature
	[W/m^{2}K]	[K]
1	1943.67	336.39
2	1881.45	326.27
3	1893.49	332.68
4	1960.62	338.86
5	1850.77	318.95
6	1813.36	315.58
7	1871.88	326.26
8	2643.07	359.83
9	1809.89	360.89
10	3056.69	414.85

Table 4.1 – Convective heat transfer coefficients for cooling holes

The following conditions were implemented:

INLET:

Total inlet pressure = 334 000 Pa	Total inlet temperature = 788 K
Inlet Mach number = 0.19	*Inlet static pressure = 325695 Pa

*The static inlet pressure was calculated assuming isentropic flow and ratio of specific heats of air taken as, k=1.4 through equation (4.1)[37]:

$$\frac{P_o}{P} = \left[1 + \frac{1}{2}(k-1)M^2\right]^{\frac{k}{k-1}} \qquad (4.1)$$

OUTLET:

Outlet static pressure=167000 Pa	Outlet Mach number=1.04

Air properties were obtained from [32] and modelled as temperature dependent. In order to calculate the temperature distribution within the blade, it is necessary to specify its properties. In this case the blade was fabricated from 310 stainless steel [39]. The following properties were modelled as temperature dependent: thermal conductivity, thermal coefficient of expansion and Young's Modulus. Details of the temperature dependent properties can be found in Appendix A. The following material properties were modelled as constant:

C_p=502 J/kgK	ρ=7750 kg/m^3
υ=0.31	

4.4 Thermal Results

The study was conducted in two different stages. The first was the flow and heat transfer problem for which FLUENT was used and the second was the determination of the thermal stress for which FIDAP was used. The simulation results were compared to the available experimental data. The accuracy of the temperature distribution is also important because it has a direct bearing on the thermal stress distribution. Hence, if the temperature distribution is inaccurate, it will result in an inaccurate thermal stress distribution. Since the complete analysis was conducted in two steps, it was required to export the results from FLUENT (flow solver) to FIDAP (structural solver). The reason for not solving both the fluid and structure in FIDAP was due to the fact that the flow was transonic which FIDAP cannot handle. Details of the routine used to export the boundary conditions from Fluent to Fidap can be found in Appendix B. A coupled implicit solver was used for all the analyses. This means that the continuity and momentum equations are solved simultaneously. This is a recommended solver for compressible flow. The main control over the time stepping scheme is the *Courant* number.

The first solution made use of the one-equation *Spalart-Allmaras* turbulence model. The horizontal axis (x) is the distance along the blade curvature. Figure 4.6 shows the static pressure distribution over the blade surfaces.

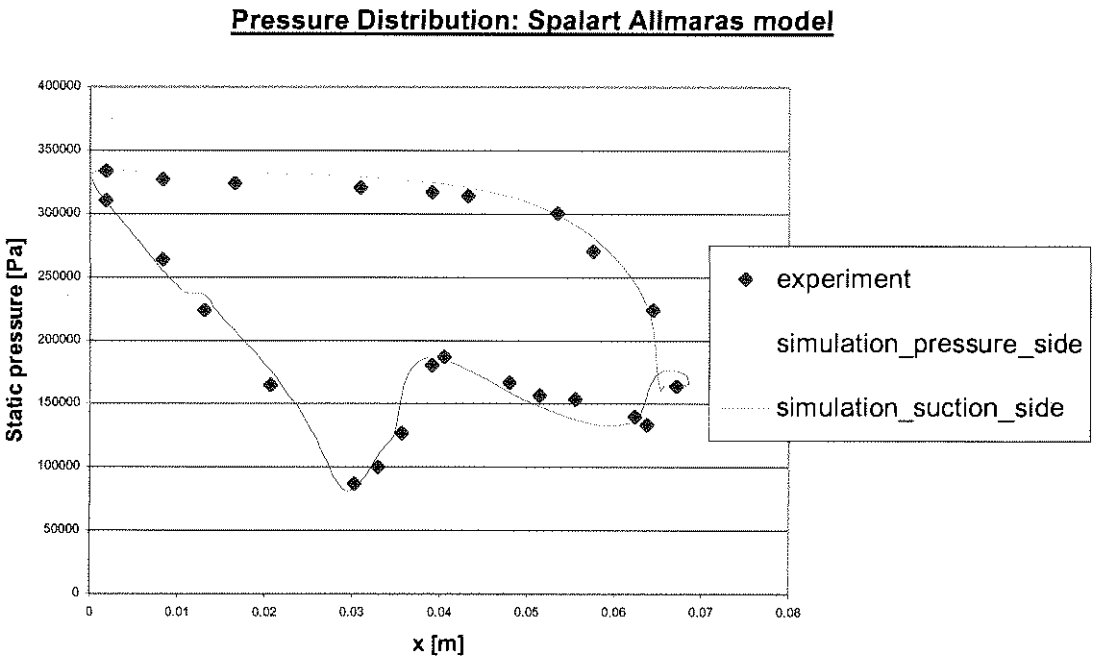

Figure 4.6 – Pressure distribution: *Spalart-Allmaras* model

Figure 4.6 shows reasonable accuracy in predicting the pressure distribution around the blade as well as the shock wave, which occurs on the suction side of the blade. The maximum error on the pressure side is just under four percent. The maximum error on the suction side is nine percent. This is however only on two points: x=0.036m and x=0.056m. The other points have an error of less than five percent. The general trend of the simulation follows the experiment well. From this result one can therefore conclude that the grid was adequate to capture the boundary layer in the flow.

The temperature distribution over the blade surface using the *Spalart-Allmaras* model is shown in Figure 4.7. The pressure side exhibits the trend well, although the temperature is over-predicted. The fluctuating temperature distribution is closely followed. The peaks of the fluctuating temperature of the simulation and experiment do not occur at the same position. This can be

explained by the prediction of the stagnation point to be slightly different from that determined in the experiment. The simulation predicts the position of the stagnation point to be 0.002695m; instead of zero. Hence there is a phase shift in the temperature distribution on both the pressure and suction sides. The average error on the pressure side is seven percent. There are several explanations for this behaviour. The first possibility is that the grid close to the wall is not fine enough to capture the thermal boundary layer. The strongest possibility is, however, the well-published fact that this turbulence model tends to over predict the heat transfer at the wall and therefore the wall temperature.

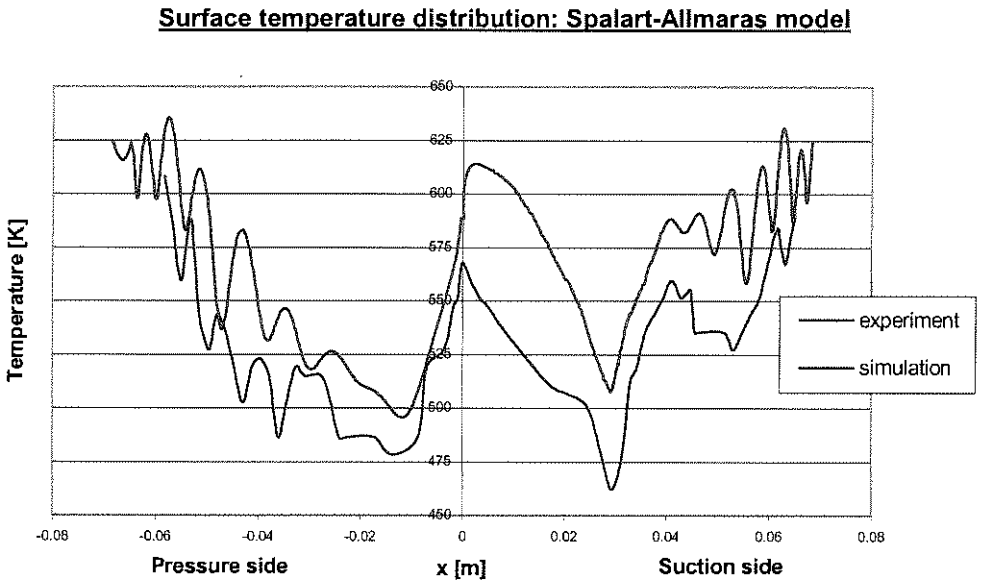

Figure 4.7 – Temperature distribution: *Spalart-Allmaras* model

The suction side temperature distribution also follows the experimental trend well. The average error is eleven percent. The decrease in fluid temperature together with the high heat transfer as a result of the cooling holes results in the rapid decrease of surface temperature up to the position x=0.3m. A sharp increase in fluid temperature at that point is due to due to a shock that breaks up the relatively thick boundary layer at that point and therefore increases the heat transfer rate. The fluctuating temperatures on both sides occur as a result of the cooling holes.

Since the heat transfer calculations are directly linked to the turbulence model, the *realizable* k-ε model using enhanced wall treatment was also used for the

analyses. The main difference between the two turbulence models with regards to the particular blade analysed are:

- The pressure distribution is better predicted with the *realizable k-ε* model than the *Spalart-Allmaras* model, especially the second, weaker shock wave
- The overall average error of the *realizable k-ε* model using enhanced wall treatment is slightly less than that of the *Spalart-Allmaras* model
- The stagnation point predicted through the *realizable k-ε* model is closer to the experimental position than the *Spalart-Allmaras* model

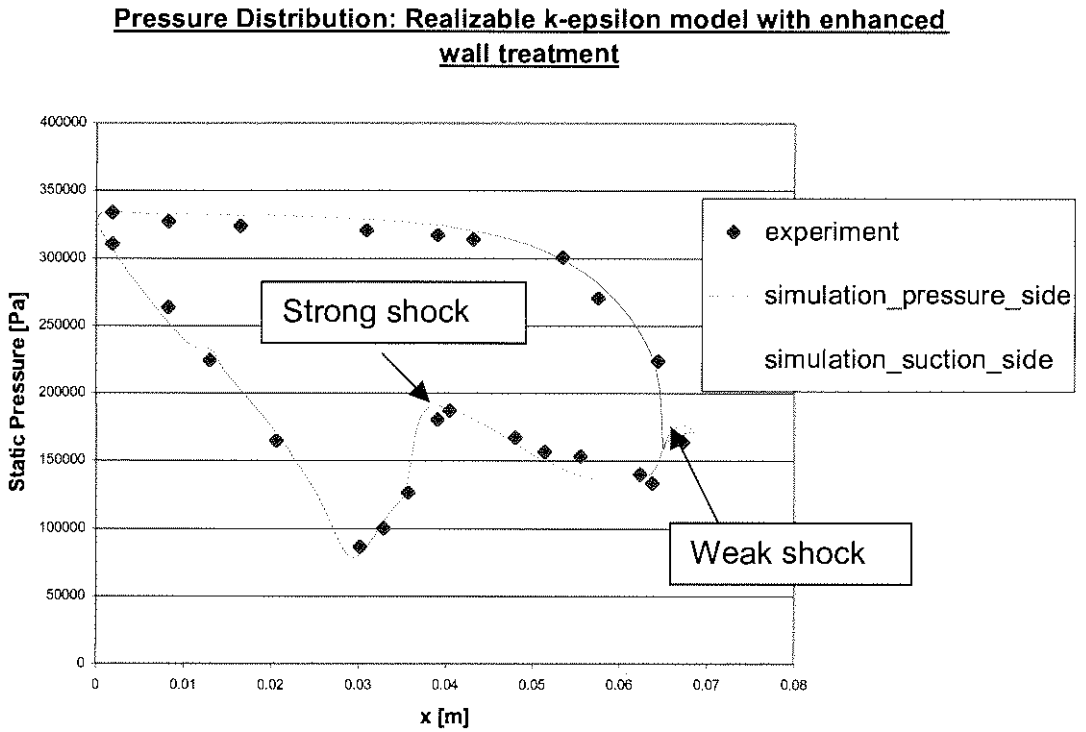

Figure 4.8 – Pressure distribution: *Realizable k-ε* model, enhanced wall treatment

Figure 4.8 shows the pressure distribution over the blade. The average error margin on the pressure side is three percent. The error margin on the suction side is slightly higher at five percent. Only one point on the pressure side is outside this margin. The point at x=0.055m is out by eight percent. The model also captured the shock wave accurately. The mach contours presented in Figure 4.9 show the presence of a strong shock wave just past the leading

edge on the suction side. The high-pressure ratio and large reduction of the flow area cause the flow to accelerate up to a maximum of Mach 1.39. This shock is evident in the pressure plots shown previously. There is also a second milder shock occurring just before the trailing edge on the suction side where the flow reaches Mach 1.2 approximately.

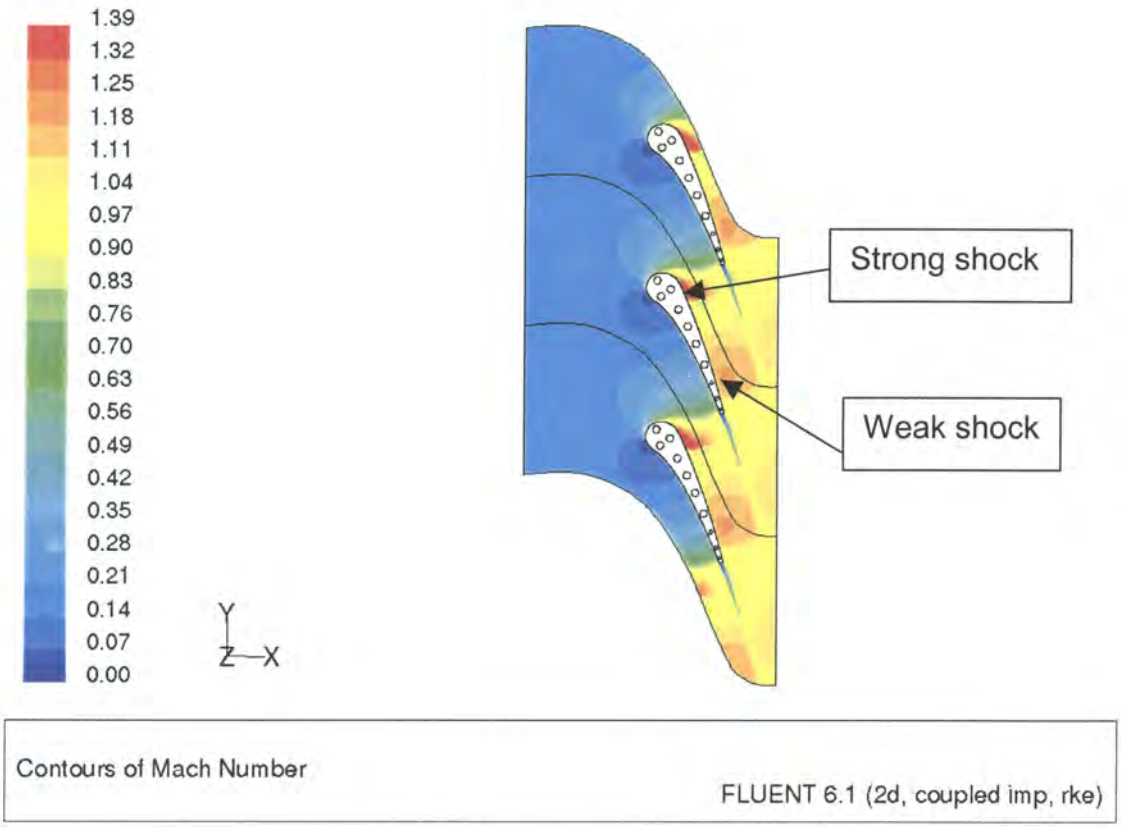

Figure 4.9 – Contours of Mach number

Figure 4.10 shows the temperature distribution over the blade surface. The general trend is well predicted, in particular the temperature fluctuations that are more prevalent on the pressure side. The average error on the pressure side is seven percent. The error on the suction side is of the same order. Although a 7% difference appears large, it is about as accurate as one can get when using standard turbulence models. The common assumption is that it is not possible to obtain temperature results with an accuracy of less than 10% when using standard turbulence formulations. At the time of this study other turbulence models were not available, but it has been claimed that when

using the k-ω turbulence model or the V2F turbulence model, the accuracy can be improved to less that 10%.

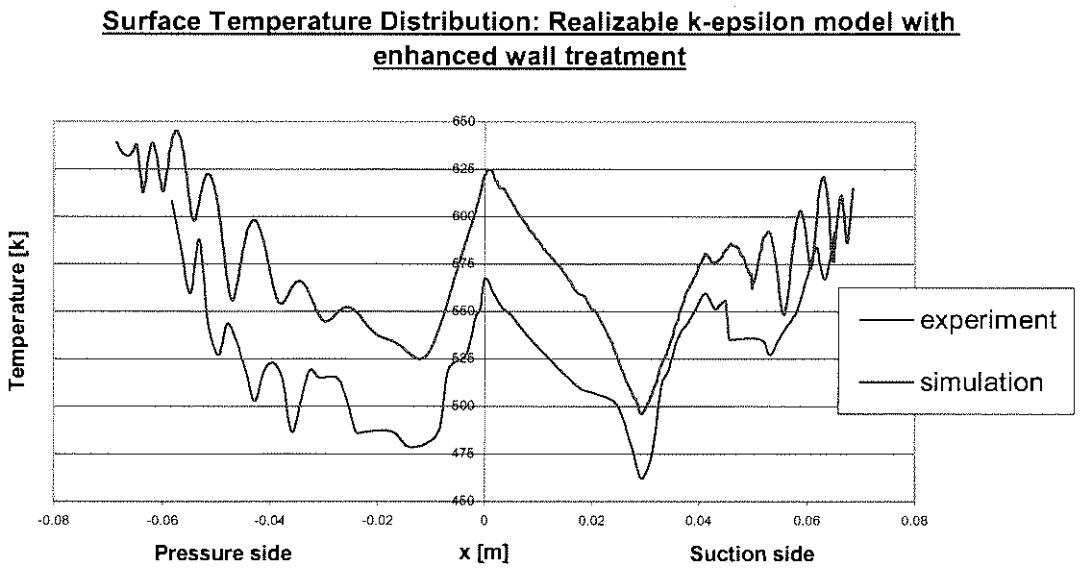

Figure 4.10 – Temperature distribution: *Realizable k-ε* model, enhanced wall treatment

A major contributing factor for the temperature distribution within the blade solid is the thermal conductivity values. The values used in this study were obtained from literature and may be different from the values used for the experiments [3]. An inaccuracy in the material properties will also have an effect on the thermal gradient in the blade and therefore the surface temperature on the blade.

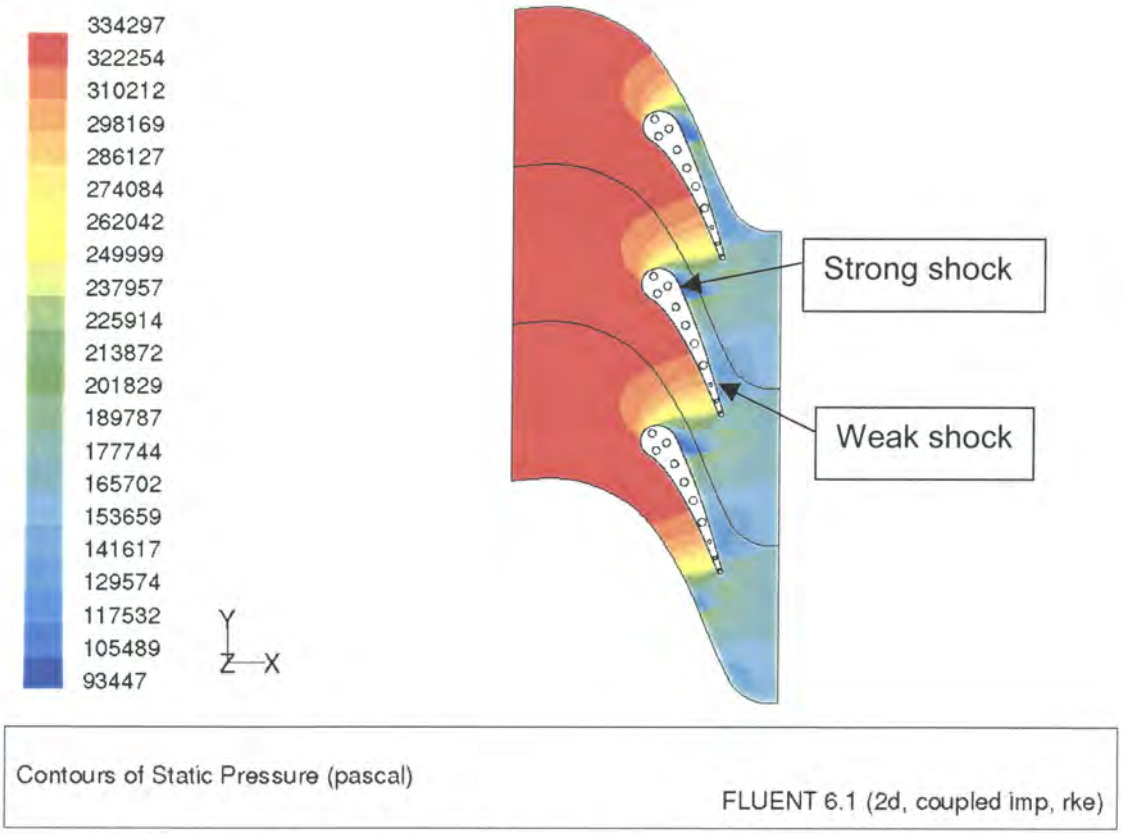

Figure 4.11 – Contours of Static pressure

Figure 4.11 shows contours of static pressure over three blades when using the *realizable* k-ε model. The presence of a strong shock wave can be seen just past the leading edge on the suction side of the blade. There is a sudden drop in static pressure at this point. A second much weaker shock is seen to form towards the trailing edge of the suction side, as a drop in pressure is also present.

The temperature plot of the blade is shown in Figure 4.12, while Figure 4.13 shows the temperature distribution as obtained from the literature [3].

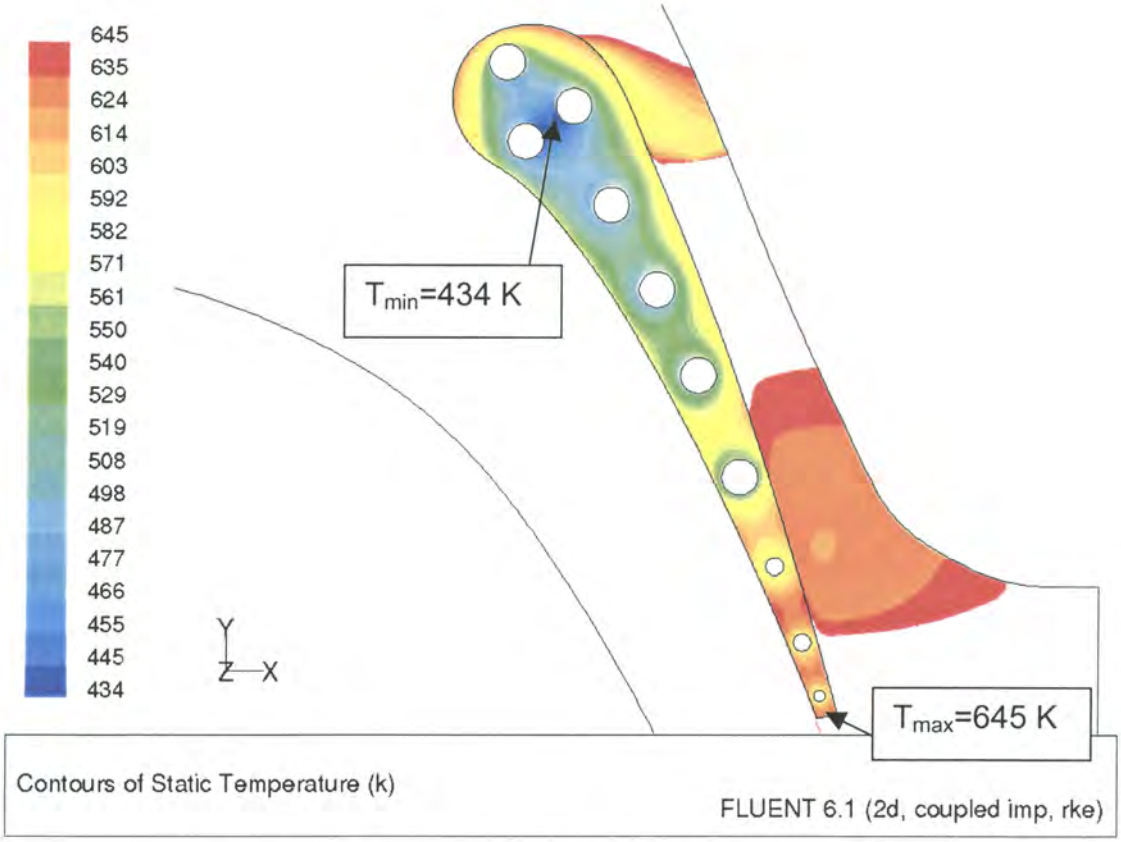

Figure 4.12 – temperature distribution inside the blade

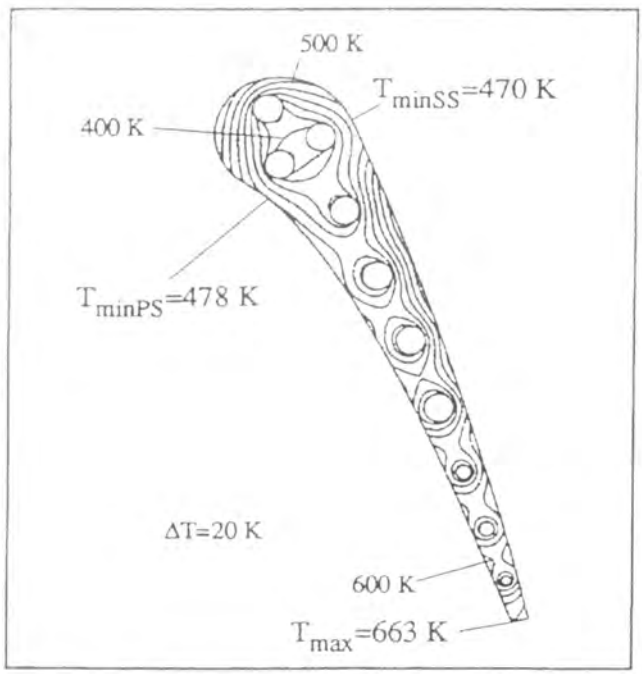

Figure 4.13 – Temperature distribution as calculated by Bohn et al. [3]

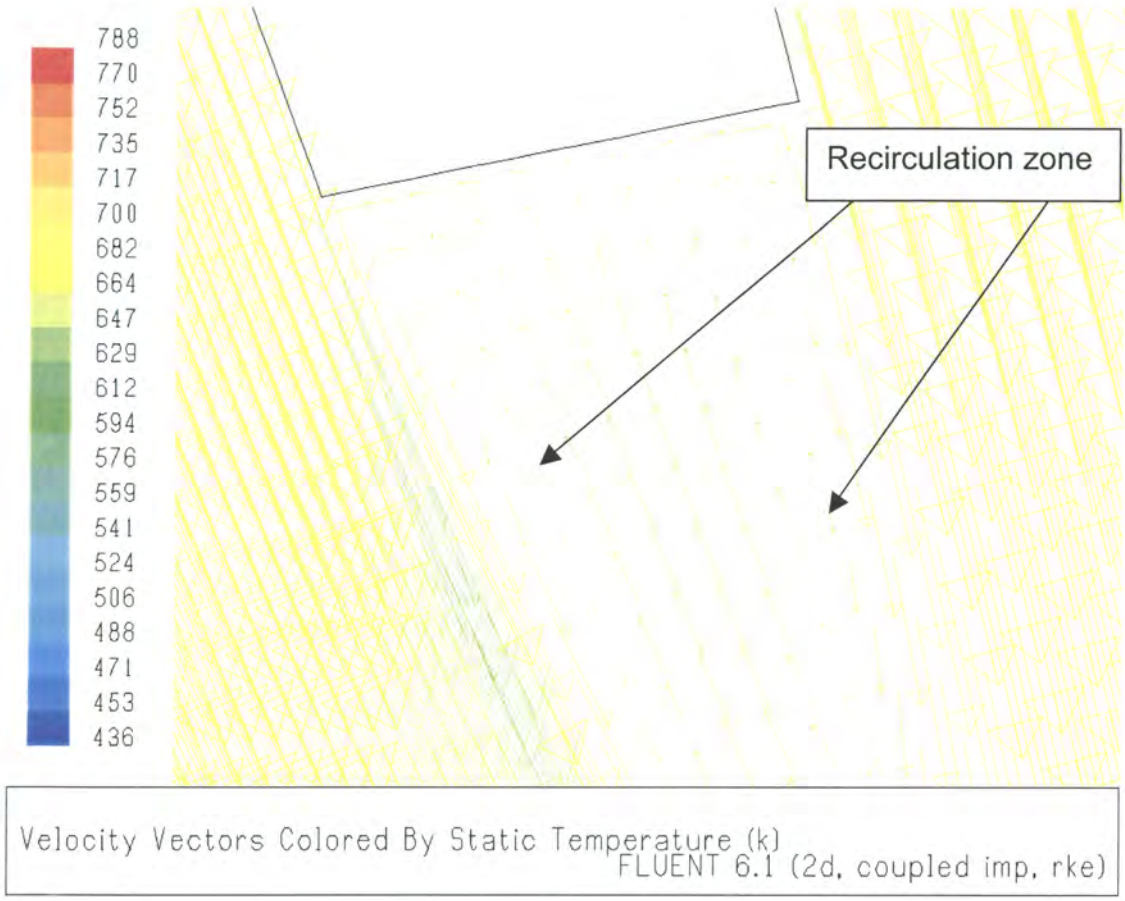

Figure 4.14 – contours of static temperature

The hottest section of the blade occurs on the trailing edge as the result of a recirculation zone at this point. The abrupt ending of the blade causes the recirculation zone and the breaking up of the boundary layer in that section as shown in Figure 4.14. Hence, a zone of hot air is *trapped* in this region with a high heat transfer rate resulting in a hot trailing edge. The highest temperature is 645 K and is close to the analysis of Bohn et al [3], in which the value was 663K, thus giving a difference of less than three percent. The minimum temperature was slightly higher in this analysis at 434K whereas Bohn recorded 400K an error of 8.5 percent. On the positive side, the location of the lowest temperature occurred in the same geometric area between cooling holes two and three in both simulations. This is due to the fact that both these holes have very high convective heat transfer coefficients and the material in between them is furthest from the hot air. This region is also where the highest temperature gradients occur, which shall have a bearing on the highest thermal stress.

4.5 Thermal Stress Results

The results obtained with the *realizable* k-ε turbulence model with enhanced wall treatment produced the most accurate results. Hence, the temperature distribution results are exported to the structural solver FIDAP in order to compute the resulting thermal stress. Thus the results presented show the thermal stress distribution as a result of temperature gradients only and not as a function of the fixation of the blade. The von Mises stresses are used as a criterion for failure. The method followed for stress calculation differs considerably from Bohn et al. as only the structure is solved and no conduction is solved for in FIDAP, the structural solver. This was permissible because of the ability to export the results from FLUENT to FIDAP. The results presented for the structural analysis are validated against those computed through the analysis of Bohn et al. No experimental results were conducted within the blade for temperature or stress purposes. Therefore, a comparison was made to the results of Bohn et al. for a cross section taken between cooling holes four and five. Figure 4.15 shows the distribution of Von-Mises stresses and the location of cross section A-B. Figure 4.16 shows von Mises stress distribution as computed by Bohn et al [3].

It is evident from the contours of von Mises stress that the highest stress occurs between holes two and three. This is consistent with the temperature distribution within the blade, where the highest temperature gradient also occurred in the same geometric location. The maximum stresses predicted in this study is, however, lower than what Bohn predicted. This is a direct result of the difference in the temperature distribution discussed in the previous paragraph. This proves the importance of an accurate temperature distribution in order to calculate the correct thermal stresses.

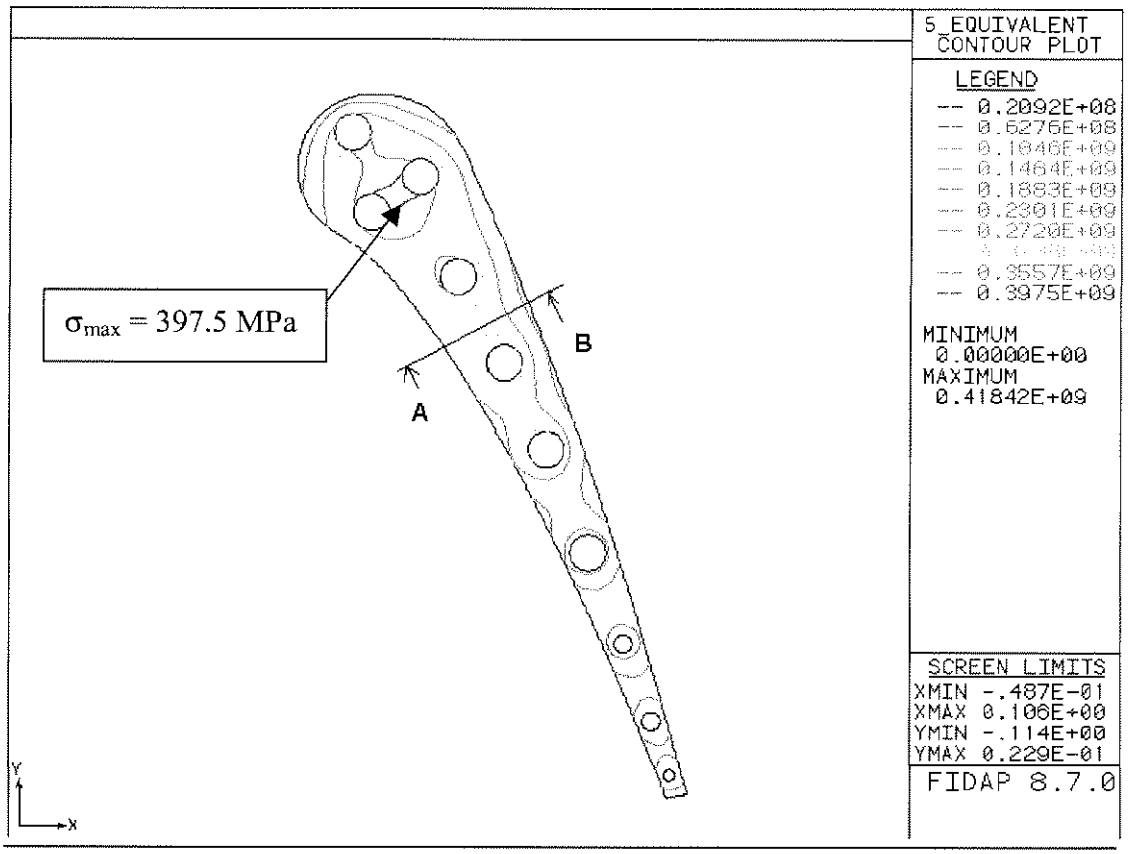

Figure 4.15 – Distribution of Von-Mises Stresses

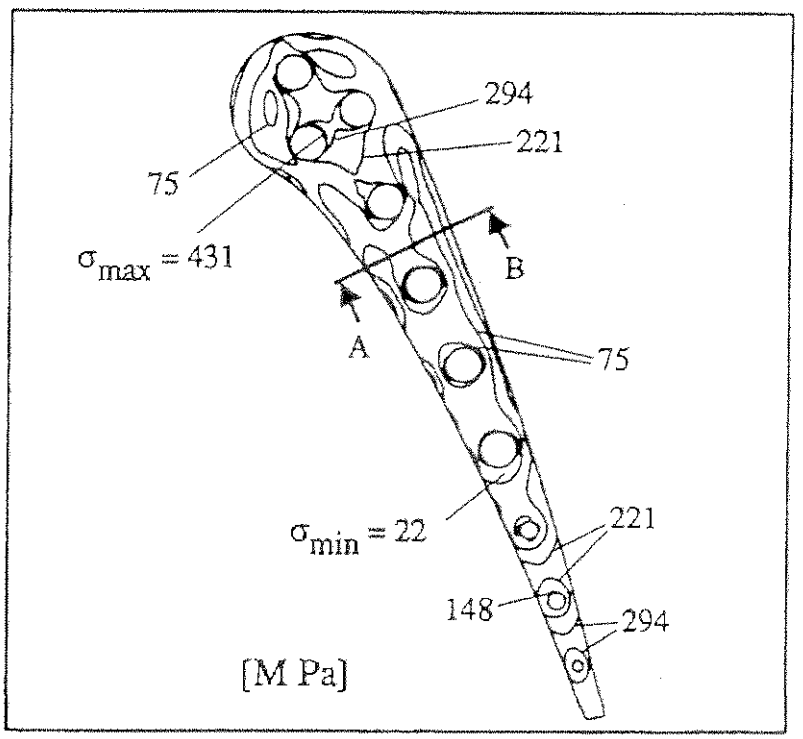

Figure 4.16 – Distribution of Von-Mises Stresses [3]

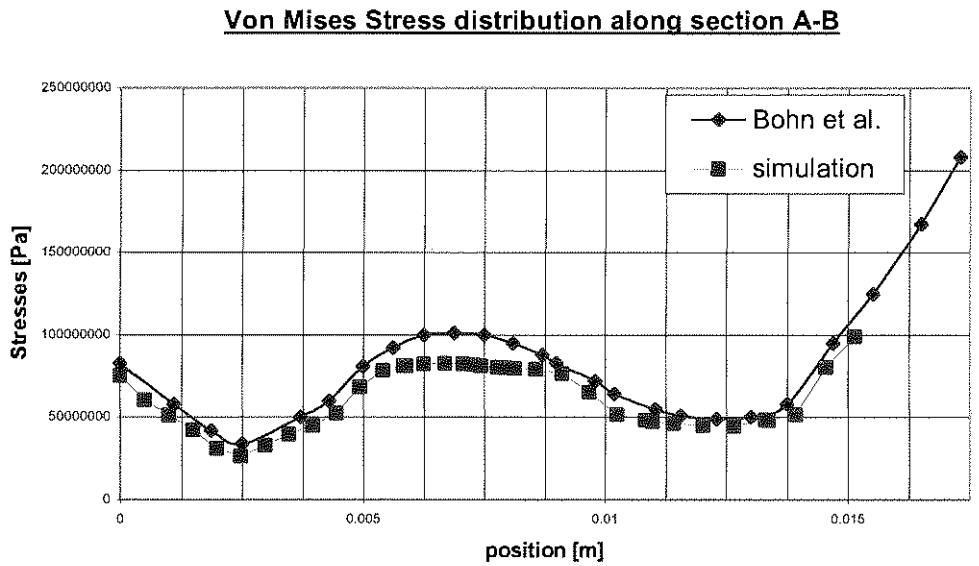

Figure 4.17 – Von Mises stress distribution along section A-B

The Von Mises stress distribution across section A-B, is shown in Figure 4.17. The general trend is well predicted over the section. The average error is twelve percent, mainly as a result of the difference in the temperature distribution. The stress is under predicted whereas the temperature distribution was over predicted. This is because the stress is a function of temperature gradient and if the temperatures are higher, it implies the gradients are lower, which results in lower stresses. This study has shown that the correct prediction of thermal stresses is not possible without predicting the correct temperature profile.

4.6 Summary

A combined heat transfer and thermal stress analyses was done on an internally cooled experimental nozzle guide vane. The study was conducted in two different phases. The first phase involved the solution of the flow and heat transfer over the nozzle guide vane. Two turbulence models were investigated to ascertain which model gave the most accurate results. The *realizable* k-ε model with enhanced wall treatment gave the most accurate results. The pressure distribution over the entire blade surface was well predicted, but the accuracy of the temperature distribution was not as good,

particularly on the suction side of the blade. The temperature results were exported to a structural solver in order to determine the thermal stresses in the nozzle guide vane. There was good correlation between the predicted thermal stresses to that presented in the literature. This was attributed to the good general temperature prediction trend. All the results were validated against data presented in literature.

Chapter Five

Analysis of a cooled 3D turbine nozzle guide vane

The heat transfer analysis of an internally cooled three-dimensional turbine nozzle guide vane is described in this chapter. The complete geometry, computational grid, boundary conditions and results of the analysis are presented. The heat transfer results were compared to data obtained from similar analyses.

5.1 Preamble

This section of the study extends the heat transfer analysis to three dimensions. The analysis has been conducted on a turbine nozzle guide vane of a commercial aircraft engine. This blade was chosen mainly due to the easy access to the detailed blade geometry and existing design data for the blade. The first phase of the study is to calculate the flow and heat transfer to the blade using FLUENT. As stated before, the emphasis will be on the accuracy of predicting the pressure distribution around the blade and the heat transfer from the fluid to the blade surface.

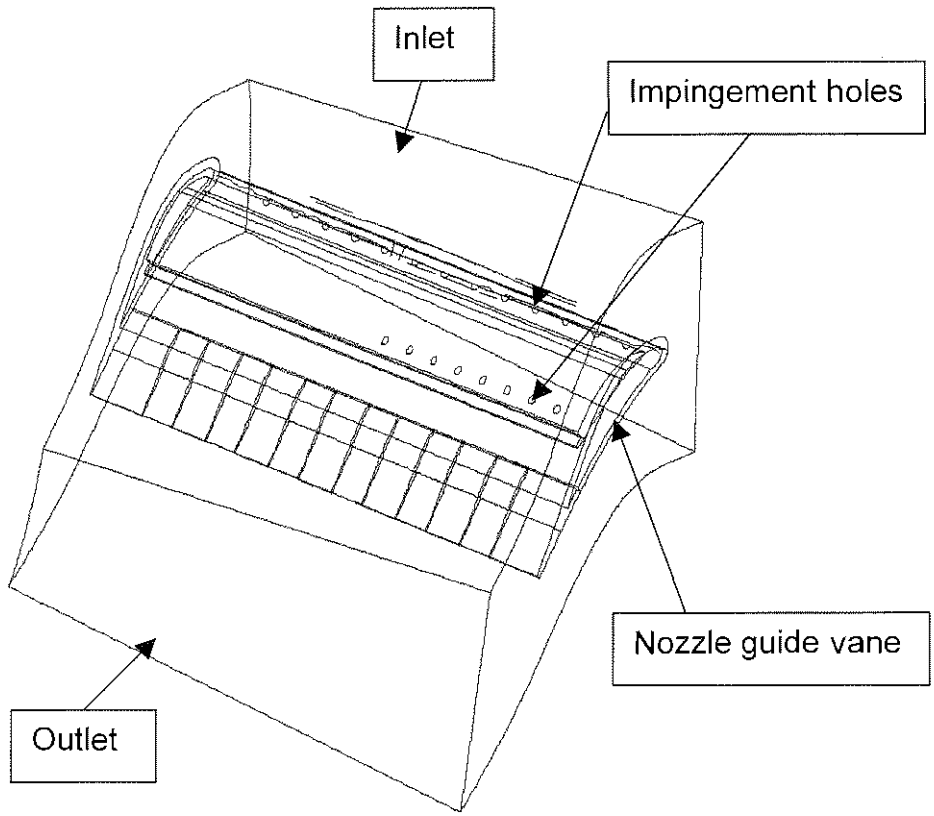

Figure 5.1 – Geometric configuration of the model

5.2 Geometric considerations

This analysis entails only one internally cooled nozzle guide vane. Cool air from the compressor is bled into an impingement-insert inside the blade from the hub side of the vane. The impingement-insert has several cooling holes that impinge the cool air onto the leading edge as well as the suction side of the blade. The cooling air then leaves the blade through thin slots towards the trailing edge of the blade. In the real engine there are forty-two nozzle guide vanes. Therefore, periodic boundary conditions are used to get the effect of the guide vanes on either side of the one being analysed.

5.3 Turbulence Model

The *realizable* k-ε turbulence model was used for the flow and heat transfer analysis. The main reason for this was because previous studies have shown this model to give the most accurate results of the standard turbulence models available, whilst being computationally constrained. Due to the size of the mesh, the *realizable* k-ε turbulence model with enhanced wall treatment could not be used. The mathematics describing the *realizable* k-ε turbulence model as well as its strengths and weaknesses was presented in chapter two. The non-equilibrium wall function approach was used in order to better predict any possible flow separation and/or reattachment. Also in the internal section of the blade where the coolant air impinges on the inner blade surface the non-equilibrium wall function is better equipped to handle such a flow.

5.4 Computational Grid

The complexity of the geometry required the use of tetrahedral cells for the dicretization procedure. A procedure similar to that applied in chapter four was used for the mesh generation process. Figure 5.2 shows the mesh used on the surface of the blade. Around the cooling slots on the trailing edge and the holes on the impingement insert special mesh refinement was required to capture the complex flow in this region. This is shown in Figures 5.3 to 5.5.

5.5 Boundary Conditions

The use of periodic boundary conditions meant that only one nozzle guide vane was analysed. For the flow domain a pressure inlet and pressure outlet boundary condition was used, while a mass flow inlet was used for the introduction of the coolant flow. Not all the values were readily available from the engine manual and several basic calculations were necessary to determine the boundary conditions for the application. The following conditions were available from the engine manuals for a spool speed of 8400 rpm:

• Total inlet pressure	573 000 Pa
• Total inlet mass flow rate	71.65 kg/s
• Static inlet temperature profile	(See figure 5.7)
• Coolant mass flow rate	2.7% of total mass flow
• Coolant temperature	534 K
• Total coolant pressure	614 000 Pa

Table 5.1 – NGV operating specifications

The following boundary conditions thus had to be computed:

- Static inlet pressure
- Static outlet pressure variation

The CFD model was set-up with the appropriate boundary specifications. Figure 5.6 shows the boundary types that were used. An initial calculation showed the Mach number to be in the region of 0.7, thus fluid was modelled as compressible. Conduction was solved within the blade solid as well as the impingement insert.

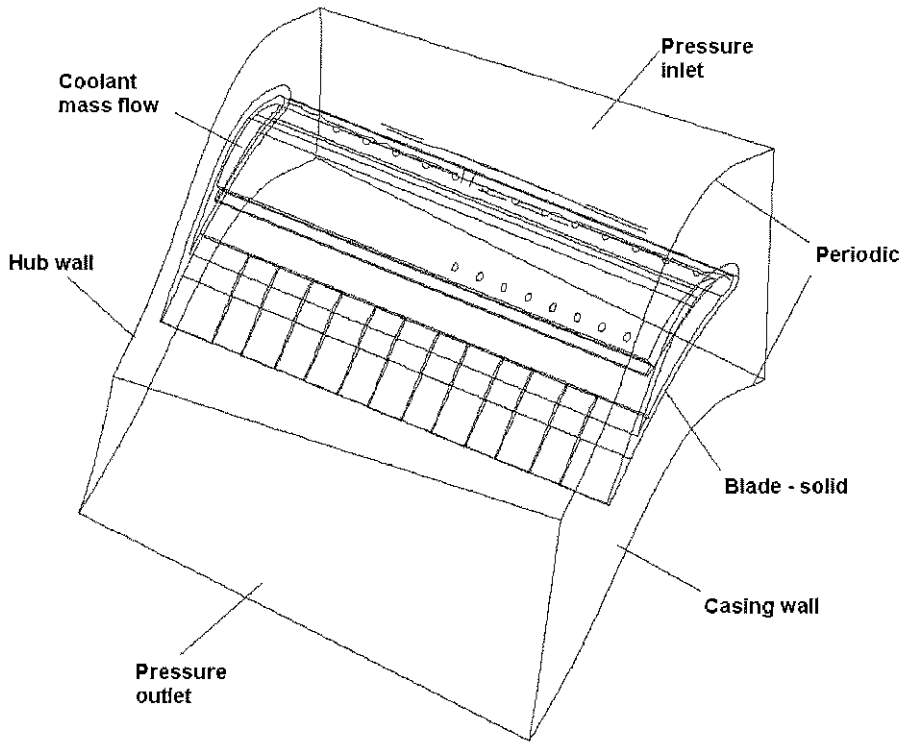

Figure 5.6 – general outline of NGV showing boundary types

The computational domain consisted of two main zones. The fluid zone was air and the solid zone was the blade. The blade is fabricated out of a material known as Haynes – 188. All physical properties of air [32] and Haynes – 188 [45] were modelled as temperature dependent. The temperature variance of the physical properties for Haynes – 188 is available in Appendix A.

A fourth order polynomial was fit through the temperature profile for input into the CFD code through the use of a user-defined function. Figure 5.7 shows the inlet temperature profile to the high-pressure turbine of the engine. The graph shows the variation of temperature with radial position, i.e. from hub to casing. Figure 5.8 shows the temperature contours at the inlet to the nozzle guide vane. The temperature contours follow the polynomial fit that was implemented into the CFD code. The maximum temperature occurs at 70% radial position, consistent with conventional design of many combustors. Thus it can be seen that the impingement insert has extra film cooling holes

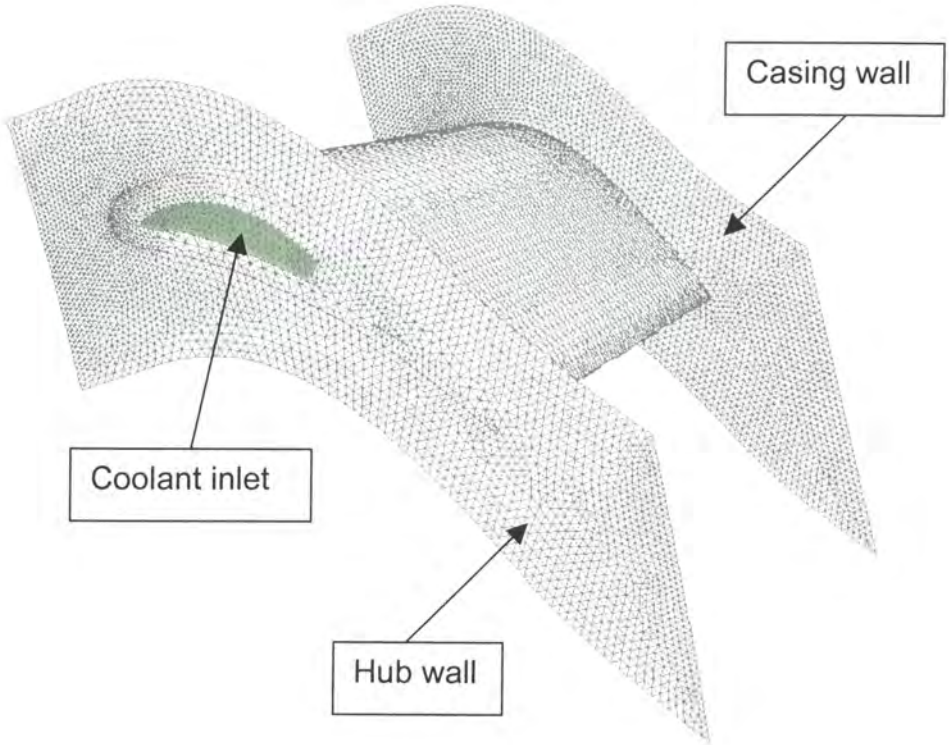

Figure 5.2 – Computational grid on blade

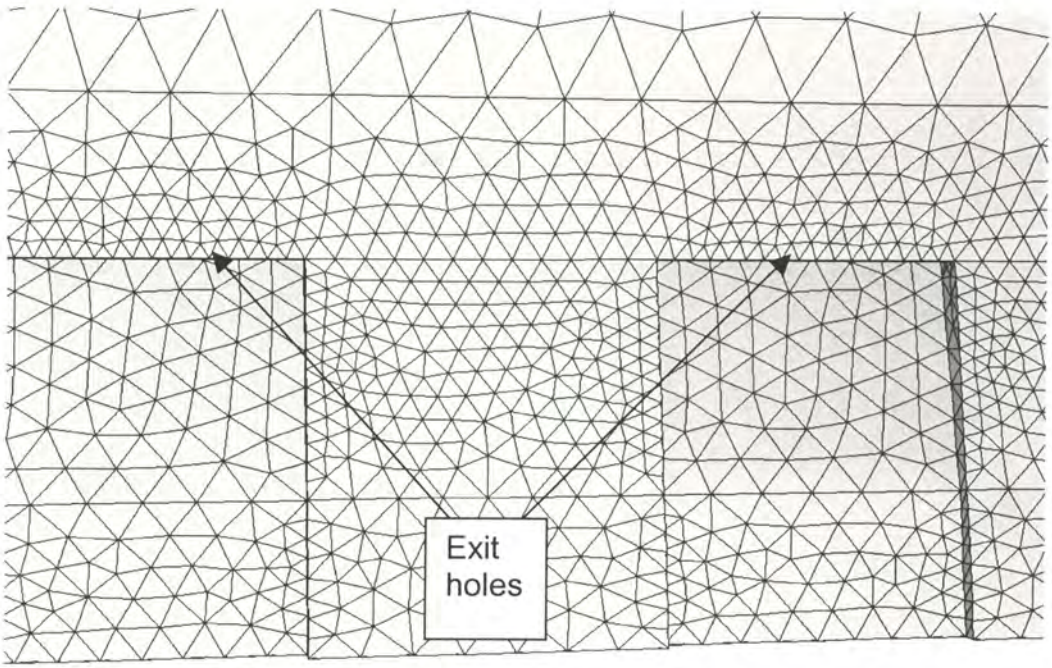

Figure 5.3 – computational grid on blade pressure side, close-up view of trailing edge

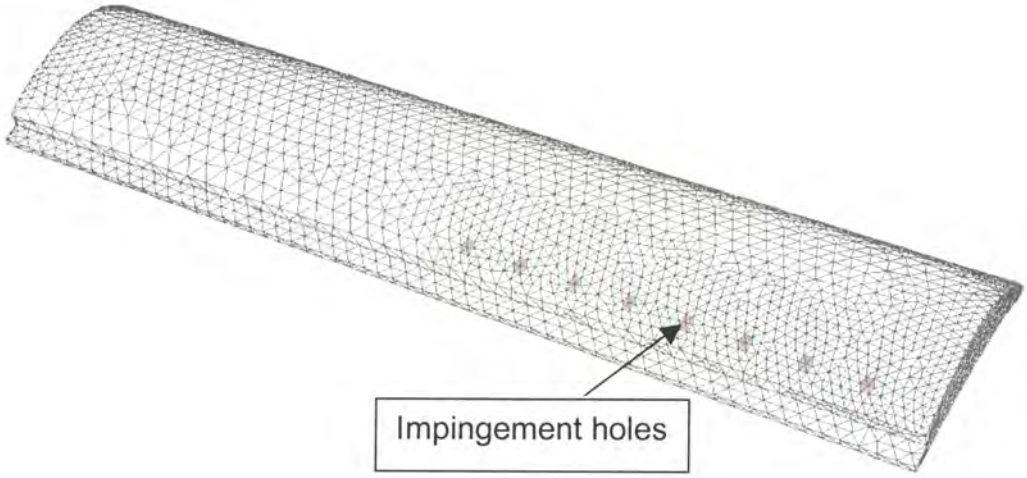

Figure 5.4 – computational grid on impingement insert, top view

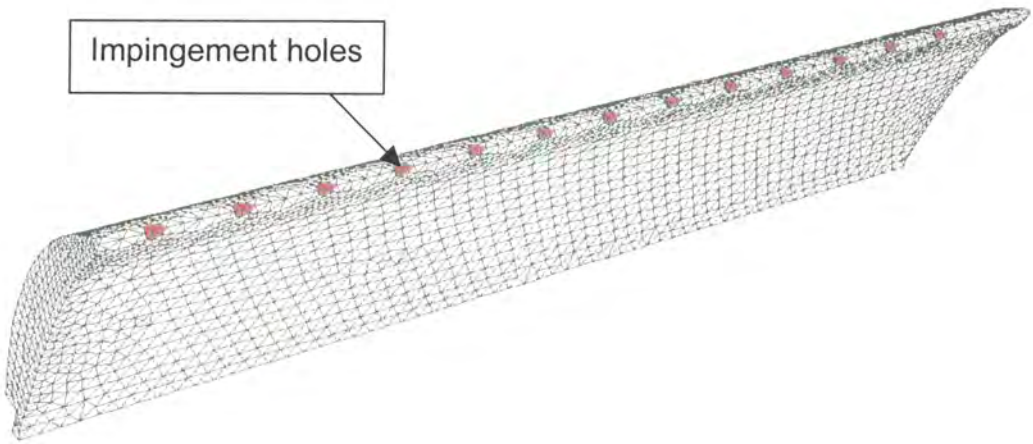

Figure 5.5 – computational grid on impingement insert, showing leading edge cooling holes

towards the casing side of the blade, to counter the effect of the large temperature magnitude present at this point.

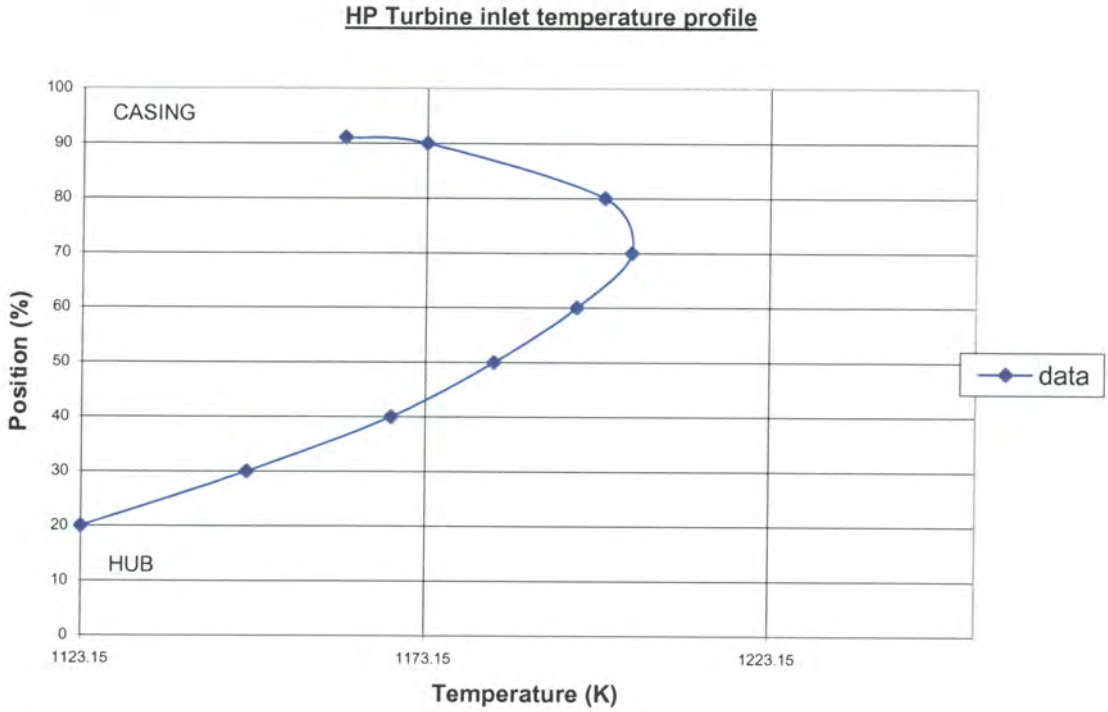

Figure 5.7 – inlet temperature profile for high-pressure turbine of engine

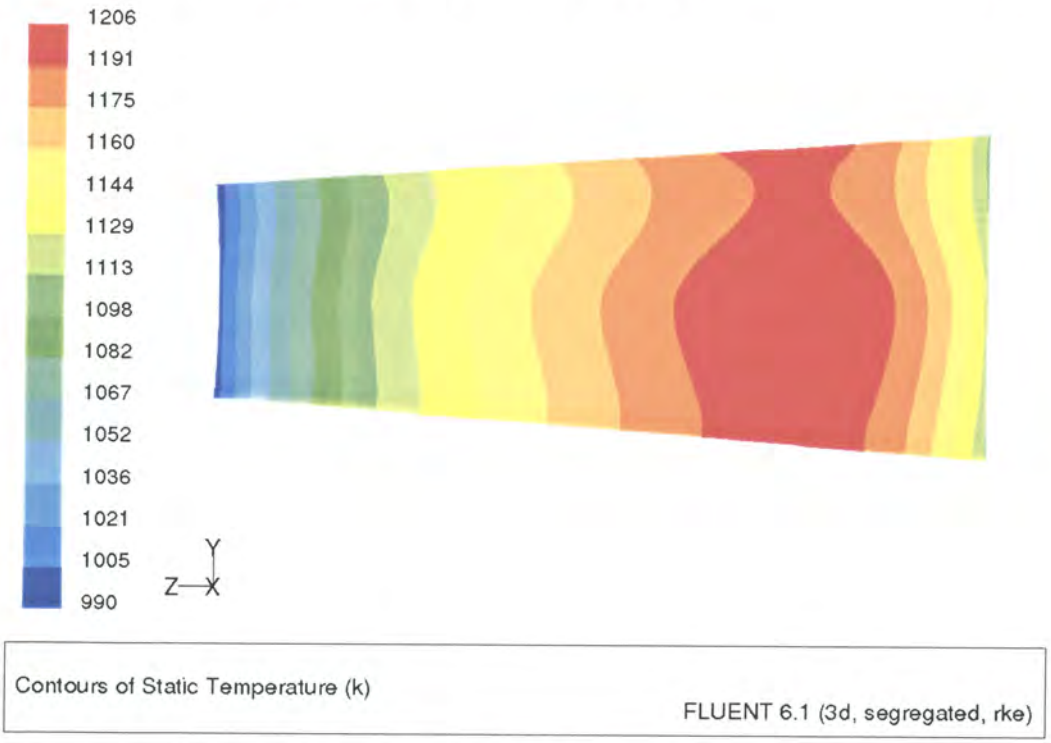

Figure 5.8 – variation of inlet temperature profile from hub to casing

The casing and hub end wall thickness was not physically modelled. Instead a wall thickness of 0.003m and a heat transfer coefficient of 100 W/m^2K were applied at the walls [46]. The wall thickness was used to calculate the conduction through the walls. This would give a temperature distribution on the hub and casing walls.

5.5.1 Calculation of static inlet pressure

The first step in this calculation was to obtain the inlet area and the throat area. The throat area is the area in the nozzle guide vane passage that has the smallest cross-section. These areas were obtained from the necessary detailed drawings that were available.

The following assumptions were made:

- *Isentropic behaviour at the inlet*
- *Calculation is at the mean radius of the blade*
- *Total temperature and total pressure do not change with position through the nozzle passage*

With these assumptions, the static pressure was determined to be **P=543039Pa**. Details may be found in Appendix D.

5.5.2 Determination of outlet static pressure variation

Due to the difference in friction losses over the different parts of the blade, it cannot be assumed that the static pressure is constant at the outlet of a blade passage. Hence, it is necessary to determine this for use as an input boundary condition into the CFD analysis. The same assumptions are valid as in the previous calculation, as well as the assumption of radial equilibrium. Radial equilibrium theory assumes that radial movements of air occur only on the passage through the blades and not in the spaces between blade rows. Experimental investigations have shown that this assumption is not strictly true [27]. However, in section 5.5.3, an estimation of flow losses as a result of friction is presented. The desired outcome of this analysis is to obtain an

equation for the outlet static pressure as a function of radius. Therefore, as the radius varies from hub to casing, so would the pressure. Using equations (4.1) and (D.1), the throat Mach number and static temperature is determined. Thus **M=0.705** and **P= 416 902 Pa**. After following the procedure outlined in Appendix D, the static outlet pressure variation is obtained as:

$$P = Kr^{0.4625} \tag{5.1}$$

Equation (5.1) can now be used as a boundary condition for the problem. The equation describes the variation of static pressure from hub to casing at the outlet of the nozzle guide vane. The constant *K* needs to be adjusted so that friction losses are taken into account.

5.5.3 Estimation of flow losses

An analytical method was used to estimate the flow losses in the nozzle guide vane [27]. Being an iterative process, it required an initial guess for the loss coefficient. Calculations are then carried out through which a *new* loss coefficient is determined. If the initial guess and the calculated value are the same or close, then the solution is acceptable and the iteration can be assumed to have converged. It was found that the initial guess of λ = 0.05 was satisfactory. Details may be found in Appendix D.

In the CFD model, the losses were accounted for by adjusting the outlet static pressure variation to get the correct inlet mass flow. This was because it was known from the engine manuals what the mass flow rate was. However applying equation (5.1) with a *K*=729416, as a boundary condition resulted in a mass flow rate different from the actual case. Therefore it was necessary to adjust the constant, *K*, to get a correct mass flow. Hence, this was an iterative process and the final value obtained was *K*=100000. The mass flow rate obtained using this value for *K* was 1.606 kg/s compared to 1.643 kg/s obtained from the engine manual. Therefore this gives an acceptably low error

of 2.3%. The outlet static pressure variation was also implemented in the CFD code through the use of a user-defined function available in Appendix B.

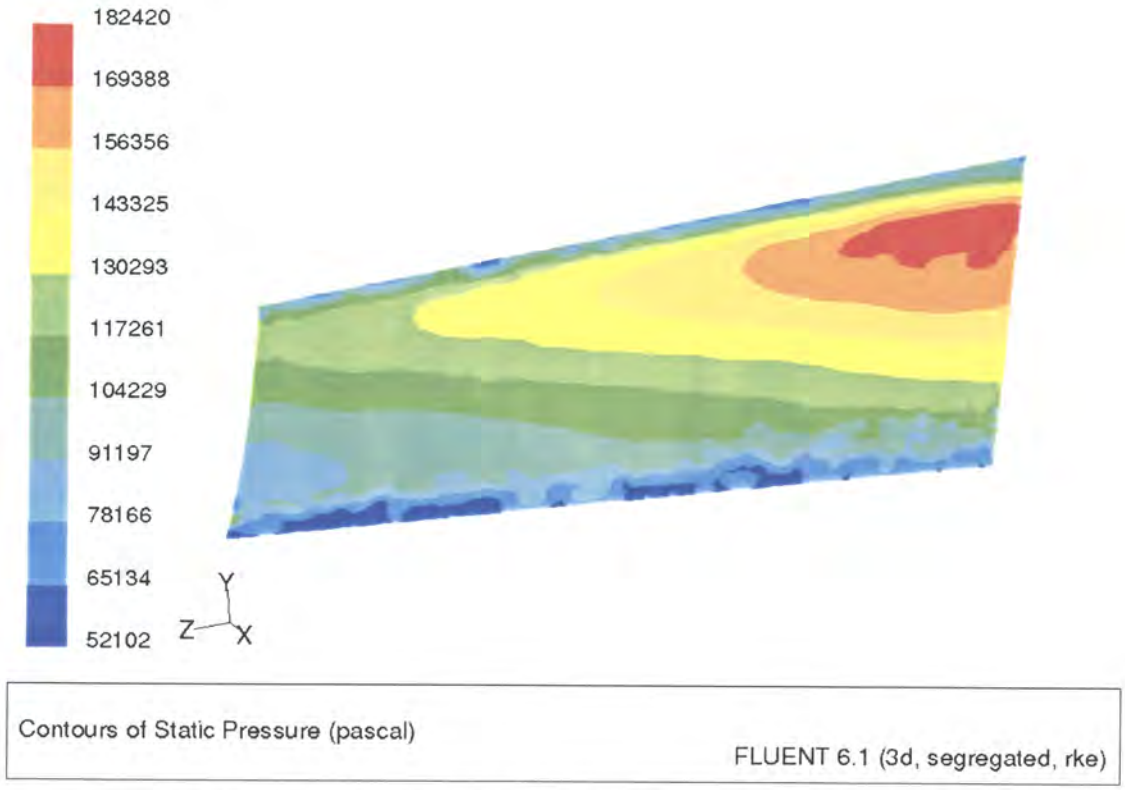

Figure 5.9 - variation of outlet static temperature from hub to casing

Figure 5.9 shows the contour variation of the outlet static pressure variation as implemented in the CFD code.

5.6 Thermal Results

For this application, no experimental data was available and thus CFD results were compared to results for the same blade using a different approach [46] - [47]. Pressure distribution results were available from [46] at five different span wise sections of the blade. Thus similarly, pressure distributions over the blade pressure and suction sides were obtained at the five different locations. Figure 5.10 shows the location of the five sections on the blade where pressure distributions were obtained. Static pressure data for each section was obtained from the numerical solution and compared to the results

obtained from a different study [46]. These results were obtained from *Loss 3D*, an Euler code. Figures 5.11 – 5.15 show the pressure distributions on the pressure and suction sides of the blade at each different section.

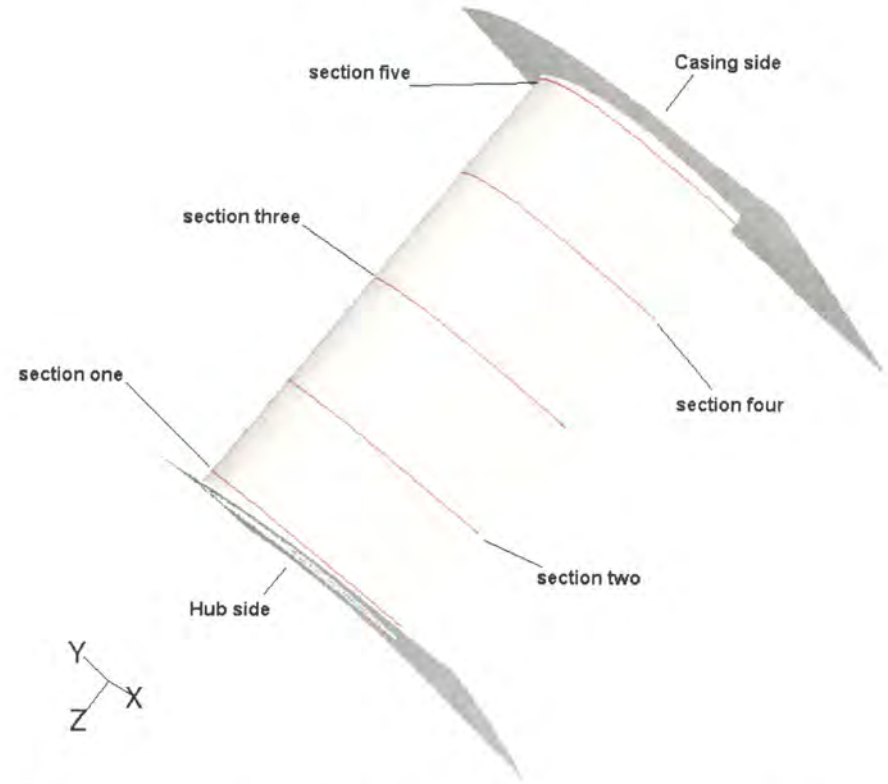

Figure 5.10 – location of span wise sections on blade surface

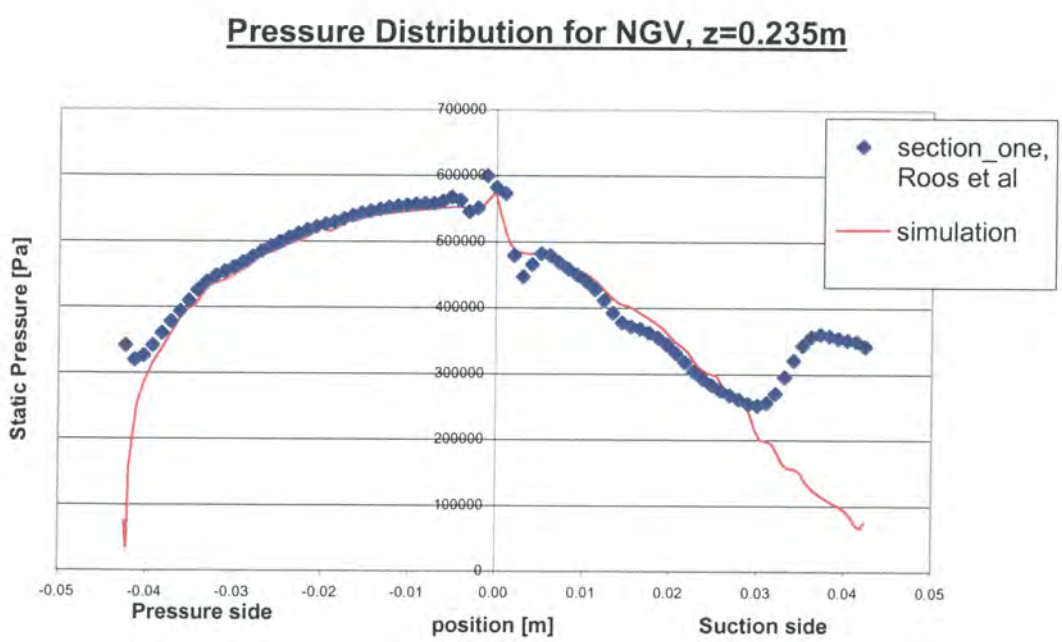

Figure 5.11 – static pressure distribution at section one

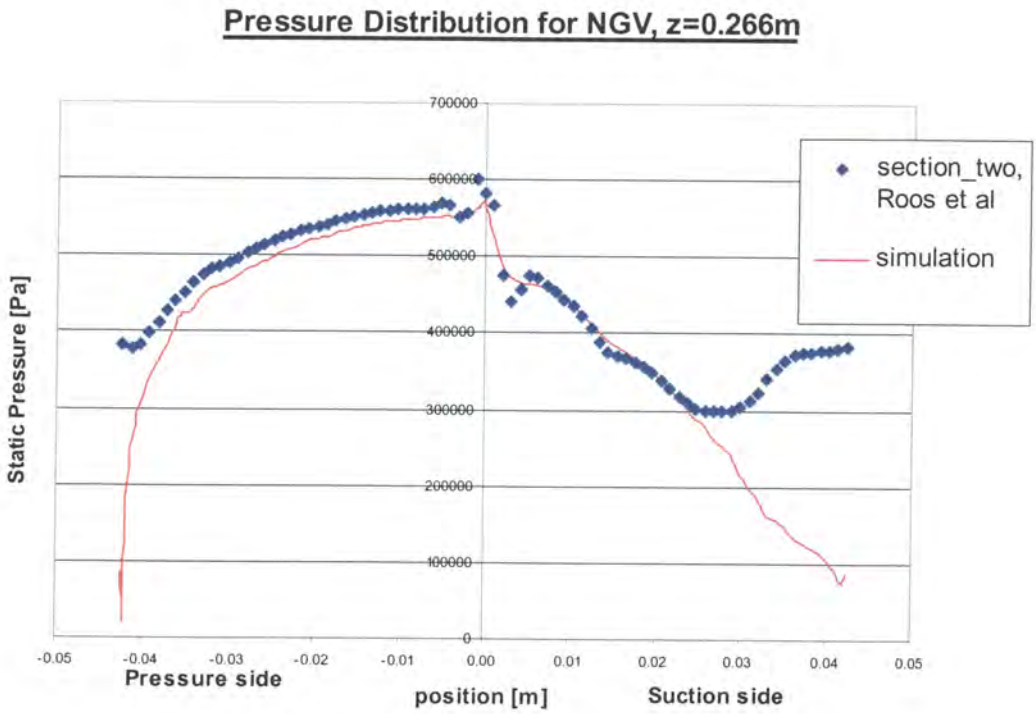

Figure 5.12 – static pressure distribution at section two

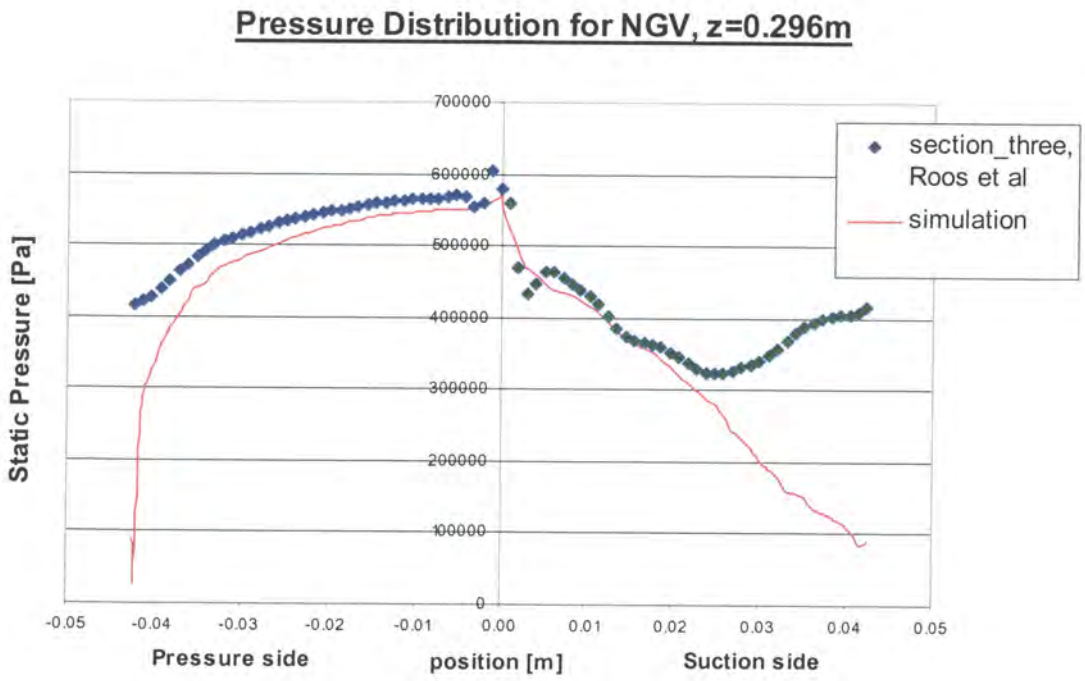

Figure 5.13 – static pressure distribution at section three

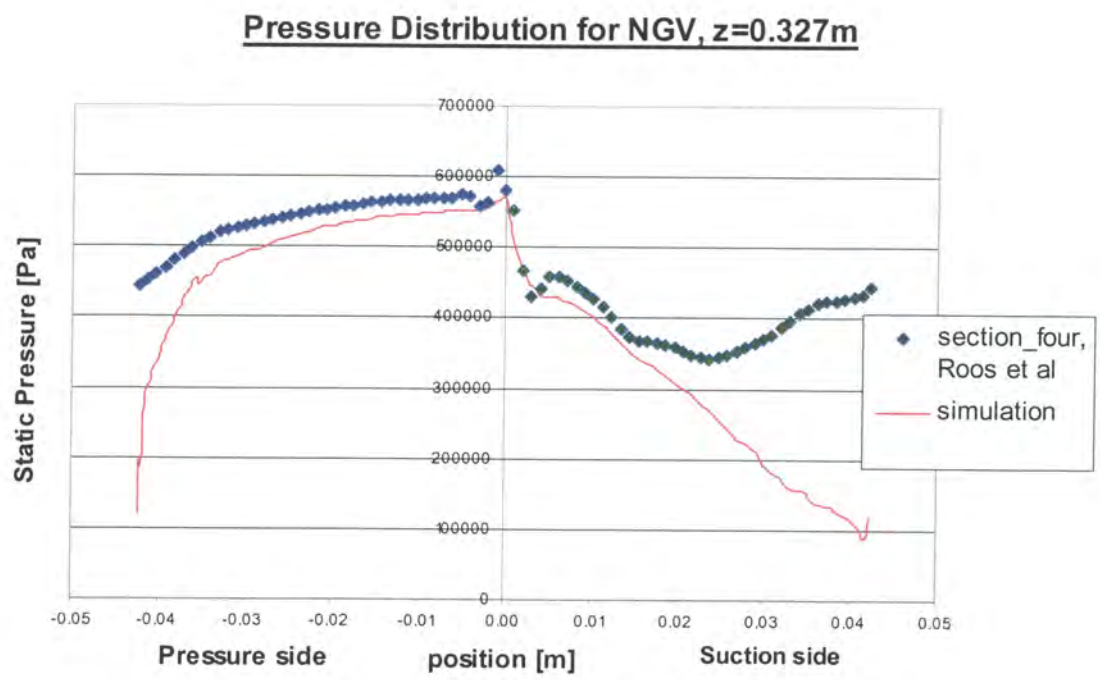

Figure 5.14 – static pressure distribution at section four

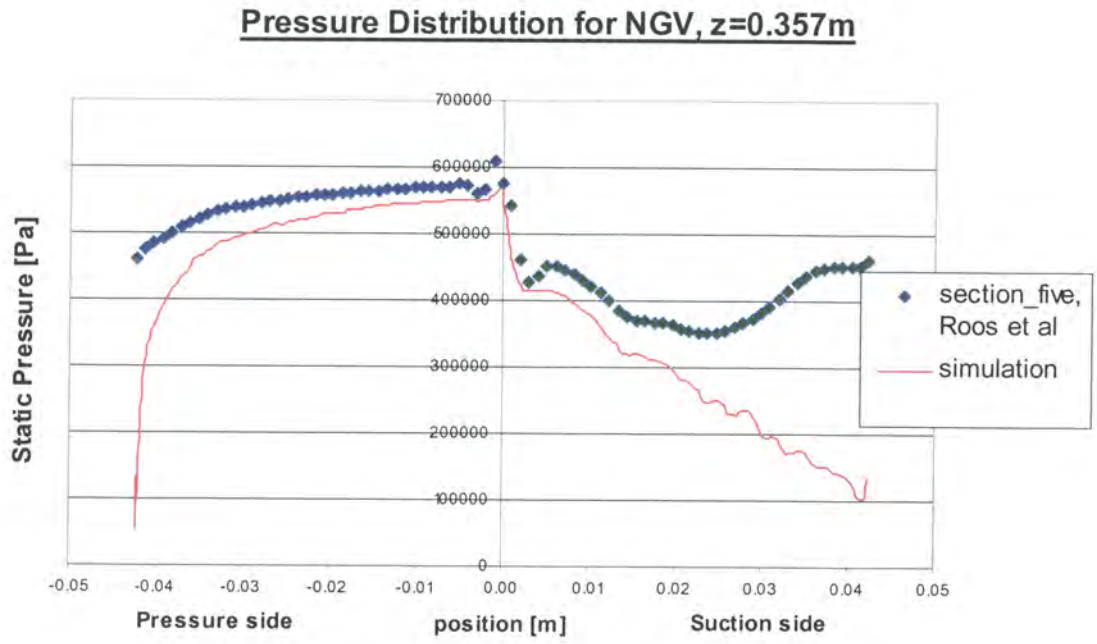

Figure 5.15 – static pressure distribution at section five

In general pressure distribution predicted using CFD compared well to the existing data on the pressure side of the blade. On the suction side of the blade there is clearly pressure recovery predicted by the Euler code that does not occur in the CFD simulation. On both sides, the pressure distribution comparisons deteriorate as one approaches the casing side. The reasons for the differences can be summarised as follows:

- The CFD simulation does not predict the pressure recovery on the suction side of the blade predicted by the Euler code. When analysed critically, there is no reason for pressure recovery of the flow in that particular area. The curvature of the blade is relatively low and the location is quite far downstream of the suction side of the blade. There is, however, one important aspect that has been ignored in the CFD analysis. This is the effect of the first stage rotor blades on the flow over the NGV. The rotating blade has an effect on the pressure distribution on the suction side of the nozzle guide vane.
- Another important issue is that the CFD results are actually pressure driven. Therefore, slight deviations in the static pressure outlet variation from the *real* condition will cause the disparities. The accuracy reduces towards the casing side of the blade. However according to the study conducted through the use of the Euler code, the actual flow conditions are transition driven [46]. This flow phenomenon is not captured through the CFD model primarily due to the turbulence model.
- The low pressures obtained towards the trailing edges at all the sections of the blade are due to the inaccuracies in the approximation of the outlet static pressure variation that was applied as a boundary condition. The main reason arises from the assumption of radial equilibrium, which was necessary in order to continue with the analysis but is not strictly applicable in a real engine.

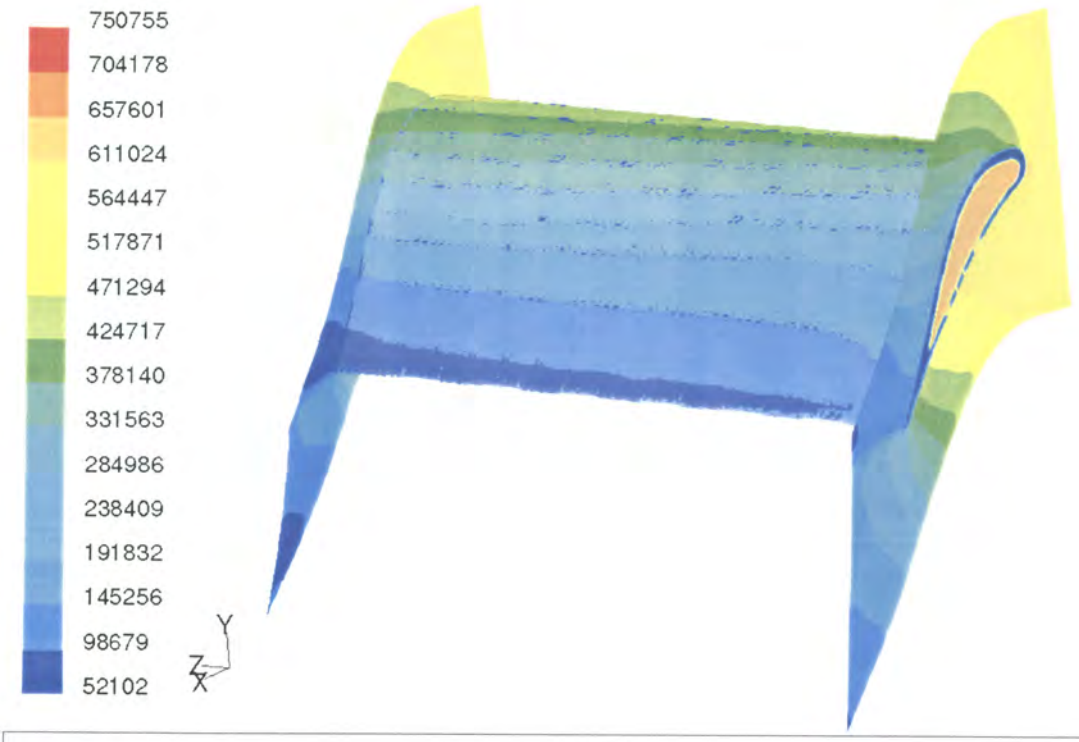

Figure 5.16 – contours of static pressure

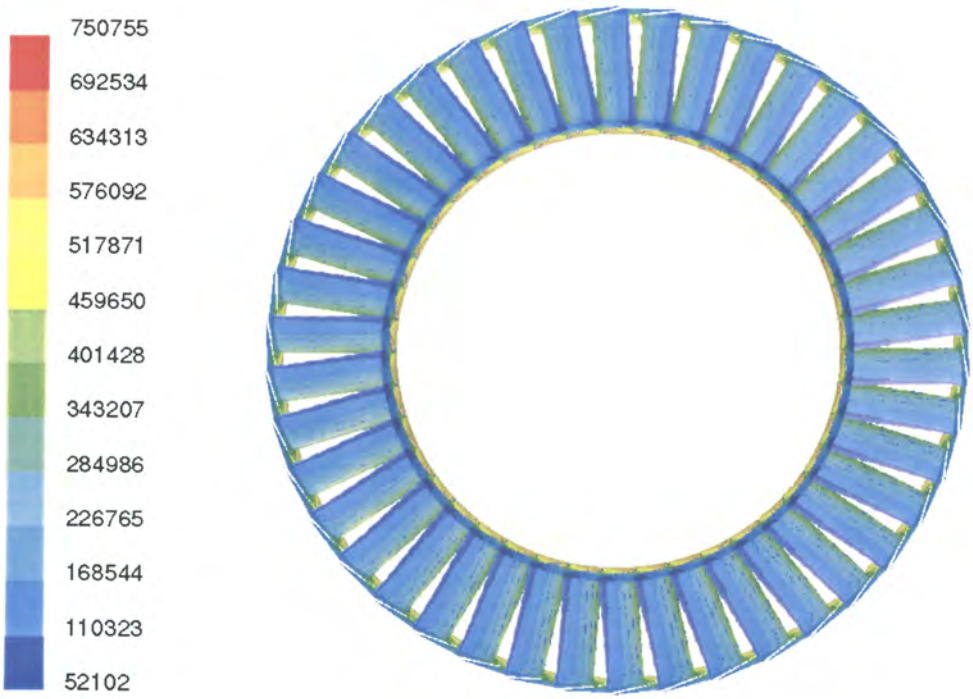

Figure 5.17 – static pressure distribution on nozzle guide vanes

Figures 5.16 and 5.17 show contour plots of the static pressure distribution over the blade surface.

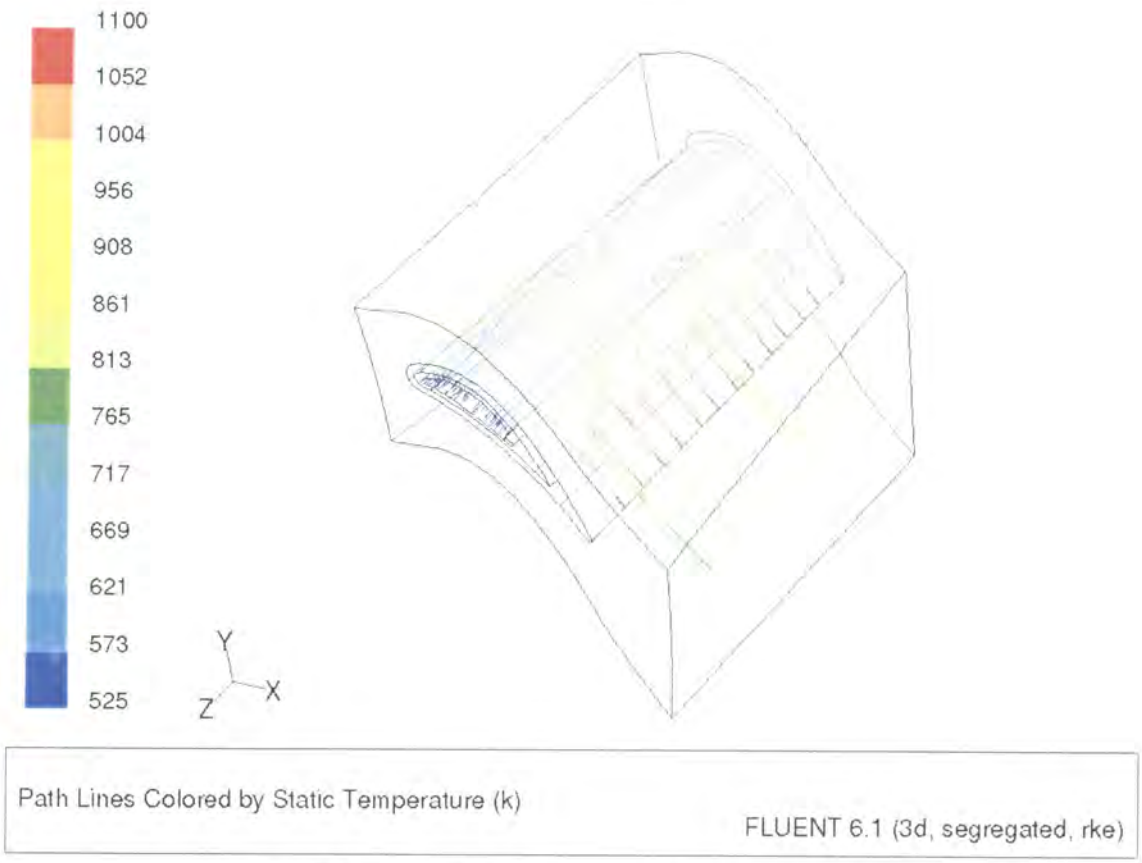

Figure 5.18 – path lines coloured by temperature

Figure 5.18 shows path lines coloured by temperature magnitude from the coolant inlet to the six trailing edge slots on the blade. It shows how the coolant flow travels through the internal section of the blade. It is introduced at the hub side of the blade. It then flows out through the leading edge holes, impinging on the leading edge inner surface of the blade as well as through the trailing edge suction side holes. These holes help control the high surface temperatures expected at 70% radial position as a result of the combustor exit profile. The flow that exits from the leading edge holes travels around the impingement insert, where it joins the flow that exited from the trailing edge suction side holes. This flow pattern helps cool the blade middle sections on both the pressure and suction sides. The combined flow at the back of the

impingement insert then exits via the six cooling slots located at the trailing edge of the blade. This then mixes with the hot combustion gas.

Surface temperatures were unavailable at similar locations for comparison purposes. However, a different study [47] computed the temperature distribution on the blade surface by solving only for conduction, using the adiabatic wall temperatures and heat transfer coefficients obtained from [46]. The conduction solver has transient capabilities but for purposes of comparison to this study, the temperature distribution was obtained at the same spool speed of 8400 rpm.

Figures 5.19 and 5.20 show a comparison of the temperature distribution between the CFD solution used in this study to the conduction solver used in [47]. In general the range of maximum and minimum values compare well. The maximum temperature predicted in this study is 1212 K compared to 1234 K in the other study. Two distinct differences are the hot spot predicted by the previous study on the centre of the suction side compared to the cooler temperatures predicted using the CFD model. This is the area where the cooling fluid impinges onto the surface and one can conclude that the CFD model calculates the impingement flow on the inside more accurately than was possible in the previous simulations.

This is also shown by Figures 5.21 and 5.22 that show the blade but for different temperature ranges when compared to the previous figures. The second is the hot sections towards the trailing edge of the blade where the CFD also predicts lower temperatures. This can be linked directly to the pressure recovery predicted by the one method [46], but not predicted by the CFD simulation. This phenomenon increases the heat transfer rate and therefore the surface temperature in Figure 5.20 compared to Figure 5.19.

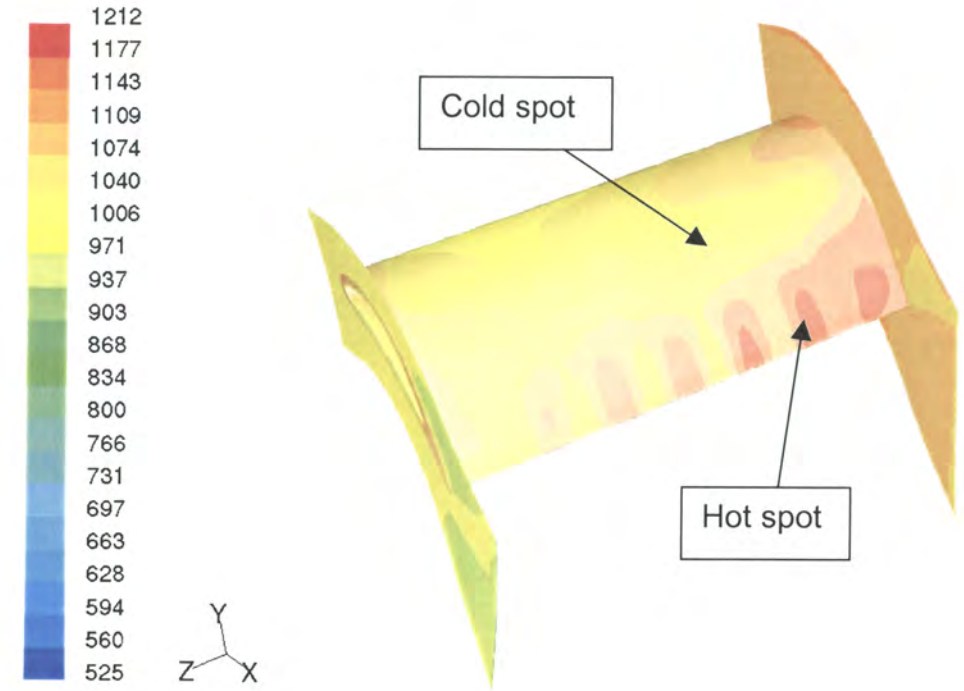

Figure 5.19 – Temperature distribution on suction side of blade, CFD

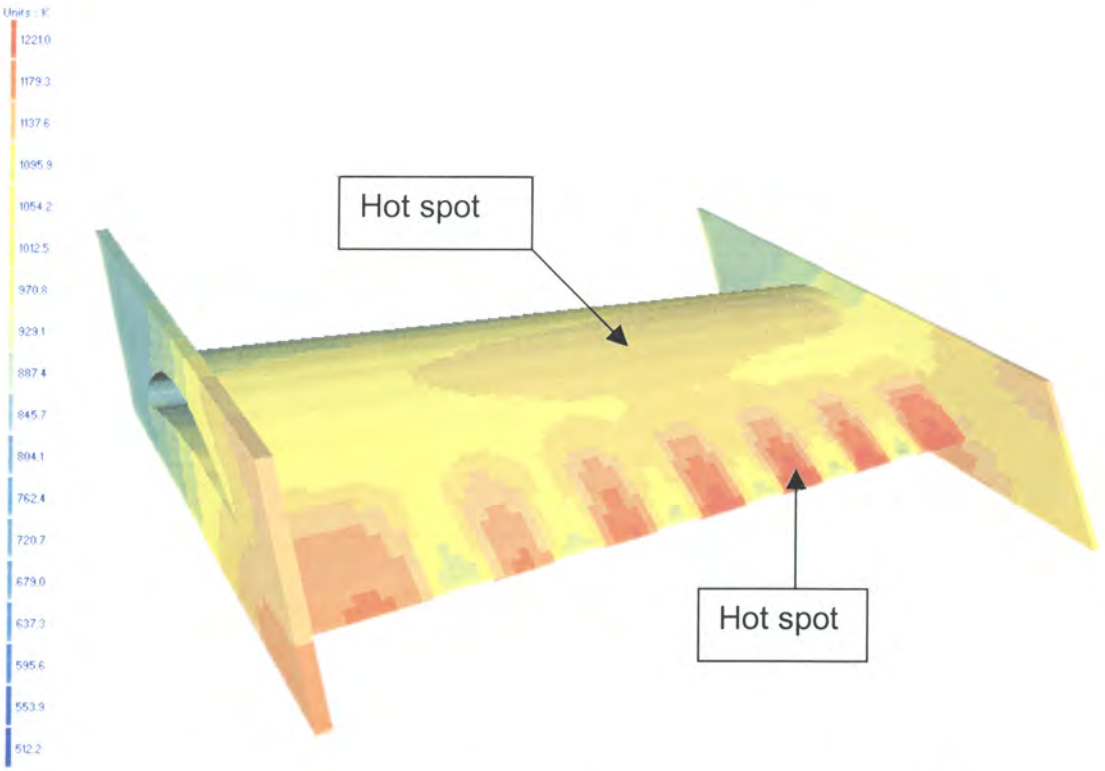

Figure 5.20 – Temperature distribution on suction side of blade [47], conduction solver

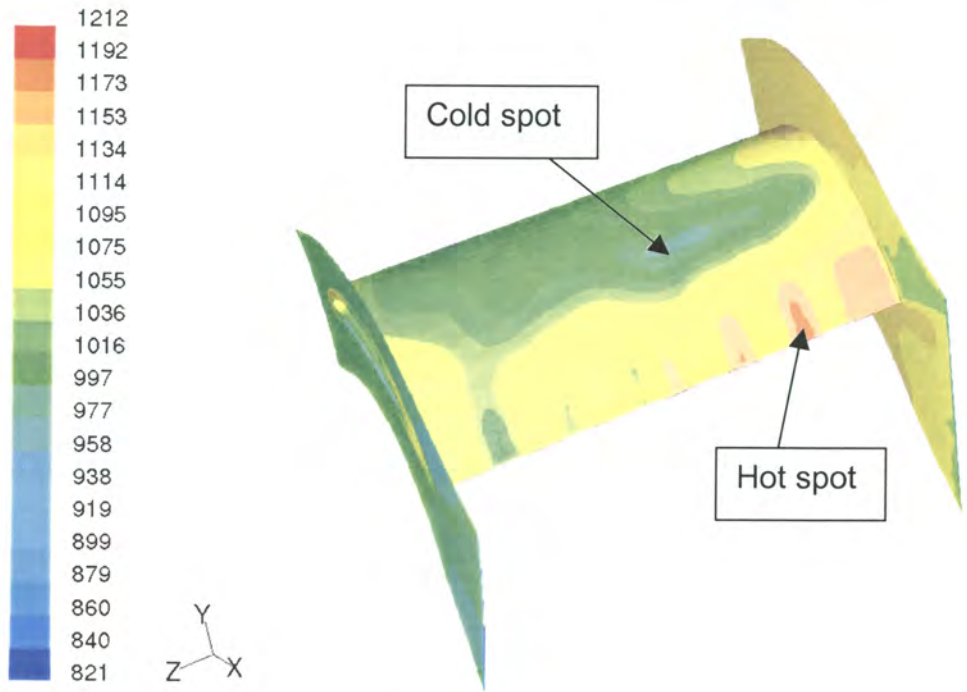

Figure 5.21 – Temperature distribution on suction side of blade, CFD

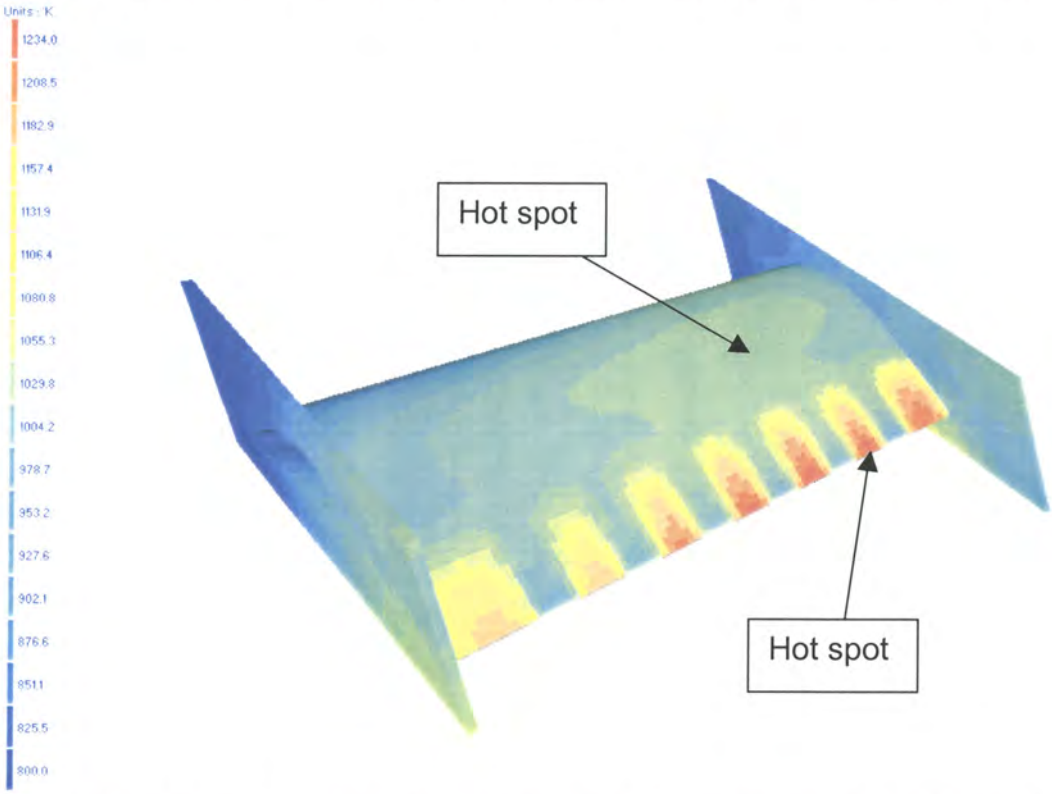

Figure 5.22 – Temperature distribution on suction side of blade [47], conduction solver

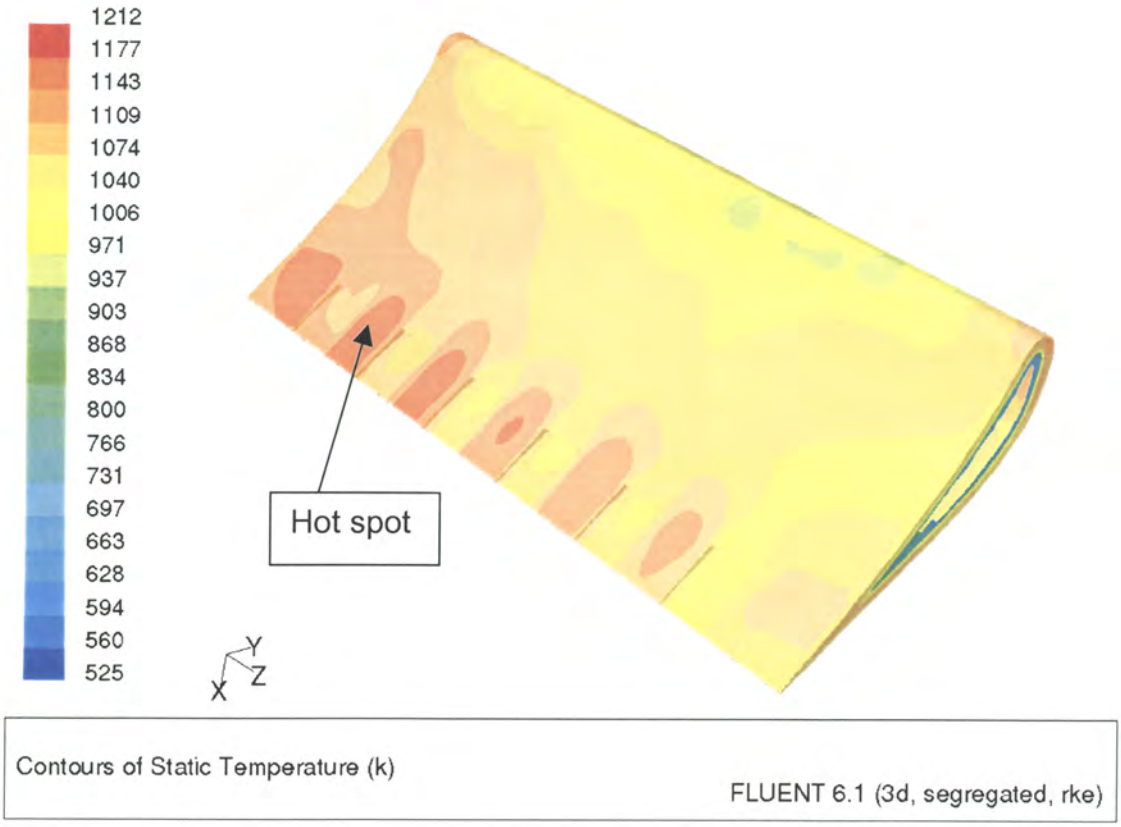

Figure 5.23 – Temperature distribution on pressure side of blade, CFD

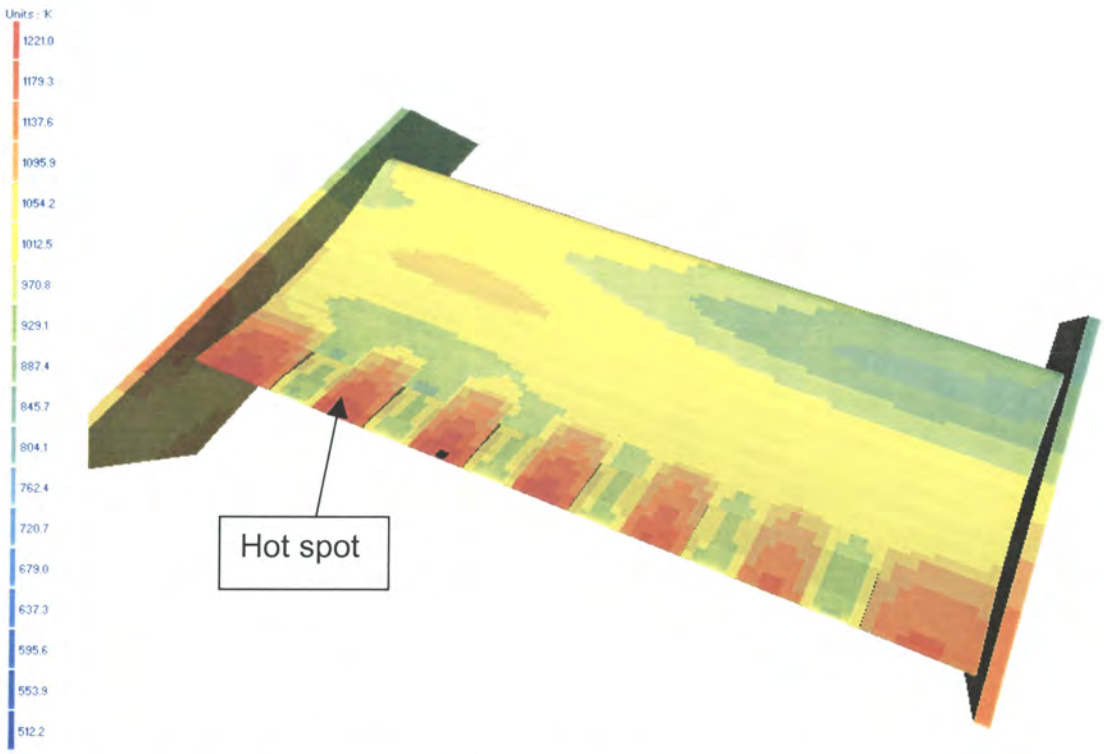

Figure 5.24 – Temperature distribution on pressure side of blade [47], conduction solver

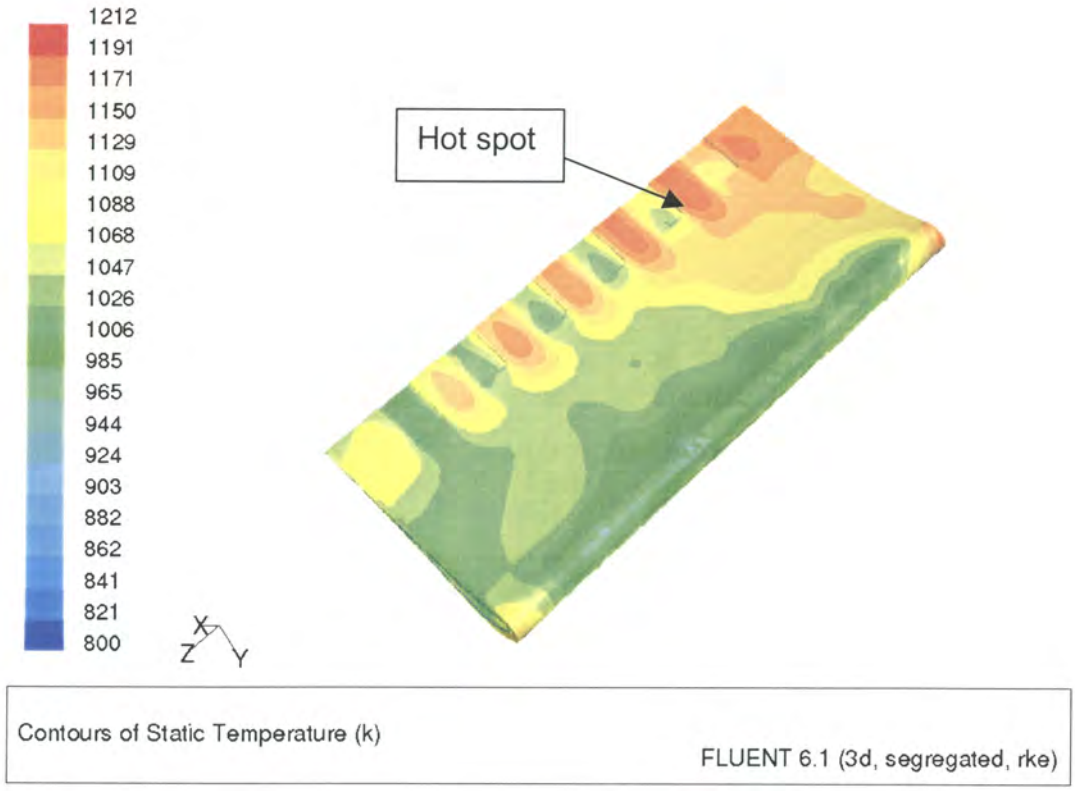

Figure 5.25 – Temperature distribution on pressure side of blade, CFD

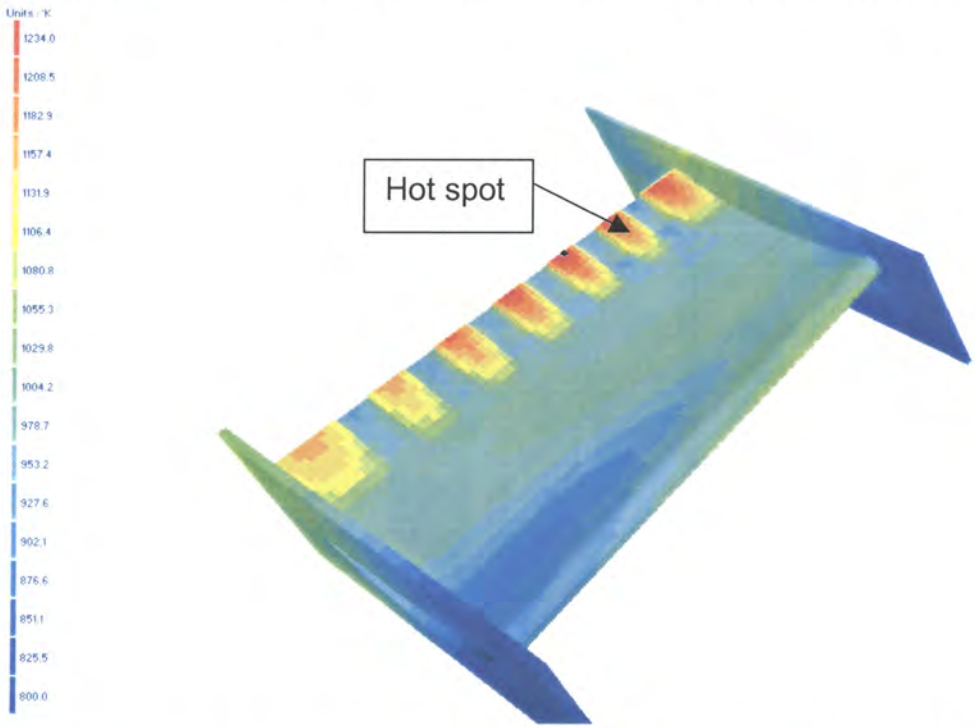

Figure 5.26 – Temperature distribution on pressure side of blade [47], conduction solver

Figures 5.23 and 5.24 compare the temperature distribution on the pressure side of the blade for a global temperature range, whereas figures 5.25 and

5.26 show a local temperature range. The general trend of predicting the hot spots is good as they lie in the same geometrical area. The hot spot is occurring towards the casing side where the peak of the inlet temperature profile occurs. The peak temperatures compare favourably, being in the same order as on the suction side of the blade.

The pressure side results for the temperature compare well due to the fact that both the CFD results and those calculated in [46] for pressure distributions compare well. The flow is captured accurately and no such phenomena as transition or flow separation occur on the pressure side. Therefore, the temperatures are similar and undisturbed by transition or separation. The pressure side of the blade also has no direct impingement of coolant air on it, as was the case for the suction side. Thus local 'cold spots' are not seen to form due to impingement.

Figures 5.27 - 5.30 show different views of the temperature distributions on the nozzles guide vanes.

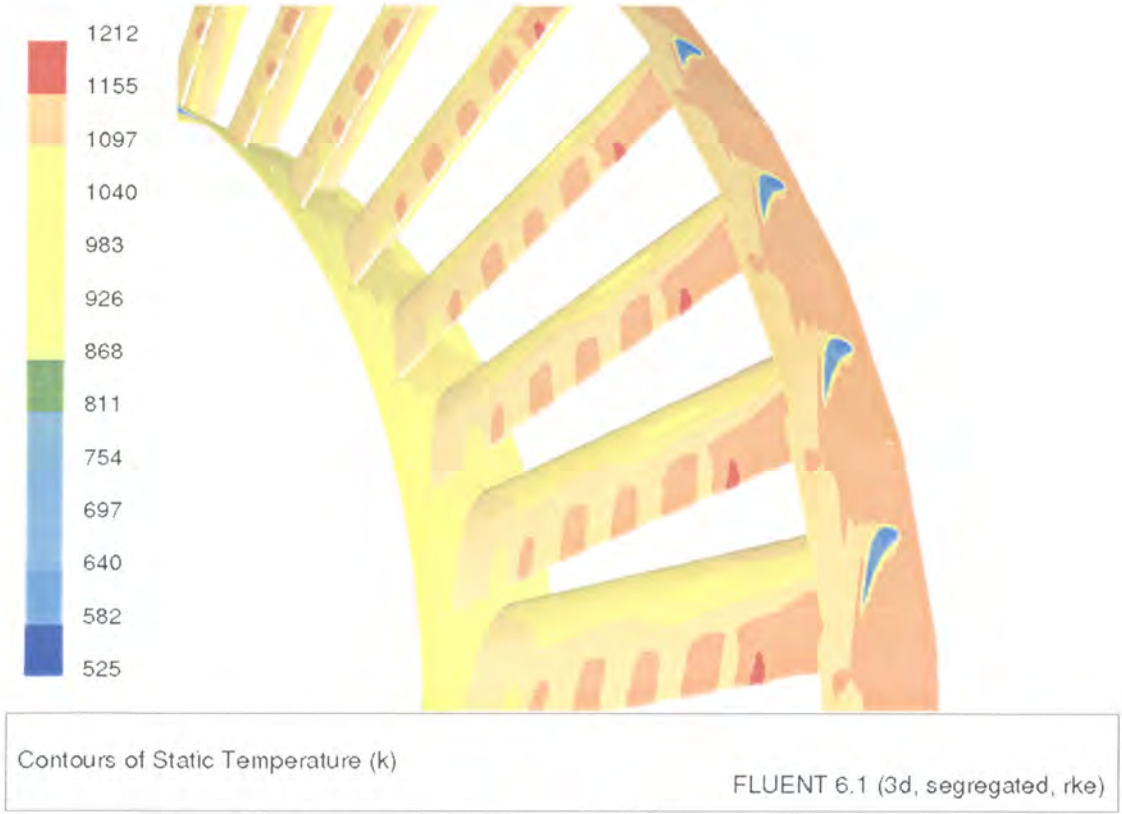

Figure 5.27 – Blade temperature distribution showing casing wall

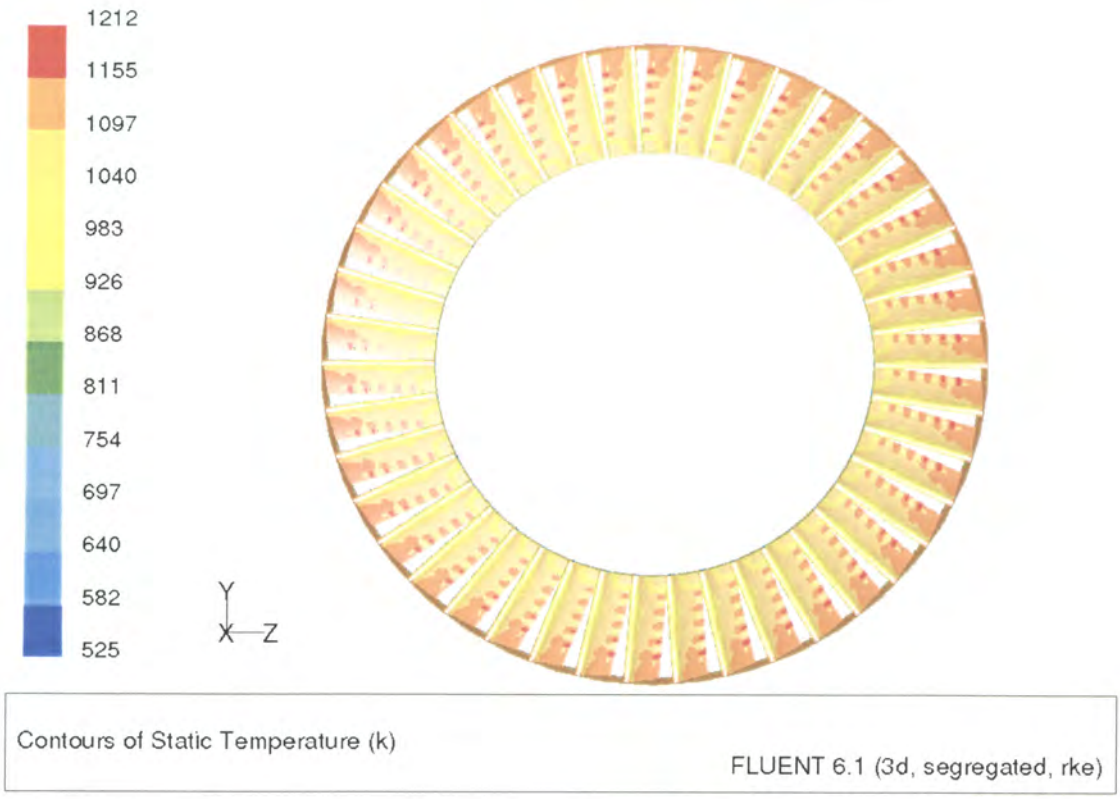

Figure 5.28 – temperature distribution of the nozzle guide vanes, suction side

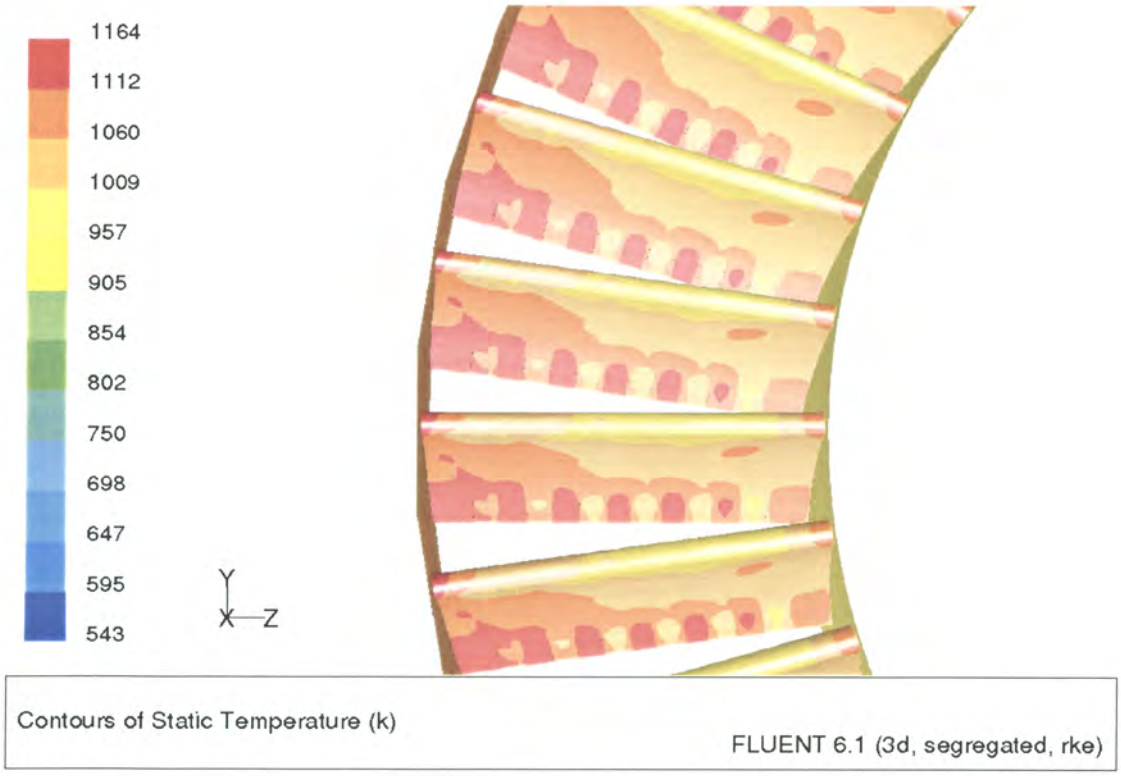

Figure 5.29 – temperature distribution of the nozzle guide vanes, suction side, close-up view

Chapter Six

Conclusions and Recommendations

This chapter gives an overview of the work done in the entire study. It summarises the main aspects of the study. It gives a conclusion and ends with recommendations for any future work that may be conducted in the field of heat transfer and thermal stresses on gas turbine nozzle guide vanes.

6.1 Summary

Due to a relative high thermal efficiency, the gas turbine engine has wide ranging applications in various industries today. The aerospace and power generation sectors are probably the best known. One method of increasing the thermal efficiency of a gas turbine engine is to increase the turbine inlet temperature. This increase in temperature will result in an additional thermal load being placed on the turbine blades and in particular the nozzle guide vanes. The higher temperature gradients will increase the thermal stresses. In order to prevent failure of blades due to thermal stresses, it is important to accurately determine the magnitude of the stresses during the design phase of an engine.

This study comprised of three different smaller studies to evaluate the accuracy of results obtained from using standard modelling techniques. The first dealt only with heat transfer. A simple one-equation turbulence model was used and thermal stresses were not analysed. The general heat transfer trend was captured although; the values differed from the experiment. The second study increased the complexity of the problem by including the thermal stress calculation and analysing a cooled nozzle guide vane. Results of two different turbulence models were also compared so as to ascertain which model gave the most accurate results in terms of both heat transfer trends and numerical values. The same methodology is then applied to a three-dimensional application in which the heat transfer was solved for a nozzle guide vane of a commercial gas turbine engine.

The accuracy of results varied with the choice of turbulence model but was, generally within ten percent of experimental data. It was shown that the accurate determination of the heat transfer to the blade is the key element to accurately determine the thermal stresses. Important conclusions are drawn from this research in the subsequent section and recommendations for further work are also given.

6.2 Conclusions

The conclusions and contributions reached during the course of this research study are as follows:

- CFD can be used as an analysis tool to predict and improve the understanding of flow phenomena in a cooled gas turbine nozzle guide vane. The analyses showed that it is important to validate the results against experimental data to obtain an estimate of the expected degree of accuracy. CFD results when using standard turbulence models are at most accurate within ten percent.

- The *Spalart-Allmaras* turbulence model proved to be robust and computationally efficient. It was used in both the heat transfer analyses for the blades with and without cooling. In both cases it predicted the heat transfer distribution trends, although the numerical values differed from the experimental data.

- The *realizable* k-ε turbulence model, used to analyse the two and three-dimensional cooled nozzle guide vanes, produced errors of up to ten percent in heat transfer. However, the accuracy was vastly better in predicting pressure distributions, where the error was as low as three percent in some cases. This model required a fine mesh when used together with the enhanced wall treatment. This implies special attention must be given to the mesh requirements when considering heat transfer. It is imperative that the correct y^+ range is adhered to.

- Accurate material property data is essential for modelling the temperature distributions within solids. It is important to determine whether material properties such as thermal conductivity, Modulus of Elasticity and coefficient of thermal expansion are temperature dependent or temperature independent. Also where experimental data is available for blade heat transfer distributions, it is important to match

the material properties used for the experiment to those of the numerical model.

- In most cases the numerical model was seen to generally over predict the temperature distributions on the blade surfaces. The pressure side results of the blade were always more accurate than the suction side results of the blade. The percentage errors were lower on the pressure side. This was mainly attributed to the nature of the flow, which sees adverse pressure gradients on the suction side that may lead to flow separation. Also shock waves form here, which can be difficult to predict the exact location due to the limitations of the turbulence models used.

- The thermal stress distribution is directly related to the temperature distribution. Hence inaccuracies in predicting temperature distribution are carried over when calculating the thermal stresses.

6.3 Recommendations for further work

The recommendations for further work applicable to the present study can be summarised as follows:

- Incorporate sensitivity studies to the thermal conditions, such as the effect of material properties to the accuracy of the solution.

- A better and more detailed mesh model can be investigated so as to capture the thermal gradient more accurately. Included in such an investigation can be the use of newer and better equipped turbulence models such as the k-ω turbulence model and the *V2F* turbulence model, that were unavailable at the time of this study.

- For the three-dimensional model, the study can be extended to include the effect of an entire turbine stage. This is because of the influence a rotor blade has on the pressure distribution of the guide vane, where

phenomenon such as flow separation may occur due to stator-rotor interaction.

- In order to accurately obtain thermal stress values, a complete blade model that includes all the geometric information of the hub and casing should be modelled so that the blade fixation can be accurately implemented.

- The study needs to be extended to include transient effects on blade. More input data would be needed for such a study. The thermal stresses for the transient cases also need to be analysed, since the worst-case scenario would be occurring here.

- An experimental investigation of heat transfer and thermal stresses that can be used as a validation for a part of this study should be done. In particular the nozzle guide vane used in the three-dimensional analysis should be placed in a cascade test and the various flow conditions be experimentally determined. Thermal strain measurements on the blade should be conducted and compared to the numerical results.

NOMENCLATURE

English Symbols

C	Gas velocity, Integration constant	[m/s], ----
$C_{'SUBSCRIPT'}$	Turbulence constants	----
D	Displacement	[m]
E	Young's Modulus	[Pa]
h	Heat transfer coefficient	[W/m^2K]
k	kinetic energy per unit mass, thermal conductivity, specific heat ratio	[J/kg], [W/mK]
L	length	[m]
Ma	Mach number	----
N	Rotational speed	[rpm]
o	Opening	----
q	Heat flux per unit area	[W/m^2]
P	Pressure	[Pa]
r	Radius	[m]
ref	reference	
s	Blade pitch	[m]
T	temperature	[K]
t	time	[s]
V	Velocity	[m/s]
u, v, w	velocity component	[m/s]
U	blade speed	[m/s]
u'	fluctuating velocity component	[m/s]
x, y, z	coordinate directions	
y^+	dimensionless wall distance	----

Greek Symbols

α	coefficient of thermal expansion, gas angle	[μm/mK]
δ	delta function	Units vary
Δ	change in variable	----
ε	Strain, turbulence dissipation rate	[m/m], [m^2/s^3]
κ	Von Karman constant	----
λ	Nozzle Loss coefficient	----
μ	dynamic viscosity	[kg/ms]
θ	Tangential component	----
ρ	density	[kg/m^3]
σ	stress, turbulent Prandtl number	[Pa], ----
υ	Poisson's ratio	----

Subscripts

1	Inlet
2	Outlet
0	Initial, Stagnation property
a	Axial
c	Casing, critical
f	Fluid side
h	Hub
L	Local
m	Mean
N	Nozzle guide vane
o	Total conditions
i, j, l	x, y, z coordinates
p	Point, position adjacent to wall
rad	Radiation
s	surface
t	turbulent
VM	von Mises
w	Whirl or tangential component

∞	Ambient

REFERENCES

[1] Mallet, O., Kaguchi, H., Ilschner, B., Meyer-Olbersleben, F., Nikbin, K., Rezai-Aria, F., Webster, G.A., *Influence of thermal boundary conditions on stress-strain distribution generated in blade-shaped samples*, International Journal of Fatigue, Vol. 17, no. 2, 1995.

[2] Simbirskii, D.F., Bogdanov, V.G., Tret'yachenko, G.N., Kuriat, R.I., Voloshchenko, A.P., *Experimental and Theoretical Determination of Thermal Stress and Heat Transfer for a Turbine Blade, Using High-Temperature Thin Film Thermocouples*, Translated from Problemy Prochnosti, No. 7., pp 42-47, July 1974.

[3] Bohn, D., Lang, G., Schonenborn, H., Bonhoff, B., *Determination of Thermal Stress and Strain Based on a Combined Aerodynamic and Thermal Analysis for a Turbine Nozzle Guide Vane*, ASME Cogen-Turbo Power Conference, 95-CTP-89, 1995.

[4] Mukherjee, D.K., *Stresses in Turbine Blades Due to Temperature and Load Variation*, ASME Paper no. 78 – GT – 158.

[5] Maya, T., Katsumata, I., Itoh, M., *A Study of Thermal Fatigue Life Prediction of Air-Cooled Turbine Blades*, ASME Paper no. 78-GT-63.

[6] Sato, T., Takeishi, K., Sakon, T., *Thermal Fatigue Life Prediction of Air-Cooled Gas Turbine Vanes*, Journal of Engineering for Gas Turbines and Power, Vol. 108, April 1986.

[7] Wan, S.M., Lam, T.C.T., Allen, J.M., McCloskey, T.H., *A Gas Turbine Blade Thermal/Structural Program with Linked Flow-Solid Modeling Capability*, ASME Paper no. 94-GT-270.

[8] Thompson, R.L., Maffeo, R.L., *A Computer Analysis Program for Interfacing Thermal and Structural Codes*, NASA Technical Memorandum 87021, 1985.

[9] Greenblatt, D., Kirsten, T.J., Senatore, P., Louw, W.J., Dedekind, M.O., *Life Cycle Assessment of an Impingement-Cooled Gas Turbine Blade*, AIAA 92-4716.

[10] Nealy, D.A., Mihelc, M.S., Hylton, L.D., Gladden, H.J., *Measurements of Heat Transfer Distribution Over the Surfaces of Highly Loaded*

Turbine Nozzle Guide Vanes, Journal of Engineering for Gas Turbines and Power, Vol. 106, January 1984.

[11] Consigny, H., Richards, B.E., *Short Duration Measurements of Heat-Transfer Rate to a Gas Turbine Rotor Blade*, Journal of Engineering for Power, Vol. 104, July 1982.

[12] Rizzo, F.J., Shippy, D.J., *Thermomechanical Stress Analysis of Advanced Turbine Blade Cooling Configuration: Final Scientific Report*, 1979 Central Scientific Instruments Organisation (CSIO).

[13] Edmunds, T.M., Lawrence, R.A., *Monitoring Engine Thermal Stresses*, Rolls-Royce Limited Report.

[14] Rao, J.S., Sharan, A.M., Bahree, R., *The Design of Rotor Blades Taking Into Account the Combined Effects of Vibratory and Thermal Loads*, Journal of Engineering for Gas Turbines and Power, Vol. 111, October 1989.

[15] Panteleev, A.A., Trushin, V.A., *Calculation of transient temperature fields in cooled blades in turbines*, Telpoenergetika, Translation, August 1974.

[16] Takahashi, T., Watanabe, K., Takahashi, T., *Transient Analyses of Conjugate Heat Transfer of a first stage rotor blade in start-up and shut-down*, ASME Paper no. 2001-GT-0171.

[17] Allen, J.M., *Effect of Temperature Dependent Mechanical Properties on Thermal Stress in Cooled Turbine Blades*, Journal of Engineering for Power, Vol. 104, April 1982.

[18] Tzimas, E., Mullejans, H., Peteves, S.D., Bressers, J., Stamm, W., *Failure of Thermal Barrier Coating Systems under Cyclic Thermomechanical Loading*, Acta Materialia, 48, pp 4699-4707, 2000.

[19] Xu, H., Gong, S., Deng, L., *Preparation of thermal barrier coatings for gas turbine blades by EB-PVD*, Thin Solid Films, 334, pp 98-102, 1998.

[20] Dilzer, M., Gutmann, C., Schulz, A., Wittig, S., *Testing of a Low Cooled Ceramic Nozzle Vane Under Transient Conditions*, Journal of Engineering for Gas Turbines and Power, Vol. 121, April 1999.

[21] Fu, K.C., Harb, A., *Thermal Stresses of a Wind Turbine Blade made of Orthotropic Material*, Computers and Structures, Vol. 27, No. 2, pp225-235, 1987.

[22] Czech, N., Esser, W., Schmitz, F., *Gas turbine blade materials: the next steps*, Modern power systems, Turbine Technology, Vol. 15, pp43, 44-45, 1995.

[23] Kirsten, T.J., Greenblatt, D., Dedekind, M.O., *Thermal Fatigue Life Assessment of a convection-cooled gas turbine blade*, AIAA and International Symposium on Air Breathing Engines, 1993.

[24] Pejsa, P.N., Cowles, B.A., *Thermal Mechanical Fatigue Life Prediction for Advance Turbine Alloys*, Journal of Engineering for Gas Turbines and Power, Vol. 108, July 1986.

[25] Henderson, M.B., Ward, T.J., Harrison, G.F., Hughes, M., *Creep and Thermomechanical Fatigue Modelling of Single Crystal Superalloy Turbine Blades*, ASME Paper no. 2001-GT-0596.

[26] Crocker, D.S., Smith, C.E., *Numerical Investigation of Enhanced Dilution Zone Mixing in a Reverse Flow Gas Turbine Combustor*, Journal of Engineering for Gas Turbines and Power, Vol. 117, April 1995.

[27] Cohen, H., Rogers, G.F.C., Saravanamuttoo, H.I.H., *Gas Turbine Theory*, Second Edition, Longman, 1971.

[28] Gatewood, B.E., *Thermal Stresses*, McGraw-Hill, 1957.

[29] Townley, C.H.A., Darlaston, B.J.L., *The CEGB Research Programme on Thermal Fatigue of Structures – Its Background, Present State and Future Development*, Thermal Stresses and Thermal Fatigue, Proceedings of the International Conference, Gloucestershire, September, 1969.

[30] Logan, D.L., *A First Course in the Finite Element Method*, Second Edition, PWS Publishing Company, 1992.

[31] Patankar, S.V., *Numerical Heat Transfer and Fluid Flow*, Hemisphere Publishing Corporation, 1980.

[32] Mills, A.F., *Basic Heat and Mass Transfer*, IRWIN, 1995.

[33] Arts, T., Lambert de Rouvroit, M., *Aero-Thermal Performance of a Two-Dimensional Highly Loaded Transonic Turbine Nozzle Guide Vane: A Test Case for Inviscid and Viscous Flow Computations, ASME Journal of Turbomachinery*, Vol. 141, January, 1992.

[34] Croce, G., *Heat Transfer Analysis in a 2D turbine cascade*, Advanced Computational Methods In Heat Transfer.

[35] *Fluent 5 User's Guide Volume 2*, FLUENT INCORPORATED.

[36] Arts, T., Lambert de Rouvroit, M., Rutherford, A.W., *Aero-Thermal Performance of a Two-Dimensional Highly Loaded Transonic Turbine Nozzle Guide Vane: A Test Case for Inviscid and Viscous Flow Computations*, von Karman Institute for Fluid Dynamics, Technical Note 174, September 1992.

[37] White, F.M., *Fluid Mechanics*, Third Edition, McGraw Hill, 1994.

[38] White, F.M., *Viscous Fluid Flow*, Second Edition, McGraw Hill, 1991.

[39] Rothman, M.F. Editor, *High-Temperature Property Data: Ferrous Alloys*, ASM International, 1988.

[40] *Atar 9K50 – Instruction Manual*, Snecma.

[41] Van Wylen, G.J., Sonntag, R.E., Borgnakke, C., *Fundamentals of Classical Thermodynamics*, Fourth Edition, Wiley, 1994.

[42] Thopmson, P.A., *Compressible-fluid dynamics*, The Mapple Press Company, 1984.

[43] Liepmann, H.W., Roshko, A., *Elements of Gasdynamics*, Wiley, 1957.

[44] Zucrow, M.J., Hoffman, J.D., *Gas Dynamics Volume 1*, Wiley, 1976.

[45] www.haynesintl.com/188alloy

[46] Roos, T.H., *Atar 09K50 Hot condition*, 1996.

[47] Bezuidenhout, J.J., *Simplified failure location prediction method* PHD Thesis, University of Pretoria, 2003.

APPENDIX A

The temperature dependant material properties for 310 stainless steel and haynes 188 are given in this section. Where necessary a curve fit has been performed on the data for implementation into the CFD code.

The MarkII blade analysed in chapter four was fabricated from 310 Stainless steel. The material properties obtained were modelled as temperature dependent.

Thermal Conductivity	
T(K)	k(W/mK)
273	13.09
373	14.2
773	18.7
973	21

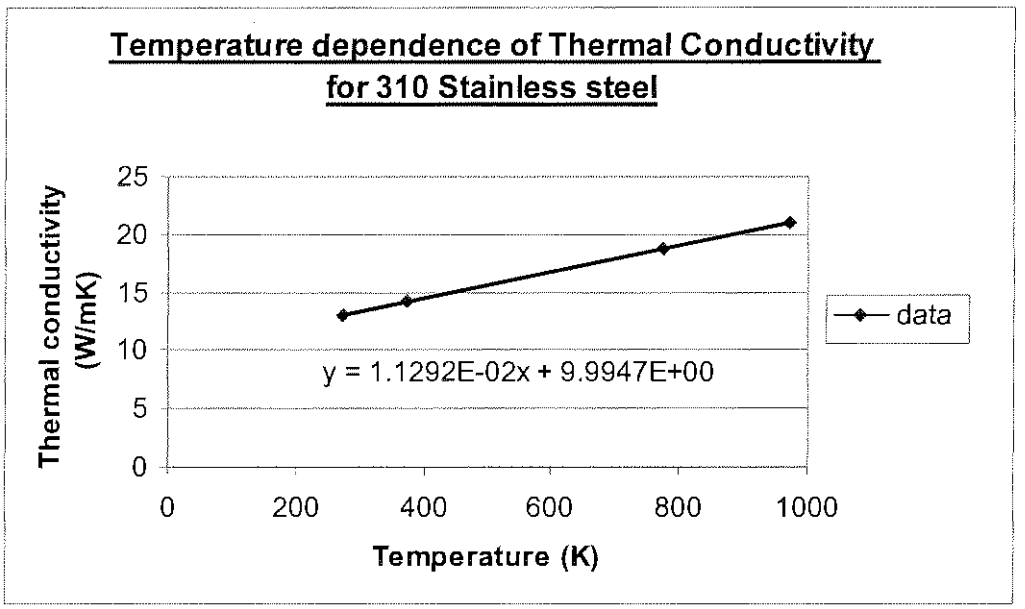

Figure A1 – thermal conductivity temperature dependence for 310 stainless steel

Coefficient of Thermal Expansion	
T(K)	alpha(m/mK)
293	1.58E-05
523	1.62E-05
773	1.69E-05
1273	1.91E-05

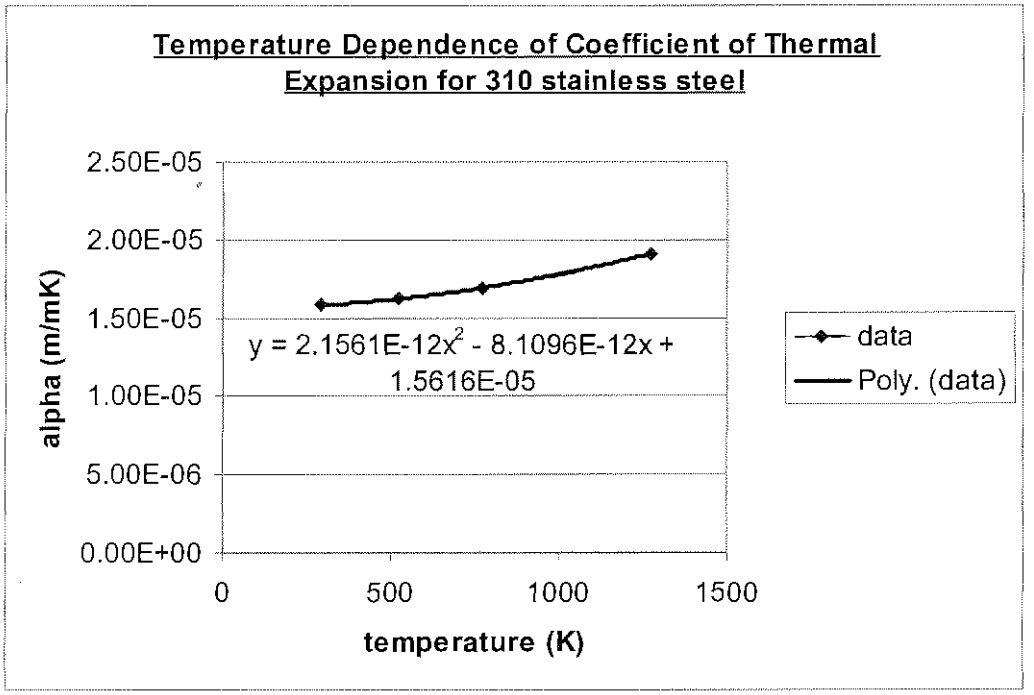

Figure A2 – coefficient of thermal expansion temperature dependence for 310 stainless steel

Young's Modulus	
T(K)	E (Pa)
293	215.00
973	150.00

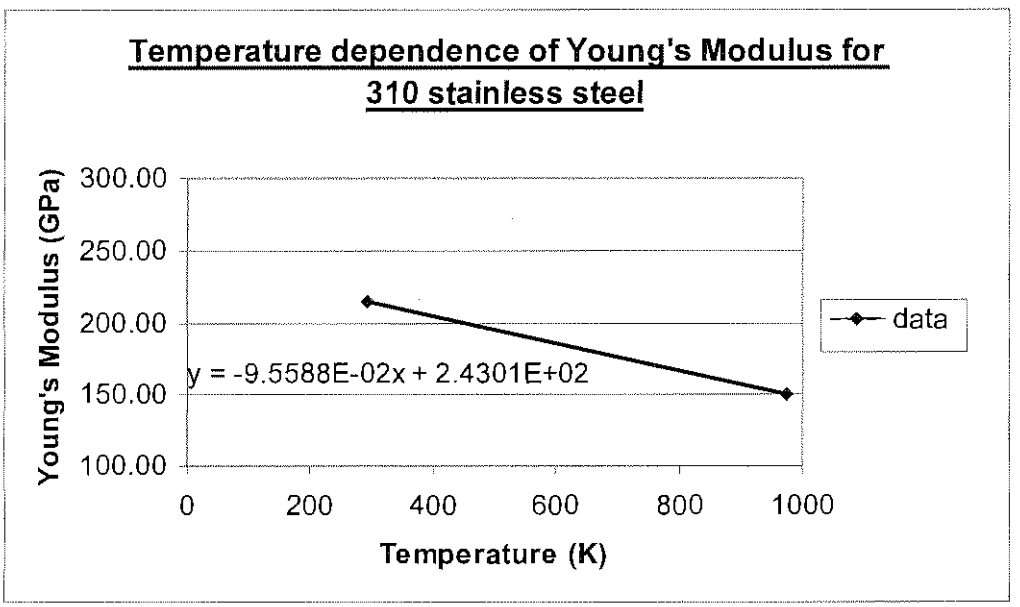

Figure A3 – Young's Modulus temperature dependence for 310 stainless steel

The Atar nozzle guide vane analysed in chapter 5 was fabricated from Haynes_188. The material properties were modelled as temperature dependent.

Thermal Conductivity	
T(K)	k
288	10.4
373.15	12.2
473.15	14.3
573.15	15.9
673.15	17.5
773.15	19.3
873.15	21.1
973.15	23
1073.15	24.8
1173.15	25.5
1273.15	27.6

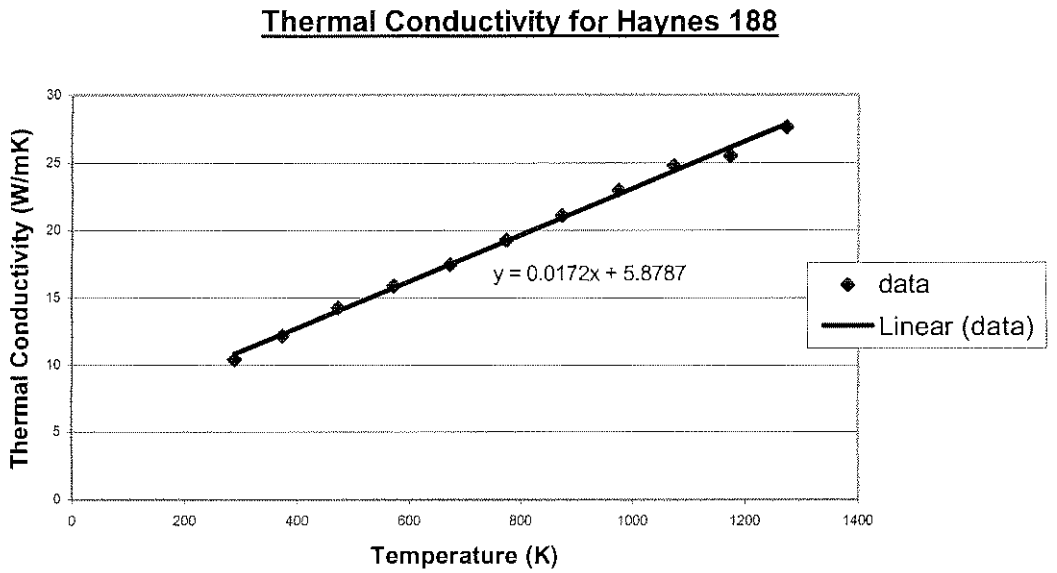

Figure A4 - thermal conductivity temperature dependence for Haynes 188

Specific Heat	
T(K)	Cp
288	403
373.15	423
473.15	444
573.15	465
673.15	486
773.15	502
873.15	523
973.15	540
1073.15	557
1173.15	573
1273.15	590

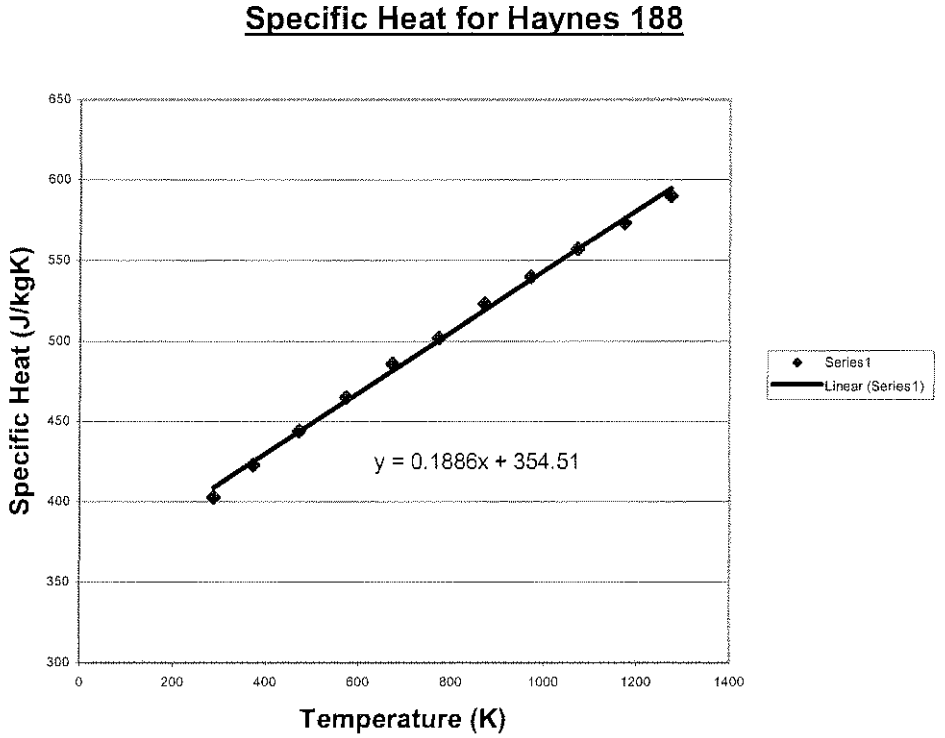

Figure A5 – specific heat temperature dependence for Haynes 188

Mean coefficient of thermal expansion	
DT(K)	alpha(m/mK)
75	0.0000119
175	0.0000126
275	0.0000132
375	0.0000138
475	0.0000145
575	0.0000152
675	0.0000158
775	0.0000165
875	0.0000171
975	0.0000179

Modulus of Elasticity	
T(K)	E(GPa)
288	232
373.15	225
473.15	217
573.15	209
673.15	201
773.15	193
873.15	184
973.15	176
1073.15	169
1173.15	161
1273.15	153

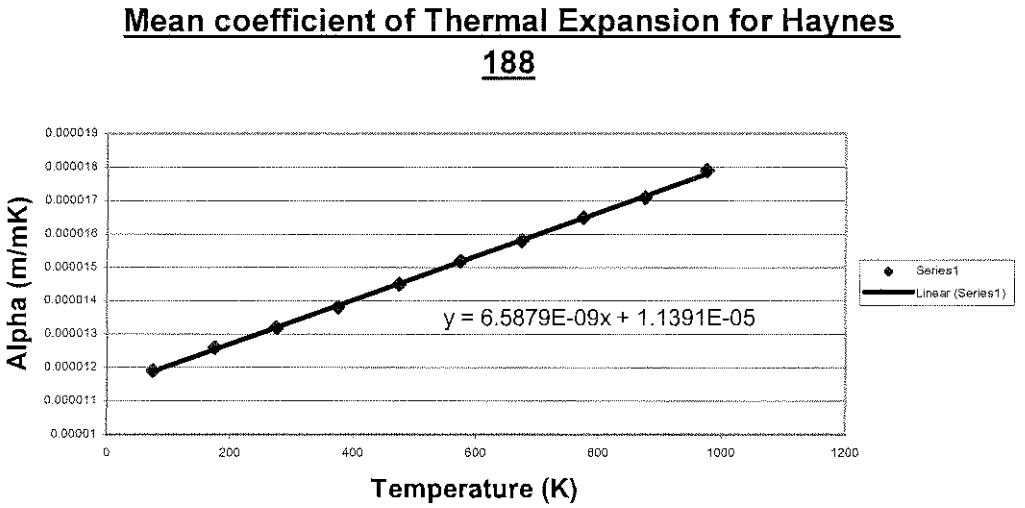

Figure A6 – mean coefficient of thermal expansion temperature dependence for Haynes 188

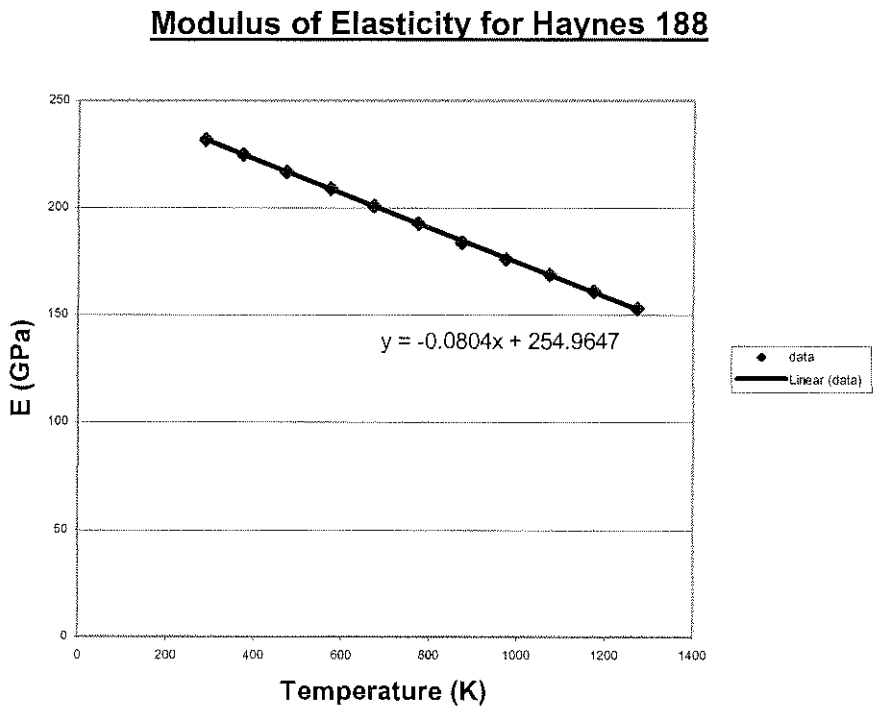

Figure A7 – Young's Modulus temperature dependence for Haynes 188

APPENDIX B

The Fortran code used to export the mesh and temperature data from FLUENT into FIDAP is given. The FLUENT user defined functions as well as the Matlab code used to generate the plot for the outlet static pressure variation calculation in chapter 5 are given.

```
c this code reads data from a PATRAN results file and writes
c it in the fidap neutral file format
      implicit none
      integer i,j, NUMNP, NDFVL, n1
      parameter (NUMNP=95620, NDFVL=2)
         real UF(NDFVL,NUMNP), T(NUMNP), P(NUMNP)
         real ux, uy, temp, pres
         open(unit=10,file='blade.rst',status='unknown')
         open(unit=20,file='blade.out',status='unknown')
c
      do 200 i=1,NUMNP,1
c
c            read(10,'(6x, I2,4E13.10)') n1, pres, ux, uy, temp
c
            read(10,'(3x, I5,1E13.5)') n1, temp
c     P(i) = pres
c     UF(1,i) = ux
c     UF(2,i) = uy
     T(i) = temp
 200  continue
c
c     write(20, '("VELOCITY          ")')
c     write(20,'(5E16.9)') ((UF(i,j), i=1,NDFVL),j=1,NUMNP)
c
c     write(20, '("PRESSURE          ")')
c     write(20,'(5E16.9)') (P(i), i=1,NUMNP)
c
     write(20, '("TEMPERATURE       ")')
     write(20,'(5E16.9)') (T(i), i=1,NUMNP)
     stop
     end
```

A similar code was written for the 2D case found in chapter 4.

The script shown below is the Matlab code used to generate the outlet static pressure variation for the Atar NGV.

```
%program to plot static pressure variation from hub to casing
Vt=377;    %tangential velocity at mean radius
R=287;     %air constant
T=1070.75; %static temperature at mean radius
r=(0.235:0.001:0.357); %range of radii from hub to casing
A=(Vt^2)/(R*T);
C=13.51;
C1=exp(C);
P1=r.^(A)
P=P1*C1;
hold on;
plot(r,P)

xlabel('radii, m'),ylabel('static pressure, Pa')
grid
title('Static pressure variation from hub to casing at NGV outlet')

% this plots the corrected mass flow rate
K=11.513;
K1=exp(K);
J=P1*K1;
plot(r,J,'r')
```

The FLUENT UDF's that were used to define the inlet temperature profile and the outlet static pressure variation are given below.

```
/*****************************************************************/
//* UDF for specifying steady-state boundary condition */
/*****************************************************************/
#include "udf.h"

DEFINE_PROFILE(inlet_temp, thread, position)
```

```
{
  real x[ND_ND];              /* this will hold the position vector */
  real z,y,radius,perc_blade;
  face_t f;

  begin_f_loop(f, thread)
    {
      F_CENTROID(x,f,thread);
      y = x[1];
            z = x[2];
            radius = sqrt(pow(y,2)+pow(z,2));
            perc_blade = ((radius - 0.23585)/0.12077)*100.;
      F_PROFILE(f, thread, position) = -0.00001695*pow(perc_blade,4) +
0.0032*pow(perc_blade,3) - 0.2299*pow(perc_blade,2) + 9.1717*perc_blade
+ 1008.6042;
    }
  end_f_loop(f, thread)
}

DEFINE_PROFILE(outlet_pres, thread, position)
{
  real x[ND_ND];              /* this will hold the position vector */
  real z,y,radius;
  face_t f;

  begin_f_loop(f, thread)
    {
      F_CENTROID(x,f,thread);
      y = x[1];
            z = x[2];
            radius = sqrt(pow(y,2)+pow(z,2));
      F_PROFILE(f, thread, position) = 736747.1262*pow(radius,0.467);
    }
  end_f_loop(f, thread)
}

DEFINE_PROFILE(outlet_pressure, thread, position)
{
  real x[ND_ND];              /* this will hold the position vector */
  real z,y,radius;
  face_t f;

  begin_f_loop(f, thread)
    {
      F_CENTROID(x,f,thread);
      y = x[1];
            z = x[2];
            radius = sqrt(pow(y,2)+pow(z,2));
      F_PROFILE(f, thread, position) = 100000.0001*pow(radius,0.462);
    }
```

```
  end_f_loop(f, thread)
}
```

The above UDF code is divided into three distinct sections. The first section is applying the inlet temperature profile in the form of a fitted fourth order polynomial. The second section deals with the initial guess of the outlet static pressure variation and the third section with the adjusted outlet static pressure variation.

APPENDIX C

The verification of the FEM results was done through a simple test case whose results were compared to an applicable one-dimensional equation.

The one-dimensional equation that may be used to calculate thermal stress is given:

$$\sigma = \alpha * E * \Delta T \qquad \text{C.1}$$

This equation was applied on a three dimensional bar, where the length is much greater than the width, so that this justifies the comparison with the FEM results to the one-dimensional equation.

The block analysed was fabricated from Haynes 188, so the material properties available in Appendix A are applicable. The block was clamped in all directions at both ends and its temperature was raised by 100 K. The mean coefficient of thermal expansion was taken as 0.0000119 m/mK and E=230 GPa. This gave a stress of 273.7 MPa.

The analysis done with Fidap gave similar results. Figures C1 and C2 show the stress distribution of the block.

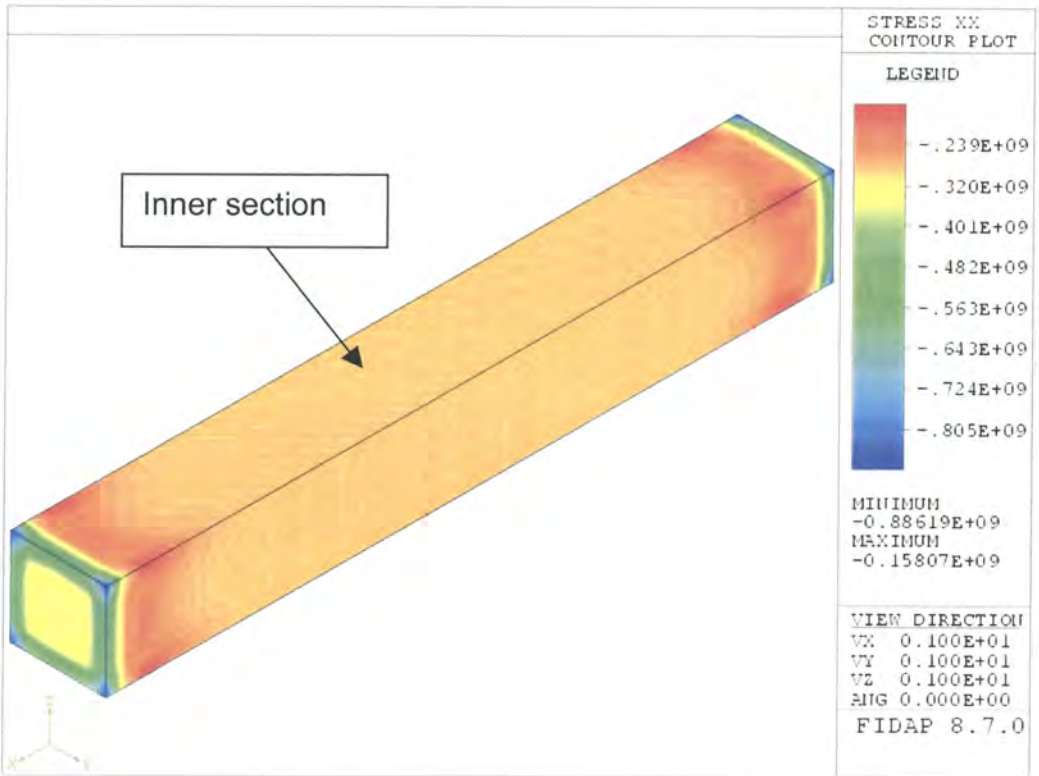

Figure C1 – filled contour plot of stress in x-direction

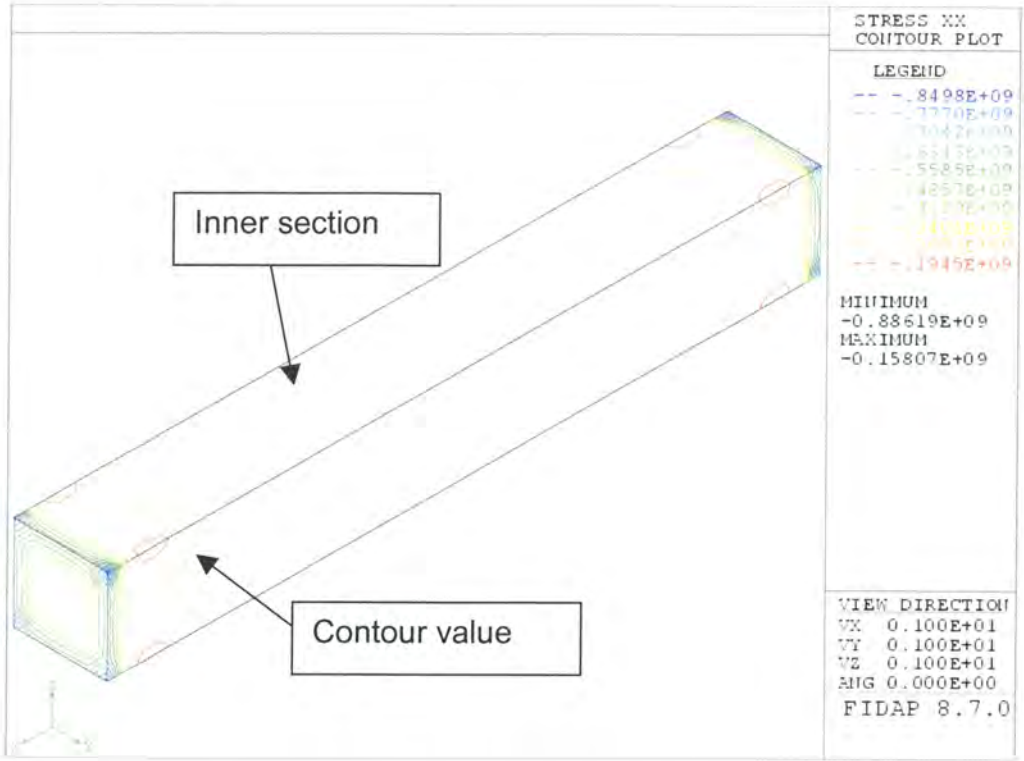

Figure C2 – line contour plot of stress in x-direction

It is important to note the scale on each plot shown. Also in order to compare, it is necessary to examine the stress distribution of the bulk of the block. Therefore one must ignore the end effects of the block where stresses will be higher due to the limitation of expansion caused by the clamping regime of the block. Thus if one examines the inner section of the block, Figure C1 shows the stress to lie between a contour value of 239 MPa to 320 MPa. To determine what the actual value of the inner section was, Figure C2 was plotted with contour lines. From this it is evident that the inner section of the blade is at 267.3 MPa, shown by the contour value in Figure C2. This gives an error of 2.34%, which is acceptably low.

APPENDIX D

The detailed calculation results needed in chapter five to estimate the boundary conditions are presented. These calculations are all an initial approximation and do not strictly represent the real conditions in the engine.

INLET CONDITIONS

Mass flow rate through one nozzle guide vane passage:

$$= \frac{96.3\% * total\_mass\_flow}{no.\_of\_vanes}$$

$$= \frac{0.963 * 71.65}{42}$$

=1.643 kg/s

INLET:

An average static inlet temperature was taken as 1172.6 K.
The Mach number at the inlet was determined using equation (D.1) and (D.3).
The inlet velocity was determined to be 192 m/s, k=1.33, R=287J/kgK

$$c = \sqrt{kRT} \tag{D.1}$$

The Mach number, M was calculated to be 0.287.

Then using the relation between Mach number, total and static pressure, equation (4.1), the static pressure was determined. Thus the static pressure was determined to be **P=543 039 Pa**.

THROAT:

The static temperature can be calculated using equation (D.2) P=416 902 Pa, k=1.33, T_0 = 1241K:

$$\frac{T_0}{T} = \left(\frac{P_0}{P}\right)^{\frac{k-1}{k}} \tag{D.2}$$

Thus, **T=1146.15 K**.

Then using the equation for mass flow rate, equation (D.3), the velocity at which the gas leaves the blade can be determined. The fluid density, ρ, is evaluated at the throat using the throat static temperature and pressure.

$$\dot{m} = \rho A V \tag{D.3}$$

The velocity, **C_2 = V = 448.55 m/s**.

Determination of blade pitch at mean radius

The specific engine consists of 42 nozzle guide vanes in its first stage. The following is available from the geometry:

- ✓ Blade length = 0.122 m
- ✓ Hub radius = 0.235 m

Therefore the pitch to be determined is at: 0.235+0.5*(0.122) = 0.296m

Circumference = 2*π*r

= 2*π(0.296)

= 1.8598 m

Therefore, the pitch at mean radius

$$s = \frac{1.8598}{42}$$

$$= 0.0443m$$

Determination of blade gas angles,

The opening, *o* =0.02236 m from the geometry.

The gas angle can now be determined for a Mach number of unity:

$$= \cos^{-1}\left(\frac{o}{s}\right)$$

$$= 59.7^0$$

Thus the outlet gas angle, α_2, from figure 7.13 of [27] at the mean radius:

$\alpha_2 = 57.14^0$

One can determine the gas angles at the hub and casing using equation (D.4)

$$\tan\alpha_2 = \left(\frac{r_m}{r}\right)\tan\alpha_{2m} \qquad \text{(D.4)}$$

Where r is the radius at the desired section (for example hub or casing) and α_{2m} is the gas angle at the mean radius.

Therefore,

α_{2h} **= 62.85^0**

α_{2c} **= 52.1^0**

The whirl component of the velocity, C_w, at the mean radius can be determined using equation (D.5) with C_2 = 448.55m/s:

$$\sin\alpha_2 = \frac{C_w}{C_2} \qquad \text{(D.5)}$$

Thus, C_w = 377 m/s.

Consider the radial equilibrium condition:

$$\frac{1}{r}C_w^{\,2} = \frac{1}{\rho}\frac{dP}{dr} \qquad \text{(D.6)}$$

The following assumptions were required to simplify equation (D.6) for a first approximation:

- The whirl velocity C_w does not vary from hub to casing
- The static temperature is constant

Using the ideal gas law for density, equation (D.6) can be re-arranged as:

$$\frac{dP}{P} = \frac{C_w^{\,2}}{RT}\frac{dr}{r} \qquad \text{(D.7)}$$

Integrating both sides:

$$\ln P = \frac{C_w^{\ 2}}{RT} \ln r + C \tag{D.8}$$

Therefore to evaluate the integration constant C, the following initial conditions were available:

r = r_m = 0.296 m , P = 416902 Pa, C_w = 377 m/s, R=287 J/kgK T = 1070.75 K evaluated using the ideal gas law. Thus substituting these values into and solving for C, one obtains C=13.5. Then substituting into equation (D.8) and taking the natural logarithms on both sides:

$$P = (7.29416e + 05) r^{0.4625} \tag{D.9}$$

Determination of nozzle loss coefficient

As an initial guess, a nozzle loss coefficient, λ_N = 0.05 is assumed.
Rotor rotational speed, N = 8400 rpm = 140 rps
The mean blade speed at the mean radius can be determined as U_m=260.375 m/s. A flow coefficient of ϕ = 0.8 is assumed. The axial flow velocity, C_{a2} can then be calculated as 208.3 m/s. Thus the absolute velocity, C_2 = 383.9 m/s.
The temperature equivalent of the outlet velocity can be determined from equation (D.10):

$$T_{02} - T_2 = \frac{V_2^{\ 2}}{2C_p} \tag{D.10}$$

Therefore T_2 = 1108.4 K and thus $T_2^{'}$, the ideal temperature assuming no frictional losses can be calculated using equation (D.11):

$$T_2 - T_2^{'} = \lambda_N \frac{C_2^{\ 2}}{2C_p} \tag{D.11}$$

Thus $T_2^{'}$ = 1105.2 K. The pressure P_2 can be calculated from:

$$\frac{P_{01}}{P_2} = \left(\frac{T_{01}}{T_2'} \right)^{\frac{\gamma}{\gamma-1}} \tag{D.12}$$

This gives P_2 = 452.2 kPa. It can now be determined if the nozzle is choking or not by comparing to the critical pressure ratio, given by equation (D.13):

$$\frac{P_{01}}{P_c} = \left(\frac{\gamma+1}{2} \right)^{\frac{\gamma}{\gamma-1}} \tag{D.13}$$

In this instance the nozzle was not choking. Therefore the annulus area and throat area of the nozzles can be determined. This in turn can be used to determine the overall blade loss coefficient λ. The detailed method as described in chapter seven of [27] was followed for this case.